# UC Santa Barbara
## UC Santa Barbara Electronic Theses and Dissertations

**Title**

Radium ions and radioactive molecules for probing new physics

**Permalink**

https://escholarship.org/uc/item/5j42z6c8

**Author**

Fan, Mingyu

**Publication Date**

2023

Peer reviewed|Thesis/dissertation

UNIVERSITY OF CALIFORNIA

Santa Barbara

Radium ions and radioactive molecules for probing new physics

A dissertation submitted in partial satisfaction of the
requirements for the degree Doctor of Philosophy
in Physics

by

Mingyu Fan

Committee in charge:

Professor Andrew Jayich, Chair
Professor David Weld
Professor Nathaniel Craig

June 2023

The dissertation of Mingyu Fan is approved.

---

David Weld

---

Nathaniel Craig

---

Andrew Jayich, Committee Chair

May 2023

Radium ions and radioactive molecules for probing new physics

Copyright © 2023

by

Mingyu Fan

To my parents

# Acknowledgements

# Curriculum Vitæ
Mingyu Fan

## Education

| | |
|---|---|
| 2023 | Ph.D. in Physics (Expected), University of California, Santa Barbara |
| 2020 | M.A. in Physics, University of California, Santa Barbara |
| 2017 | B.A. in Physics, with a minor in Mathematics, University of California, Los Angeles |

## Publications

*Ion optical clocks with three electronic states*, C. A. Holliman, M. Fan, and A. M. Jayich. *Proceedings of SPIE*, **PC12447**, PC124470C (2023).

*Measurement of the $Ra^+$ $7p^2P_{3/2}$ state lifetime*, M. Fan, C. A. Holliman, A. Contractor, C. Zhang, S. Gebretsadken, and A. M. Jayich. *Physical Review A* **105**, 042801 (2022).

*Radium Ion Optical Clock*, C. A. Holliman, M. Fan, A. Contractor, S. M. Brewer, and A. M. Jayich. *Physical Review Letters* **128**, 033202 (2022).

*Optical Mass Spectrometry of Cold $RaOH^+$ and $RaOCH_3^+$*, M. Fan, C. A. Holliman, X. Shi, H. Zhang, M. W. Straus, X. Li, S. W. Buechele, and A. M. Jayich. *Physical Review Letters* **126**, 023002 (2021).

*Direct measurement of the $7s^2S_{1/2} \rightarrow 7p^2P_{3/2}$ transition frequency in $^{226}Ra^+$*, C. A. Holliman, M. Fan, A. Contractor, M. W. Straus, and A. M. Jayich. *Physical Review A* **102**, 042822 (2020).

*Measurements of electric quadrupole transition frequencies in $^{226}Ra^+$*, C. A. Holliman, M. Fan, and A. M. Jayich. *Physical Review A* **102**, 062512 (2019).

*Measurement of the $7p^2P_{3/2}$ state branching fractions in $Ra^+$*, M. Fan, C. A. Holliman, S. G. Porsev, M. S. Safronova, and A. M. Jayich. *Physical Review A* **100**, 062504 (2019).

*Laser Cooling of Radium Ions*, M. Fan, C. A. Holliman, A. L. Wang, and A. M. Jayich. *Physical Review Letters* **122**, 223001 (2019).

**Abstract**


Radium ions and radioactive molecules for probing new physics

by

Mingyu Fan


Charge conjugation parity ($CP$) symmetry violation is linked to important physics questions such as the matter-antimatter asymmetry and the Strong $CP$ Problem. Table-top precision measurements using heavy atoms and molecules can set stringent bounds on the new physics that attempt to explain these problems, and these measurements are complementary to direct searches of new particles using colliders. Radium, among other radioactive elements, is a sensitive probe to hadronic $CP$ violation due to its heavy and octupole-deformed nucleus, and the sensitivity is further enhanced by incorporating the radioactive element in a molecule. In this thesis we introduce the first laser cooling of radium-226 ions and measurements of the low-lying $^{226}\text{Ra}^+$ energy levels. We realize control of the radium ion $S_{1/2} \to D_{5/2}$ optical qubit for implementing the quantum logic spectroscopy technique to prepare and readout the radioactive molecular ions. We also present production and detection of radium-containing molecular ions that are sensitive to hadronic $CP$ violation. Finally, we discuss ongoing work on designing a hadronic $CP$ violation experiment using radioactive molecular ions and developing a long-term source for the short-lived radium-224 and radium-225 atoms.

# Contents

# Chapter 1

# Introduction

One of the largest unsolved problems in physics is the matter-antimatter asymmetry. The Big Bang should produce an equal amount of matter and antimatter, and a process that favors production of matter is required to create the Universe we see today [1]. Such a process cannot be explained within the Standard Model and requires new physics that introduces interactions violating the charge conjugation parity ($CP$) symmetry, which is the symmetry between matter and antimatter [2]. Within the Standard Model, the lack of $CP$ violation in the strong interaction remains a mystery. Experiments have not found hadronic $CP$ violation [3, 4], yet the quantum chromodynamics (QCD) theory does not forbid $CP$ violation to occur. This is known as the Strong CP problem.

By studying the generation and annihilation of particles in colliders at high energies, physicists can directly study these problems by looking for new particles. On the other hand, the same physics that leads to unsolved problems such as the matter-antimatter asymmetry should affect everything in the universe in the same way. That means we can probe a system that can be measured really well to test new physics theories, too. Atoms and molecules are suitable systems for these experiments, as they produce the most precise measurement humans have made to date [5] and have relatively simple

structures so contributions from possible new physics can be predicted [6].

This thesis describes work towards probing hadronic $CP$ violation using radium-containing molecular ions. These heavy molecules have high sensitivities to hadronic $CP$ violating physics due to their nuclear and electronic structures, and experiments using these molecules could lead to one of the most sensitive tests of new physics. In the work associated with this thesis, we laser cooled radium ions for the first time and did fundamental measurements and tests on radium ions and radium-containing molecular ions that laid the groundwork for future precision measurements. These work also opens up other opportunities with radium ions including quantum information science [7] and optical clocks [8].

## 1.1   Dissertation Overview

This thesis is divided into 12 chapters and 1 appendix. Chapter 2 discusses the dynamics of trapped ions. Chapter 3 introduces the atomic ions we use, $Sr^+$ and $Ra^+$. Chapter 4 gives an overview of $CP$ violation and precision measurements using atomic, molecular, and optical (AMO) systems and specifically discusses hadronic $CP$ violation and radioactive molecular ions. Chapter 5 summarizes important light atom interaction physics that is relevant for this thesis. Chapter 6 documents the ion trapping apparatus used. Chapter 7 discusses the lasers, cavities, wavemeters, and experimental control systems for this thesis. Chapter 8 describes the trapping and laser cooling of radium-226 ions. Chapter 9 summarizes all finished and ongoing experiments measuring the basic properties of the radium ion. Chapter 10 discusses the progress on controlling the $Ra^+$ $S_{1/2} \to D_{5/2}$ optical clock transition. Chapter 11 summarizes the work on production and identification of heavy radium-containing molecular ions that are promising for hadronic $CP$ violation measurements. Chapter 12 discusses energy structures of radium-containing

polyatomic molecular ions and methods and challenges associated with a hadronic $CP$ violation measurement using these ions. Chapter 13 introduces the latest work on a long-term atom source for short-lived radium-224 and 225 isotopes. Appendix A presents a new ion trap built for molecular ion spectroscopy work in the future.

## 1.2    Permissions and Attributions

1. Content of Chapter 8 is a result of a collaboration with Craig Holliman, Anna Wang, and Andrew Jayich, and has previously appeared in *Physical Review Letters* [7]. It is reproduced here with the permission of Physical Review.

2. Part of Chapter 11 is a result of a collaboration with Craig Holliman, Xiaoyang Shi, Haoqing Zhang, Michael Straus, Xinghua Li, Sean Buechule, and Andrew Jayich, and has previously appeared in *Physical Review Letters* [9]. It is reproduced here with the permission of Physical Review.

3. Figure 12.3 is authored by Spencer Kofford. It is reproduced here with the author's permission.

# Chapter 2

# Linear Paul Traps

Ion traps are the central apparatus where we conduct all experiments on the ions in our lab. This chapter discusses dynamics of trapped ions in a linear Paul trap.

## 2.1 Single ion dynamics and stability regions

A potential well is required to trap a particle. For atoms and molecules, most traps depend on electromagnetic interactions, including Paul traps, Penning traps, magneto-optical traps, and optical dipole traps. Specifically, Paul traps confine ions with Coulomb forces, so they provide high trap depth that has storage times up to days or longer [10].

Point charges cannot be stably confined in 2D or higher dimensions with only static electric fields according to the Earnshaw's theorem: According to Gauss's law, the divergence of the electric field in free space is zero, so if a point charge is confined in one axis, there must be another axis where the charge is not confined. Therefore, time-dependent electric fields are required to trap an ion in 3D.

A schematic drawing of a linear Paul trap is shown in Fig. 2.1. An oscillating voltage $U_{\rm rf} \cos(\Omega_{\rm rf} t)$ is applied on one pair of the radial electrodes to confine the ions in the

radial plane, and a static voltage $U_{\text{ec}}$ is applied on the axial end cap electrodes to provide confinement along the trap axis. In addition, a DC bias voltage $U_{\text{dc}}$ is applied between the two rf pairs to break the degeneracy between the two radial directions.
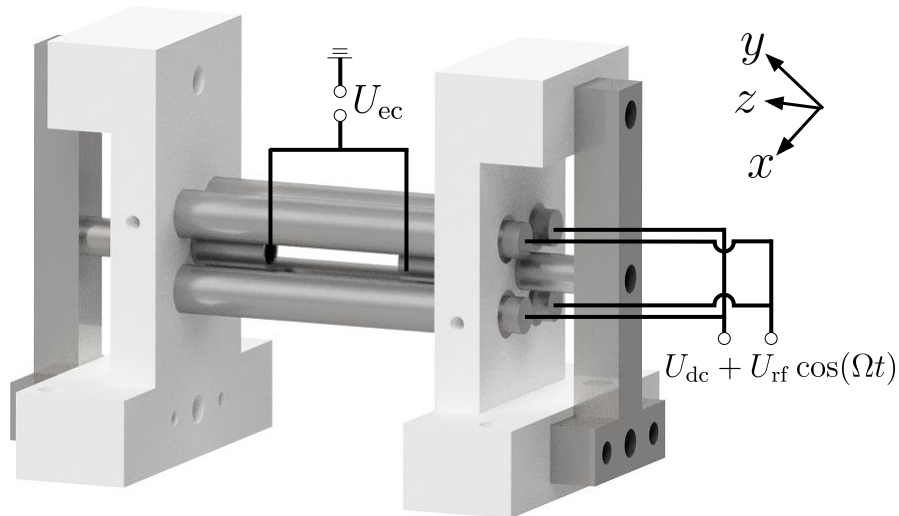


Figure 2.1: The linear Paul trap used for all radium ion work in this thesis.

The dynamics of a single ion in a linear Paul trap has been thoroughly studied [11, 12, 13]. Due to the importance of ion trapping in our research, the dynamics are derived again in this section, mostly following [13]. First of all, the electric potential near the center of the trap due to the radial voltage is

$$U_{\text{radial}}(x, y, z, t) = [U_{\text{rf}} \cos(\Omega_{\text{rf}} t) + U_{\text{dc}}] \frac{x^2 - y^2}{2r_0^2}, \tag{2.1}$$

where $r_0$ is the radial characteristic dimension of the trap, which is approximately the distance between the radial electrode surface to the trap center. This equation is only strictly true for hyperbolic-shaped electrodes, and higher order terms (sixth or higher power in $x$ and $y$) appear for the circular electrodes that are shown in Fig. 2.1. These higher order terms are small when the radial electrode radius $r_e \sim r_0$, and specifically, the sixth order term is zero when $r_e = 1.14511 r_0$ [14]. Such higher order terms could

5

reduce the stability region of a linear Paul trap that will be discussed later [13].

The potential due the axial voltage is

$$U_{\text{axial}}(x, y, z) = \frac{\kappa U_{\text{ec}}}{z_0^2}(z^2 - \frac{x^2 + y^2}{2}),$$ (2.2)

where $\kappa$ is an axial geometry factor that represents how much the end cap electrodes are shielded by the radial electrodes, and $z_0$ is the distance from the end cap electrodes to the trap center.

The total electric field potential is

$$U(x, y, z, t) = U_{\text{radial}}(x, y, z, t) + U_{\text{axial}}(x, y, z).$$ (2.3)

Assuming that the ion is only subject to the Coulomb force [1], the dynamics of a single ion is described by the Mathieu equation

$$\ddot{u}_i + [a_i + 2q_i \cos(\Omega_{\text{rf}}t)]\frac{\Omega_{\text{rf}}^2}{4}u_i = 0,$$ (2.4)

where $i$ is one of the three directions $x$, $y$, or $z$, $u_i$ is the displacement of the ion on the $i$ direction relative to the trap center, and $a_i$, $q_i$ are the following parameters

$$a_x = \frac{4eU_{\text{dc}}}{mr_0^2\Omega_{\text{rf}}^2} - \frac{4\kappa eU_{\text{ec}}}{mz_0^2\Omega_{\text{rf}}^2},$$ (2.5)

$$a_y = \frac{-4eU_{\text{dc}}}{mr_0^2\Omega_{\text{rf}}^2} - \frac{4\kappa eU_{\text{ec}}}{mz_0^2\Omega_{\text{rf}}^2},$$ (2.6)

$$a_z = \frac{8\kappa eU_{\text{ec}}}{mz_0^2\Omega_{\text{rf}}^2},$$ (2.7)

---

[1]The Earth's gravitational force ($\sim 10^{-24}$ N) pulls the ion away from the trap center by $\sim 1$ pm in a typical ion trap, which is negligible compared to a typical ion trap dimension $\sim 1$ mm.

$$q = q_x = -q_y = \frac{2eU_{\mathrm{rf}}}{mr_0^2\Omega_{\mathrm{rf}}^2}, \tag{2.8}$$

$$q_z = 0. \tag{2.9}$$

The solutions of the Mathieu equation can be either quasi-periodic or diverging dependent on the $a_i$ and $q_i$ parameters. For stable trapping of ions, we need to choose parameters that lead to quasi-periodic solutions, which are shown as the blue shaded regions in Fig. 2.2(a).
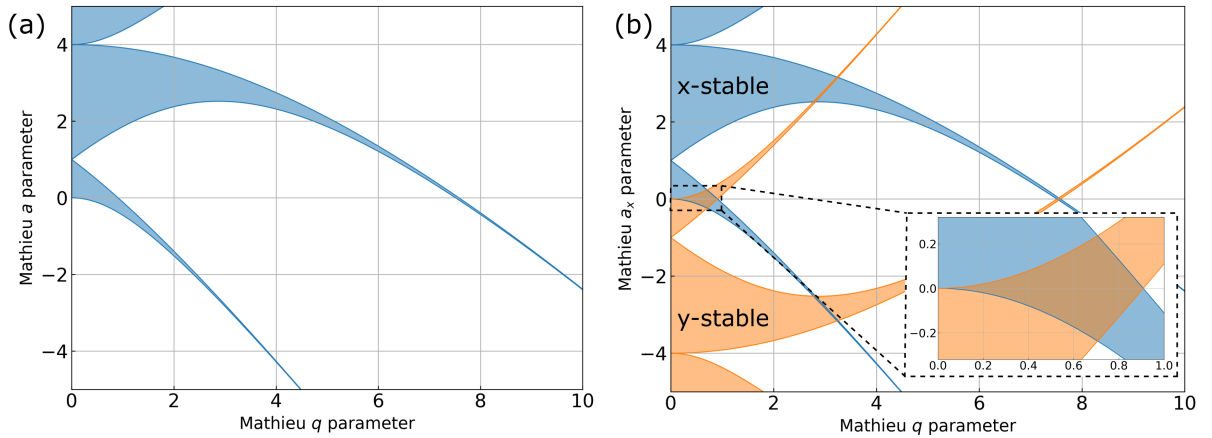


Figure 2.2: (a) Stability regions (blue shaded) of the Mathieu equation. (b) Stability regions for $x$ (blue) and $y$ (orange) axes in terms of $q$ and $a_x$ when the trap axial voltage $U_{\mathrm{ec}} = 0$. The cross-section of the blue and orange shaded areas are stable in both radial directions. Insets shows the first stability region we use for ion trapping work.

The stability conditions for $a_i$ and $q_i$ must be satisfied for all three axes to trap an ion. As $q_z = 0$ and $a_z > 0$, the ion is always stable on the trap axis with a positive end cap voltage. The stability conditions for the radial directions are more complicated, but the problem can be simplified if we assume the end cap voltage $U_{\mathrm{ec}}$ is small. In this case, $a_y = -a_x$, and the stability regions for both $x$ and $y$ directions can be overlaid as in Fig. 2.2(b), and they must both be satisfied for stable trapping of an ion. In practice, a positive end cap voltage decreases both $a_x$ and $a_y$ and it needs to be included when

calculating the trapping parameters.

An approximate quasi-periodic solution of Eq. 2.4 for $|a_i| \ll 1$ and $|q_i| \ll 1$ is [11]

$$u_i(t) \approx u_{1i} \cos(\omega_i t + \varphi_{Si})[1 + \frac{q_i}{2} \cos(\Omega_{\rm rf} t)], \tag{2.10}$$

where the motion can be separated into the "secular" motion at frequency

$$\omega_i = \frac{\Omega_{\rm rf}}{2} \sqrt{a_i + \frac{q_i^2}{2}}, \tag{2.11}$$

and the "micromotion" at the trap rf frequency $\Omega_{\rm rf}$. The secular motion amplitude $u_{1i}$ and phase $\varphi_{Si}$ are determined by the initial condition. The secular motion is thermal in nature and its amplitude can be reduced via techniques such as laser cooling. If micromotion is not considered, the ion can be approximated as in a pseudo-potential of a 3D harmonic oscillator characterized by the secular frequencies. There is no micromotion along the trap axis because $q_z = 0$, and the radial micromotion will be discussed more in Section 2.3.

## 2.2   Dynamics of multiple ions

We often need to trap more than one ion in an ion trap at the same time, e.g. for quantum logic spectroscopy [15, 16] of radioactive molecular ions to probe hadronic $CP$ violation. In this section we discuss the dynamics of multiple ions in the trap, with a focus on the two-ion linear crystal case.

To trap multiple ions stably, each of the ions must individually satisfy the single-ion stability requirements in Fig. 2.2 [17]. Although $q$ is theoretically stable from 0 to 0.908 with $a_x, a_y \sim 0$, for $q > 0.3$ the micromotion amplitudes increase which is generally not desired. On the other hand, a very small $q$ may not provide a deep enough trap

potential for stable confinement of ions. Therefore, an ion trap can only confine species with similar mass to charge ratios.

When the trapped ions are "hot" so that they move in the ion trap with large amplitudes, the time-averaged Coulomb force from other ions is much smaller than the time-averaged Coulomb force from the trap potential. In this regime, dynamics of individual trapped ions can be approximated by the Mathieu equation, and there is little interaction between the ions. Over a time scale that is much longer than the secular motion periods in the trap, the small ion-ion Coulomb interaction thermalizes the system and every ion attains the same kinetic energy.

In the opposite limit that the ions are "cold", each ion moves around the equilibrium position with its motional amplitude much less than the separation between the ions. In this regime, the trapped ions form a Coulomb crystal where the crystal shape is dependent on the ion species and the radial and axial potentials applied [18]. If the radial secular frequencies $\omega_x$ and $\omega_y$ are much greater than axial secular frequency $\omega_z$, the ions form a linear chain along the trap axis. If $\omega_z \gg \omega_x, \omega_y$, the ions form a 2D crystal in the radial plane [18]. If the radial and axial secular frequencies are similar, the crystal is zigzag shaped for a small number of ions [19] and forms shell structures for a large number of ions [20].

We are interested in the few-ion linear crystal case in our experiments. With a linear crystal along the trap axis, the micromotion is minimized as the trap rf field is zero along the trap axis. There are a total of $3N$ secular motional modes for $N$ ions, and each mode corresponds to a normal mode of the collective motion of the ion chain. The equations of motion for linear crystals are detailed in [17], and in this section we discuss the two-ion specific case in detail.

We assume that two ions of masses $m$, $M$ and charge $q = -e$ are trapped, and both ions are crystallized and aligned in the trap axis, as shown in Fig. 2.3(a). Similar

9
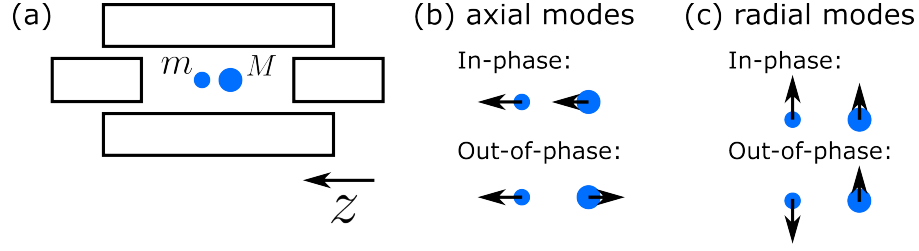
Figure 2.3: (a) Two-ion crystal along the trap axis. (b) Normal modes of the two-ion crystal in the trap axis. (c) Normal modes of the two-ion crystal in a radial direction.

to coupled oscillators, the motion of the ions in each direction can be decomposed into normal modes of in-phase motion at frequency $\omega_{i,\text{ip}}$ and out-of-phase motion at frequency $\omega_{i,\text{oop}}$, see Fig. 2.3(b) and (c). The secular frequencies of the two modes along axis $i$ are [21]

$$\omega_{i,\pm} = \omega_{i,m} \sqrt{1 + \frac{1}{\mu} \pm \sqrt{1 + \frac{1}{\mu^2} - \frac{1}{\mu}}}, \qquad (2.12)$$

where $\omega_{i,m}$ is the single-ion secular frequency along $i$ for mass $m$ (see Eq. 2.11), and $\mu$ is the mass ratio $M/m$.

For the axial mode ($i = z$), the positive sign of Eq. 2.12 is chosen for the out-of-phase mode and the negative sign for the in-phase mode. For the radial modes ($i = x, y$), the positive (negative) sign is for the in-phase (out-of-phase) mode.

## 2.3   Micromotion

Micromotion is typically an unwanted effect in ion traps [2]. Doppler shifts from micromotion appear as micromotion sidebands in the spectrum which could lead to off-resonant scatterings and ion heating [11, 24]. In addition, for precision spectroscopy such as an ion optical clock, micromotion induced frequency shifts are a key systematic effect.

---

[2]There are a few exceptions [22, 23] where the micromotion is used to enhance entanglement in an ion trap.

For an ideal ion trap with all ions crystallized along the trap axis, the micromotion amplitude is proportional to the secular motional amplitude, see Eq. 2.10. In this case, the energy of the radial micromotion is approximately the same as the energy of the associated radial secular motion [11], and such micromotion is called the intrinsic micromotion as it cannot be eliminated in an ion trap.

Excess micromotion can arise from stray dc electric fields or from a phase offset of the rf signals on the different radial electrodes. A stray electric field pushes the equilibrium positions of trapped ions away from the trap axis, and the equilibrium positions oscillate around the trap axis if there is a rf phase offset. In either case, as the equilibrium position is no longer along the trap axis, the ions experience non-zero rf electric fields even if the secular motion amplitude is zero. Such excess micromotion can lead to significant distortion of the transition spectrum [11] and rf heating of the trapped ions [24]. Therefore, it is of experimental interest to detect and compensate for excess micromotion. We discuss several methods of micromotion compensation in this section.

One of the simplest methods to detect micromotion due to stray electric fields is to observe ion equilibrium position movements when changing the rf voltage amplitude driving the trap [11]. With the same stray fields, if the rf amplitude increases so the radial pseudo-potential becomes steeper, the equilibrium positions of ions will move towards the trap center. If the stray electric field is zero, the ions will not move when the rf amplitude is changed. This method only needs an imaging system that is sensitive to ion movement along the radial directions, and it can be used as long as the center of an ion crystal can be identified. However, it has the following disadvantages:

- This method is not sensitive to micromotion induced by a rf phase shift. With a rf phase shift, the ion equilibrium positions oscillate around the trap axis at the trap rf frequency, and the average position of the ion will not move. This method is only

effective when the rf phase shift is large enough so the oscillation of the equilibrium position can be observed on the camera.

- To compensate for micromotion on both of the micromotion axes, two imaging systems are needed to observe the ion movement on two radial directions.

- In an ion trap of high secular frequencies ($\omega_x, \omega_y > 2\pi \times 1$ MHz), the ion movement distance is small and therefore difficult to observe.

The other two methods to detect micromotion are based on the Doppler shift of laser light induced by the micromotion. Following the treatment in [11], the micromotion leads to sidebands in the transition spectrum modulated by the trap rf frequency. The light-induced electric field in a sideband of order $n$ (frequency shifted by $n\Omega_{\mathrm{rf}}$) is

$$\mathbf{E}(n) \propto J_n(\beta), \tag{2.13}$$

where $J_n(\beta)$ is the Bessel function of the first kind of order $n$, and $\beta$ is the micromotion index

$$\beta = \sqrt{\left(\frac{1}{2}\sum_{i=x,y} k_i u_{0i} q_i\right)^2 + \left(\frac{1}{4}k_x q_x r_0 \alpha \varphi_{\mathrm{offset}}\right)^2}, \tag{2.14}$$

where $\mathbf{k} = \sum_{i=x,y,z} k_i \hat{\mathbf{i}}$ is the $k$-vector of the laser, $u_{0i}$ is the displacement of the equilibrium position due to the bias field along the direction $i$, $\alpha$ is a trap geometry factor that is on the order of unity [11], and $\varphi_{\mathrm{offset}}$ is the rf phase offset between the electrodes.

One method to detect micromotion is to measure transition spectrum of the ion. If the spectrum shows significant micromotion sidebands, it indicates that the excess micromotion along the laser direction is non-zero [25]. For a newly assembled ion trap that has never been micromotion compensated before, there could be large stray fields that create high-order micromotion sidebands. In such asses, the typical laser cooling

scheme with light red-detuned by approximately half the natural linewidth no longer works. We have observed that the micromotion may broaden the cooling transition of $Sr^+$ ions to $\sim 2$ GHz (natural linewidth $\sim 20$ MHz) without compensation, so the laser needs to be red-detuned by $\sim 1$ GHz to cool the ions. In this case, the micromotion compensation can be achieved by applying bias voltages to counteract the stray fields, and the results can be checked by monitoring the light detuning required to cool the ions.

Another method to detect micromotion is through a cross correlation between the ion fluorescence and micromotion. If the ion moves at the trap rf frequency, its fluorescence will be Doppler modulated at the same frequency. We can demodulate the ion fluorescence signal at the trap rf frequency with a lock-in amplifier to detect micromotion. If the trap rf frequency is greater than the fluorescence transition linewidth, this method may not be useful due to the smaller modulation depth. Both methods that detect micromotion with a laser are only sensitive to the micromotion that is along the laser direction, so multiple laser beams are typically necessary to measure and compensate micromotion on all axes.

# Chapter 3

# Stontium and Radium Ions

This chapter discusses the strontium and radium ions, the two alkaline-earth elements that we use in this thesis.

## 3.1  Alkaline-earth ions

While ion traps provide long coherence time and storage time, they only work with charged species. Most of the atomic ions that has been thoroughly studied in an ion trap have a single valence electron, so their electronic level structures are relatively simple, often with cycling transitions formed with only a few lasers. For example, the first laser-cooled atom, $Mg^+$ [26], has a $S_{1/2} \rightarrow P_{3/2}$ cycling transition for efficient Doppler cooling and detection.

Other alkaline earth elements, similar to $Mg^+$, have cooling transitions that are laser accessible. The first two elements in Group II, $Be^+$ and $Mg^+$, have cooling transitions around 300 nm. The heavier elements from $Ca^+$ to $Ra^+$ have low-lying $D_{3/2}$ and $D_{5/2}$ states that require an additional repumping laser to form cycling transitions. The $D_{3/2}$ and $D_{5/2}$ states also provide optical clock states [27, 28, 29, 8] and metastable hyperfine

qubits [30]. Most of the other laser-cooled ions, e.g. $Zn^+$ [31], $Cd^+$ [32], $Hg^+$ [33], $Yb^+$ [34], are spectroscopically similar to alkaline earth ions with a single $s$-orbital valence electron in the ground state.

## 3.2   Strontium ions

The low-lying energy structure of $Sr^+$ is shown in Fig. 3.1 (a). The most abundant isotope of strontium, strontium-88, has no nuclear spin. The optical clock transition between the $S_{1/2}$ ground state and the $D_{5/2}$ metastable state (0.39 s lifetime [35]) is one of the secondary representations of the second [28], and is also used as an optical qubit for quantum information science [36].
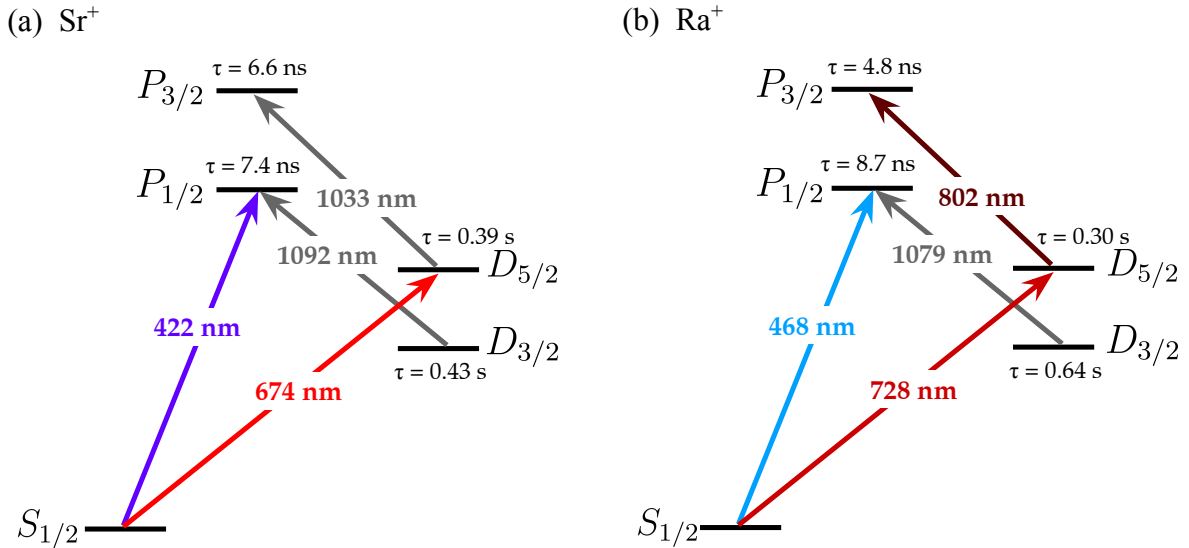


Figure 3.1: Low-lying energy levels of (a) $Sr^+$ and (b) $Ra^+$.

In the scope of this thesis, the $^{88}Sr^+$ ion serves as a test species for ion trap and other apparatus because of its similarity to $^{226}Ra^+$. Both species have a nuclear spin of zero, and share the same cooling $S_{1/2} \rightarrow P_{1/2}$ transition and repumping $D_{3/2} \rightarrow P_{1/2}$ transition. All low-lying $Sr^+$ transitions are compatible with diode lasers without the

need for frequency conversion, and recently integrated photonics for all lasers for $Sr^+$ control have been demonstrated [37]. In addition, the $S_{1/2} \rightarrow P_{1/2}$ transition is only 440 MHz blue-detuned relative to a dipole transition of $^{85}Rb$ [38], so the cooling laser can be stably locked to a convenient wavelength via saturation absorption spectroscopy of Rb atoms in a cell. These properties of $^{88}Sr^+$ make it a convenient species to test ion traps in our lab, including a cryogenic chamber for characterization of novel ion trap designs [39].

## 3.3   Radium ions

Radium is the heaviest element in the group II of the periodic table with all of its isotopes radioactive. Due to its radioactivity, the spectroscopy data of this atom is rare compared to other alkaline-earth elements, but more experiments using radium have appeared in the last 15 years. Here is an overview of previous atomic, molecular, and optical (AMO) physics experiments using radium: The first spectroscopy of dipole transitions of neutral radium atoms and radium ions was done in 1930s with a hollow-cathode lamp setup [40, 41, 42]. Absorption measurements of some Rydberg lines in the neutral radium atom have been done in 1980 [43]. In the 1980s, Isotope shifts and hyperfine splittings of several transitions for a range of neutral and ionic radium isotopes were measured with ion beams in ISOLDE at CERN [44, 45]. The short-lived radium isotopes from radium-209 to 214 have been transported from a radioactive beam line and trapped in linear Paul traps at the University of Groningen, where a series of spectroscopy work has been done [46, 47, 48, 49, 50]. Neutral radium-226 and radium-225 have also been trapped for atomic EDM measurements to probe hadronic $CP$ violations [51, 52, 53]. More recently, the spectrum of RaF molecules has been measured [54].

The energy level diagram of $Ra^+$ is shown in Fig. 3.1 (b). Similar to the strontium ion, all required light to operate the radium ion can be generated by diode lasers. The

$Ra^+$ cooling laser (468 nm) and photoionization lasers (483 nm, 450 nm) are of longer wavelengths compared to their counterparts for $Sr^+$, so more laser power is generally available and the lasers are more stable.

### 3.3.1  $^{226}$Ra$^+$

Radium-226 is the most stable isotope of radium, first discovered by Marie Curie in 1898 [55]. It has a radioactive half-life of 1600 years. The relatively long half-life allows radium-226 to be directly stored in the experiment chamber as a long-term source of radium ions. Similar to $^{88}$Sr$^+$, $^{226}$Ra$^+$ has a narrow transition $S_{1/2} \rightarrow D_{5/2}$ (0.3 s lifetime [56]) that can be used as an optical clock or for quantum information science experiments. However, as radium-226 does not have a nuclear spin, its nucleus is not quantized and thus it cannot be used in a precision measurement of symmetry-violating moments in the nucleus.

### 3.3.2  $^{225}$Ra$^+$

Radium-225 has a nuclear spin of 1/2 and a half-life of 15 days. With the nonzero nuclear spin, its nuclear moments can be measured in radium atoms [52] or radium-containing molecules. In addition, radium-225 has a heavy octupole-deformed nucleus, which generates closely-separated parity doublets in the nuclear energy structure that enhances the $CP$-violating moments. These nuclear properties make radium-225 a sensitive probe of hadronic $CP$ violation [57, 6], which will be discussed more in Chapter 4.

The nuclear spin of 1/2 also generates hyperfine structures in the electronic states of the radium ion. Specially, the $S_{1/2}$ ground state has $F = 0$ and $F = 1$ hyperfine manifolds that can be used as hyperfine qubit states that are insensitive to first-order magnetic field fluctuations at small magnetic fields. The $F = 0$ qubit state can be eas-

ily prepared via optical pumping, following the $^{171}$Yb$^+$ work [58] that is used in many trapped ion quantum information science experiments [59, 60]. The magnetic field insensitivity can also help a $^{225}$Ra$^+$ optical clock in terms of stability and systematic effect evaluations [61]. This clock transition is useful for implementing the logic ion in quantum logic spectroscopy [16] of radioactive molecular ions to probe hadronic $CP$ violations.

The shorter half-life of radium-225 makes the isotope more challenging to work with. Experiments directly using radium-225 requires a $\sim$ mCi source [53], which is significantly more than the $\sim 10$ $\mu$Ci used with $^{226}$Ra$^+$ [7]. In addition, the number of radium-225 atoms halves every two weeks, so regular replacement of the sample is needed. These difficulties prompt us to build a long-term source of radium-225 atoms using its parent isotope, thorium-229, which has a radioactive half-life of 7825 years. Our work towards this long-term source of radium-225 atoms is discussed in Chapter 13.

# Chapter 4

# Radioactive molecules and new physics

The Standard Model of physics describes three of the four fundamental interactions (excluding gravity), and all predicted particles in the Standard Model have been discovered. Despite the great success of the Standard Model, there remain important physics problems that are not explained. One of them is the matter-antimatter asymmetry, why is there more matter than antimatter in the Universe. A popular explanation of the problem is the baryogenesis theory, where a process that favors the generation of matter over antimatter happened in the early universe just after the big bang. Baryogenesis can only occur with the Sakharov conditions [2], and requires violation of the $CP$ symmetry. Within the Standard Model, there is not enough $CP$ violation to explain the matter-antimatter asymmetry that we see today [1], so additional $CP$-violating interactions beyond the Standard Model are required.

Particle colliders have been used to search for new physics which may explain the matter-antimatter asymmetry and other problems such as dark matter. For example, the Large Hadron Collider is used to probe supersymmetry particles at energy scales

of $\sim 1$ TeV [62]. Although these experiments are direct tests of new physics, these large-scale experiments have high costs and need many physicists to run.

An alternative approach is to search for new physics using tabletop precision measurements. If the same physics that generates the matter-antimatter asymmetry exists today, we should be able to probe it by measuring any system that has sensitivity to the sources of new physics. Among all systems, atoms and molecules have the following advantages:

- Atoms and molecules are relatively simple systems that have mature experimental tools such as lasers and traps. High fidelity techniques for state preparation, interrogation, and readout have been developed too. On the theoretical prospective, it is possible to calculate the effects from the new physics on the atoms and molecules, e.g. energy shifts.

- Atoms and molecules can be measured to very high precision. The most precise measurements that humans have done are optical clocks, which measure transition frequencies in atoms to $< 10^{-18}$ fractional uncertainty [5]. Such precision measurements are important as effects from the new physics must be small.

- Each atom or molecule of the same species is identical. Therefore, the same experiment can be repeated in another place or time to gather statistics or to test systematic effects.

As $CP$ violation is an integral part of the barogenesis theory, it is natural to search for $CP$-violating interactions in atoms and molecules. According to the $CPT$ theorem, violation of the $CP$ symmetry is equivalent to violation of the $T$ (time-reversal) symmetry, so we can search for $T$-violating moments in atoms and molecules to probe new physics. One of these moments is the electric dipole moment (EDM) of a fundamental particle,

which violates both the $P$ and $T$ symmetries. The EDM can be measured by placing the particle in an electric field, so the particle energy is dependent on the alignment between the EDM and the electric field. If a nonzero energy shift accompanies reversal of quantization direction (spin) of the particle, it indicates that the particle has a nonzero EDM.

## 4.1 Electron EDM measurements

The search for an electron EDM (eEDM) is one of the most sensitive probes of new physics. However, electrons are very light charged particles that move in an electric field, so it is difficult to directly measure the EDM-induced energy shift of free electrons. Electron EDM experiments instead measure the energy shifts of polarized paramagnetic atoms or molecules that have an unpaired valence electron.

How does the EDM of the valence electron manifest as an energy shift of the atomic or molecular system? In the following discussion we consider a paramagnetic neutral atom or molecule in an external electric field, but the arguments work for ionic systems too. If the eEDM, $d_e$, can be measured in this system, the Stark shift Hamiltonian

$$H_{\text{eEDM}} = \mathbf{d_e} \cdot \mathbf{E}_{\text{eff}} \tag{4.1}$$

must have a nonzero expectation value, where $\mathbf{E}_{\text{eff}}$ is the effective electric field on the valence electron. According to Schiff's theorem [63], the expectation value of $\mathbf{E}_{\text{eff}}$ must be zero in a neutral system: If $\langle \mathbf{E}_{\text{eff}} \rangle$ is nonzero, the electron is accelerated by the Coulomb force, but the neutral system remains still in an electric field. Thus we would anticipate the electron separated with the neutral atom if there is a net electric field, which is not the reality. Therefore, within nonrelativistic physics where $\mathbf{d_e}$ is a constant, the eEDM

produces no shift on the polarized atom or molecule. However, bound electrons in an atom move at relativistic speeds $v \sim \alpha c$, so relativistic effects must be considered. When the valence electron moves close to the nucleus, the speed is faster so relativistic length contraction results in a smaller $d_e$ [63, 64]. Therefore, although $\langle \mathbf{E}_{\text{eff}} \rangle = 0$, the Stark shift $\langle \mathbf{d_e} \cdot \mathbf{E}_{\text{eff}} \rangle \neq 0$, leading to an energy shift on the atomic or molecular levels due to the eEDM.

For a paramagnetic atom, the effective electric field that the valence electron experiences is proportional to the applied external electric that the atom experiences, so the energy shift can be regarded as produced by a permanent atomic EDM due to the eEDM

$$H_{\text{eEDM,atom}} = \mathbf{d}_{\text{atom}} \cdot \mathbf{E}, \tag{4.2}$$

where $\mathbf{E}$ is the external laboratory electric field and $\mathbf{d}_{\text{atom}}$ is the atomic EDM

$$\mathbf{d}_{\text{atom}} = R\mathbf{d_e}, \tag{4.3}$$

where $R$ is an enhancement factor [65] that is proportional to $Z^3$ due to relativistic effects. For example, $R = -573$ in thallium ($Z = 81$), so EDM measurements with heavy atoms enhance the sensitivity compared to free electron measurements and a thallium EDM experiment holds the current best limit of the eEDM **measurement with atoms** [66].

Another sensitivity enhancement can be realized with molecules. With a paramagnetic polar molecule, the valence electron moves in a steep Coulomb potential gradient due to the charge transfer associated with the chemical bond, so the relativistic effect is even larger in the molecule frame. In addition, closely spaced parity doublets in molecules allow full polarization of the molecule with a modest external electric field on the order

of V/cm [67]. In fully polarized molecules, the Stark shift due to the electron EDM

$$H_{\text{eEDM,molecule}} = \mathbf{d_e} \cdot \mathbf{E}_{\text{eff,saturated}}, \tag{4.4}$$

where the effective electric field at saturated polarization $\mathbf{E}_{\text{eff,saturated}} \sim 10$ GV/cm in heavy polar molecules such as ThO and HfF$^+$.

In the last decade, measurements in YbF [68], ThO [69, 70], and HfF$^+$ [71, 72] have set stringent constraints on the electron EDM. The latest measurement with HfF$^+$ molecules limits $|d_e| < 4.1 \times 10^{-30}$ $e$·cm with the single-source assumption, which translates to new particle mass constraints of over 40 TeV, an order of magnitude higher than the current limit of the LHC [72]. Other than the contribution from $d_e$, atomic or molecular eEDM measurements are also sensitive to the semileptonic $CP$ violation sources that couple the electron and the nucleons, so measurements from species with different relative sensitivities to leptonic and semileptonic $CP$ violation sources are needed. When we combine the HfF$^+$ experiment and the previous best limit from ThO molecules [70], they set the best simultaneous limits on the pseudoscalar-scalar electron-nucleon coupling $|C_s| < 1.9 \times 10^{-9}$ and the electron EDM $|d_e| < 2.1 \times 10^{-39}$ $e \cdot$ cm [72].

## 4.2   Hadronic $CP$ violation measurements

Although eEDM measurements give the best limits for leptonic and semileptonic $CP$ violation, they are not sensitive to $CP$ violation in the hadronic sector. Hadronic $CP$ violation measurements require probing a $T$-violating moment in a hadronic system, such as the proton or neutron EDM which arises from quark EDMs and quark chromo-EDMs [73]. Similar $T$-violating moments also occur through collective interactions of nucleons in a polarized nucleus, leading to nuclear $T$-violating moments such as the

Schiff moment and the magnetic quadrupole moment.

### 4.2.1   The nuclear Schiff moment

Hadronic $CP$ violation sources can modify the proton distribution in the nucleus to create an EDM-like moment. The nuclear Schiff moment results from this collective interaction from the protons and a direct EDM contribution from unpaired nucleons. However, the energy shift on the atom or molecule due to the nuclear $CP$ violation effects cannot be simply expressed by a nuclear EDM, as the nucleus is not a point charge. As the electron wavefunction in the nucleus is nonzero, the nucleus is not fully shielded by the electrons and the nuclear charged radius must be accounted for when calculating the energy shifts. The nuclear Schiff moment due to collective effect of protons is defined as [74, 75]

$$\mathbf{S}^{\mathrm{ch}} = \frac{e}{10} \sum_{p=1}^{Z} (r_p^2 - \frac{5}{3}\langle r^2 \rangle_{\mathrm{ch}}) \mathbf{r_p}, \tag{4.5}$$

where the sum is over all protons, $\mathbf{r_p}$ is the proton position, and $\langle r^2 \rangle_{\mathrm{ch}}$ is the mean squared radius of the nuclear charge distribution. As the Schiff moment relies on escaping the electron shielding due to the finite size of the nucleus, it is enhanced in large nuclei such as Hg [4] and Ra [52].

In addition to $\mathbf{S}^{\mathrm{ch}}$, the full Schiff moment $\mathbf{S}$ also contains a component $\mathbf{S}^N$ from EDM contribution of unpaired nucleons, but in heavy nuclei $\mathbf{S}^N$ is typically much smaller than $\mathbf{S}^{\mathrm{ch}}$, so the EDM term due to 1 or 2 unpaired nucleons can be ignored [74].

The atomic Hamiltonian due to the Schiff moment is [75]

$$H_{\mathrm{SM,atom}} = - \sum_{i=1}^{Z} \frac{3\mathbf{S} \cdot \mathbf{r_i}}{\int \rho(\mathbf{r_i}) r_i^4 dr} \rho(\mathbf{r_i}), \tag{4.6}$$

24

where the sum is over all electrons, $\mathbf{r_i}$ is the electron position, and $\rho$ is the nuclear density.

Similar as the case of eEDM in molecules, fully polarized molecules provide an interaction constant $W_S$, and [75]

$$H_{\text{SM,molecule}} = W_S \frac{S}{J} \mathbf{J} \cdot \mathbf{n}, \tag{4.7}$$

where $S$ is the nuclear Schiff moment, $\mathbf{J}$ is the nuclear spin and $\mathbf{n}$ is the internuclear unit vector.

## 4.2.2   Nuclear octupole deformation

As the Schiff moment for heavy nuclei is mostly from the collective interactions of nucleons in a polarized nucleus, a nucleus that is not reflection symmetric may enhance the Schiff moment [76]. For example, some of the radioactive nuclei such as radium-225 are octupole-deformed [77], and such octupole deformation leads to closely spaced, opposite parity states, shown in Fig. 4.1. The $T$-violating, $P$-violating interactions between the nucleons mix the two nuclear states so they are no longer equal superpositions of the two nuclear orientations, and the nuclear deformation shape fixed in the lab frame leads to enhanced collective effects. If we apply perturbation theory, the resulting Schiff moment from such a parity doublet is [74]

$$S \propto \frac{1}{\Delta E}, \tag{4.8}$$

where $\Delta E$ is the nuclear parity doublet splitting. This splitting is 55 keV for $^{225}$Ra [76], and could be $< 100$ eV for $^{229}$Pa [78] (half-life 1.5 d). Compared to a heavy reflection-symmetric nucleus such as $^{199}$Hg which lacks a closely spaced parity doublet, the Schiff moment of $^{225}$Ra is enhanced by $\sim 100 - 1000$ times, and the $^{229}$Pa nucleus may give an

additional enhancement factor of $\sim 1000$ over $^{225}$Ra ($10^5 - 10^6$ over $^{199}$Hg) [79].
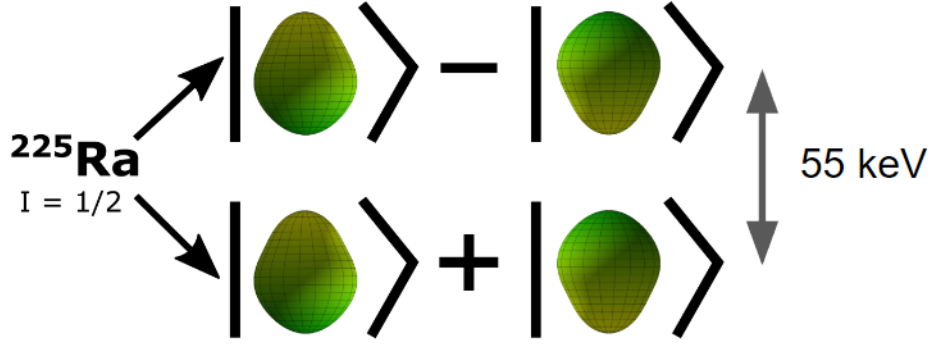


Figure 4.1: The two lowest nuclear energy state in radium-225 which forms an opposite parity doublet states. $P$, $T$-violating interactions in the radium-225 nucleus could mix the two states and lead to a non-zero nuclear Schiff moment.

### 4.2.3 Hadronic $CP$ violation in SM and BSM operators

Hadronic $CP$ violation measurements are sensitive to both $CP$ violation in the Standard Model (SM) strong interaction and additional $CP$ violation sources in physics beyond the Standard Model (BSM). To evaluate the sensitivity of a hadronic $CP$ violation measurement to the various sources, we need to write out the measured moment, such as the nuclear Schiff moment, in terms of hadronic $CP$ violation operators.

As discussed in Section 4.2.1, the Schiff moment comes from two sources: A collective effect of nucleons and EDMs of unpaired nucleons. Both of these terms are generated by pion-nucleon couplings that are $CP$-odd. Therefore, in general we can write the Schiff moment as [74]

$$S = \frac{2m_N g_A}{F_\pi}(a_0 \bar{g}_\pi^{(0)} + a_1 \bar{g}_\pi^{(1)} + a_2 \bar{g}_\pi^{(2)}), \tag{4.9}$$

where $m_N$ is the nucleon mass, $g_A$ is a quark coupling term, $F_\pi$ is the pion decay constant, $\bar{g}_\pi^{(i)}$ are the scalar (0), vector (1), and tensor (2) $CP$-violating pion-nucleon couplings, and their $a_i$ are sensitivity constants that can be determined from nuclear structure.

The prefactor in Eq. 4.9, $2m_N g_A/F_\pi \approx 13.5$ [74]. The Schiff moment from the same $CP$-violating physics would be larger for a nucleus with greater $a_i$ constants.

The Standard Model contribution to hadronic $CP$ violation is from the $\bar{\theta}$ term, which describes $CP$ violation in quantum chromodynamics (QCD). Currently, $CP$ violation in the strong interaction has never been observed, and experimental results [3, 4] have constrained $\bar{\theta} < 10^{-10}$, which is very far from a order of unity value, which is expected from the naturalness perspective. This lack of $CP$ violation in the strong interaction is the so-called strong $CP$ problem. The scaling of $\bar{g}_\pi^{(0)}$ from $\bar{\theta}$ is [80] [1]

$$\bar{g}_\pi^{(0)} = \bar{\theta}\frac{m_\pi^2}{M_{\mathrm{QCD}}F_\pi},\tag{4.10}$$

where $m_\pi$ is the pion mass, and $M_{\mathrm{QCD}} \sim 2\pi F_\pi$.

The scaling of $\bar{g}_\pi^{(i)}$ from new physics terms can also be calculated. For example, the scaling for quark chromo-EDM terms is [81]

$$\bar{g}_\pi^{(1)} = 2 \times 10^{14}(\tilde{d}_u - \tilde{d}_d),\tag{4.11}$$

where $\tilde{d}_u$ and $\tilde{d}_d$ are the chromoelectric dipole moments of the up and down quarks in units of cm.

New physics may also include other terms that can contribute to $\bar{g}_\pi^{(i)}$, including four-quark operators, quark EDMs, and chiral-invariant sources in the pion-nucleon sector [80]. Semi-leptonic $CP$ violation sources from electron-nucleon interactions can also lead to an EDM-like signal [82, 4]. These many sources of $CP$ violations call for using different experimental systems to constrain each $CP$ violation source with a global analysis of all experiments [83, 84].

---

[1]The definition of $\bar{g}_\pi^{(i)}$ in [80] is a factor of $F_\pi$ smaller than the [74] definition that we use in this thesis.

The current best limit on the QCD $\tilde{\theta}$ term is placed by a neutron EDM experiment at $\tilde{\theta} < 4.6 \times 10^{-11}$ [3, 85]. The same measurement constrains $|\tilde{d}_d + 0.5\tilde{d}_u| < 3.3 \times 10^{-26}$ cm [73]. The latest mercury EDM measurement constrains $\tilde{\theta} < 1.5 \times 10^{-10}$, and $|\tilde{d}_u - \tilde{d}_d| < 5.6 \times 10^{-27}$ cm [4]. All of these limits are placed with the assumption that there is only a single source of $CP$ violation.

## 4.2.4   Hadronic $CP$ violation measurements with radioactive molecular ions

We are working towards hadronic $CP$ violation measurements using radioactive molecular ions such as $^{225}$RaSH$^+$ and $^{229}$PaSH$^+$. Compared to state-of-the-art hadronic $CP$ violation measurements with Hg atoms, octupole deformed nuclei such as $^{225}$Ra and $^{229}$Pa provide orders of magnitude larger Schiff moments. In addition, in these polar molecules, the molecular interaction constant $W_S$ is large. These combined enhancement factors make radioactive molecules the highest sensitivity to hadronic $CP$ violation per particle.

To realize the large molecular enhancement, the molecule must be fully polarized. This requires mixing closely spaced, opposite parity states with a small lab-frame electric field so that the molecular orientation is defined in the lab frame. The eEDM experiments use paramagnetic molecules, which have $\Omega$-doublets in all states with electronic angular momentum $J_e \geq 1$ [67]. However, the radioactive molecular ions considered for hadronic $CP$ violation measurements are all diamagnetic molecules with no $\Omega$-doublet in the ground $\Sigma$ electronic state [2], so we need to use another doubling mechanism, such as vibrational $l$-, or rotational $K$-doublets with polyatomic molecules [86, 87, 88]. The rotational or vibrational doublets allow full molecule polarization at electric fields as low

---

[2]Diamagnetic molecules are less sensitive to systematics such as the fluctuations of the magnetic field, so most hadronic $CP$ violation measurements use them.

as a few V/cm in a rotational or vibrational excited state, and they are independent of the molecular electronic structure so the same measurement principle can be applied to any of the radioactive nuclei we choose.

For the proposed hadronic $CP$ violation experiment, a radioactive molecular ion will be co-trapped with a single $^{225}\text{Ra}^+$ ion. The laser-cooled $^{225}\text{Ra}^+$ ion can be used to sympathetically cool, control, and readout the molecular ion via quantum logic spectroscopy. The quantum logic spectroscopy technique has been demonstrated to control the state of a diatomic molecular ion $\text{CaH}^+$ [16, 89], and it has also been used to operate an $\text{Al}^+$ ion optical clock [5], which is one of the most precise measurements that ever realized. We will discuss more on the details of the proposed measurement in Chapter 12.

We expect up to order of magnitudes gain in the sensitivities for the proposed hadronic $CP$ violation experiments with radioactive molecules. Generally, the sensitivity of a frequency measurement is

$$\delta f = \frac{1}{2\pi\tau\eta}\sqrt{\frac{\tau + t_\text{d}}{NT}}, \tag{4.12}$$

where $\tau$ is the measurement coherence time, $\eta$ is the state preparation and detection fidelity, $t_\text{d}$ is the dead time between measurements, $N$ is the number of particles, and $T$ is the total measurement time.

The proposed measurements consider a single radioactive molecular ion ($N = 1$), and a near-unity efficiency can be enabled by quantum logic spectroscopy ($\eta \approx 1$). A coherence time of $\tau \sim 1$ s should be achievable in a proof-of-concept measurement [72], and $\tau \sim 1000$ s is possible with noise-mitigation techniques, such as magnetic field stabilization and shielding [4, 90]. The dead time for state preparation and readout, $t_\text{d}$, should be short compared to the coherence time $\tau$. For a month long measurement, we can achieve a statistical frequency sensitivity of $\sim 163\ \mu\text{Hz}$ for $\tau = 1$ s and $\sim 5\ \mu\text{Hz}$ for $\tau = 1000$ s (90% confidence interval).

We can estimate the constraints on the Schiff moment from these proposed measurements assuming the Schiff moment values that agree with zero. For a polyatomic molecule such as $RaOH^+$, the molecular interaction constant is estimated to be $W_S \approx 3 \times 10^4$ a.u. (a.u.$= e/(4\pi\epsilon_0 a_0^4)$, where $\epsilon_0$ is the vacuum permittivity, and $a_0$ is the Bohr radius) [91], and $\mathbf{J} \cdot \mathbf{n}/J = 0.5$ for comparison between opposite Schiff moment sensitivity states in a fully polarized polyatomic molecule [87]. We can calculate the Schiff moment bounds from Eq. 4.7, $|S| < 2.5 \times 10^{-10}$ e fm$^3$ for $\tau = 1$ s and $|S| < 7.5 \times 10^{-12}$ e fm$^3$ for $\tau = 1000$ s. For a radium-225 nucleus, $a_0 = -2.6$ e fm$^3$, $a_1 = 12.9$ e fm$^3$, and $a_2 = -6.9$ e fm$^3$ [91] in Eq. 4.9. The corresponding constraints in $CP$ violation sources for the $\tau = 1$ s measurement is comparable to the current best constraints, and is one to two orders of magnitudes smaller for $\tau = 1000$ s [91]. If protactinium-229 is used instead of radium-225, the very close nuclear parity doublet potentially in $^{229}$Pa could lead to hundreds or thousands of times of higher sensitivity than the radium-225-containing molecules [79].

# Chapter 5

# Atom-light interactions

In this chapter we discuss atom-light interactions that are relevant to this thesis.

## 5.1 Doppler cooling

Doppler cooling is an important technique in our work. It can reduce the kinetic energy of the trapped ions from hundreds of Kelvins to $\sim 1$ milliKelvin, and enables other techniques such as sideband cooling to cool the ions to the motional ground state in the trap pseudo-potential. In this section we briefly introduce Doppler cooling, and discuss Doppler cooling in the $S_{1/2} - P_{1/2} - D_{3/2}$ structure of strontium and radium ions.

### 5.1.1 Doppler cooling with a two-level system

Doppler cooling uses red-detuned light to slow down the motion of the atoms. When an atom moves towards the light propagating direction, the Doppler shift moves the light frequency closer to the resonance and the atom is more likely to absorb a photon. When the atom is moving away, it is less likely to absorb an photon. The difference in probability of absorbing photons results in velocity-dependent momentum "kicks" to

slow down the atoms. For atoms in free space, it typically needs two counter-propagating beams to cool the atoms in both directions of 1D, and a total of six lasers to cool the atoms in 3D. For trapped ions, the normal modes of motion are well-defined, so a red-detuned laser with nonzero $k$-vector components on all three secular motional modes is sufficient. Most of the trapped ion experiments do not use a counter-propagating laser, so the light pressure from the cooling laser pushes the ion slightly off the trap center, which can be ignored since the light scattering force is typically small compared to the Coulomb force from the trapping potential.

At very low temperatures, the random-walk heating from absorption and emissions is in equilibrium with the cooling, and results in a Doppler cooling temperature limit

$$T_{\mathrm{D}} = \frac{\hbar\Gamma}{2k_{\mathrm{B}}},\tag{5.1}$$

where $\Gamma$ is the natural linewidth of the transition. This limit is only obtained for laser detuning $\delta = -\Gamma/2$ with a small Rabi frequency $\Omega \ll \Gamma$. For the Sr$^+$ or Ra$^+$ ions, the cooling transition has a natural linewidth of $\Gamma \approx 2\pi \times 20$ MHz, corresponding to a Doppler cooling limit of $\sim 0.5$ mK.

## 5.1.2   Doppler cooling of $^{88}$Sr$^+$ or $^{226}$Ra$^+$

Due to the low-lying metastable $D_{3/2}$ state, Sr$^+$ or Ra$^+$ have a $\Lambda$-shaped energy level diagram and require two lasers for Doppler cooling. Typically we use the $S_{1/2} \to P_{1/2}$ transition as the Doppler cooling transition, and the laser driving the transition is red-detuned. The $D_{3/2} \to P_{1/2}$ transition is used as a repumping transition into the Doppler cooling cycle. This assignment of cooling and repumping transitions is due to the branching fraction of the $P_{1/2}$ state, which predominately decays to the $S_{1/2}$ state ($p = 94\%$ for Sr$^+$ [92], and $p = 91\%$ for Ra$^+$ [7]). We discuss the specific requirements

on the two lasers for cooling isotopes with no hyperfine structure ($^{88}$Sr$^+$ or $^{226}$Ra$^+$) to approximately the Doppler limit in the following text.

**Rabi frequency requirements**

Significant broadening or shifting of the cooling transition spectrum should be avoided to reach the Doppler limit, so the Rabi frequencies of the cooling and repumping lasers should be selected to minimize broadening effects on the cooling transition. For simplicity, we ignore the Zeeman sublevels in each of the electronic state, so the problem can be simplified to a three-level system.

First of all, the Rabi frequency of the cooling laser $\Omega_{SP}$ should be smaller than the transition natural linewidth $\Gamma$. If $\Omega_{SP} \gg \Gamma$, power broadening increases the transition linewidth and the ion temperature is much higher than the Doppler limit.

If the repumping laser has a very small Rabi frequency ($\Omega_{DP}^2/(1-p) \ll \Omega_{SP}^2/p$), the repumping rate from the $D_{3/2}$ state is small and the ion spends much longer time in the $D_{3/2}$ state than the $S_{1/2}$ state. In this case, the scattering rate is solely determined by the repumping rate, leading to broadening of the cooling laser spectrum as the scattering rate is no longer sensitive to the detuning of the cooling laser [93].

If the repumping laser transition rate is faster than the cooling laser transition rate ($\Omega_{DP}^2/(1-p) > \Omega_{SP}^2/p$), the ion spends shorter time in the $D_{3/2}$ state than the $S_{1/2}$ state, so the cooling transition broadening from the $D_{3/2}$ state population is small. However, if the repumping laser Rabi frequency is much greater than the natural linewidth, the cooling laser transition spectrum would be significantly distorted and shifted due to the ac Stark shift, which is generally unwanted in an experiment.

To summarize, the requirements on the cooling and repumping Rabi frequencies are

$$\Omega_{SP} < \Gamma, \tag{5.2}$$

$$\sqrt{\frac{1-p}{p}}\Omega_{SP} < \Omega_{DP} < \Gamma. \tag{5.3}$$

**Polarization requirements**

The Zeeman sublevels in the three electronic states impose additional requirements on the cooling and repumping lasers. First, there cannot be a dark state that the lasers cannot access. For example, if the cooling laser $k$-vector and polarization is set so that only the $\sigma^+$ transitions are driven, then the population which decays to the $S_{1/2}, m = +1/2$ Zeeman sublevel does not interact with the laser so the laser cooling rate drops to zero. Similarly, if the repumping laser only drives one type of transition in $\sigma^+$, $\pi$, and $\sigma^-$, there will be always two Zeeman sublevels in the $D_{3/2}$ state that are dark [93]. The polarization and $k$-vector requirements on the two lasers to prevent dark Zeeman sublevels in both the $D_{3/2}$ state and the $S_{1/2}$ state are

- The cooling laser must drive $\pi$ transitions or simultaneously drive $\sigma^+$ and $\sigma^-$ transitions. A simple way to satisfy this requirement is to set the cooling laser polarization to be linearly polarized.

- The repumping laser must simultaneously drive both $\sigma^+$ and $\sigma^-$ transitions. For example, the repumping laser can be set to a linear polarization that is not parallel with the magnetic field.

**Magnetic field and laser detuning requirements**

In addition to the dark states of single Zeeman levels, a coherent dark state can occur where a coherent state composed of Zeeman sublevels in the $D_{3/2}$ state has zero transition

rate to all of the $P_{1/2}$ sublevels. Two such states exist for any polarization and $k$-vector of the repumping laser [93]. If the state of the ion approaches one such state, it would stay in the state forever unless the state is destabilized. One of the methods to destabilize such a coherent dark state is to apply an nonzero magnetic field [93]. If the magnetic field is nonzero, the phase in each of the components of the dark state is time-dependent, and the destabilization rate depends on the Zeeman shift due to the magnetic field. In typical laser cooling conditions, we want the destabilization rate to be similar or larger to the repumping rate, $\mu_B B \gtrapprox \Omega_{DP}$.

In addition to the coherent dark states within the $D_{3/2}$ state, cooling and repumping lasers can induce Raman transitions that coherently transfer population between the $S_{1/2}$ and the $D_{3/2}$ states and lead to dark states between Zeeman sublevels in the $S_{1/2}$ state and the $D_{3/2}$ state [93]. If the frequency difference between the cooling and repumping lasers drives an allowed Raman transition between two Zeeman sublevels, population moves between the two Zeeman sublevels directly and there would be no excitation to the $P_{1/2}$ state and thus no Doppler cooling. To avoid this, the repumping laser needs to be blue detuned so the Zeeman shift is not large enough to account for the detuning difference between the red-detuned cooling laser and blue-detuned repumping laser. Assuming a typical cooling laser detuning of $-\Gamma/2$ and repumping laser detuning of $+\Gamma/2$, the magnetic field should satisfy $\mu B \ll \Gamma$.

Therefore, the requirements on the laser detunings and the magnetic fields are

$$\Delta_{SP} \sim -\frac{\Gamma}{2}, \tag{5.4}$$

$$\Delta_{DP} \sim +\frac{\Gamma}{2}, \tag{5.5}$$

$$\Omega_{DP} \lessapprox \mu_B B \ll \Gamma. \tag{5.6}$$

All of the above intensity, polarization, laser detuning, and magnetic field require-

ments need to be satisfied for laser cooling close to the Doppler limit.

## 5.2    Coherent driving of the electric quadrupole transition

Both $Sr^+$ and $Ra^+$ ions have the $S_{1/2} \rightarrow D_{5/2}$ electric quadrupole ($E2$) transition that have narrow natural linewidths. As the natural linewidth is much smaller than typical $\sim$ kHz Rabi frequencies for this transition and the $\sim$ MHz Zeeman splittings, the transitions between different Zeeman sublevels are resolved and each of them can be viewed as a two-level system.

### 5.2.1    Secular motion control

The ions are also trapped in a pseudo-potential that is a 3D harmonic oscillator. The corresponding motional states (phonon states) are shared among all ions, so the motion can be used to transfer information between trapped ions for building multi-ion quantum gates. A laser driving a transition could perturb the harmonic oscillator potential and lead to transitions that change the motional state of the harmonic oscillator. According to conservation of energy, these transitions must be spaced by the secular frequencies of the ion, and these transitions are called the secular sidebands, which can be used to control the motional quantum numbers in the trap 3D harmonic oscillator.

**Lamb-Dicke parameter**

An important parameter in light interaction with a motional mode of a trapped ion is the Lamb-Dicke parameter

$$\eta = k \cos\theta \sqrt{\frac{\hbar}{2m\omega_i}}, \tag{5.7}$$

where $k$ is the wavenumber of the light, $m$ is the mass of the trapped ion, $\omega_i$ is the secular frequency on axis $i$, and $\theta$ is the angle between the light wavevector and axis $i$. The Lamb-Dicke parameter describes the ratio between the motional state wavefunction spread to the light wavelength, and characterizes the Rabi frequencies of the sideband transitions [94]

$$\Omega_{n,n+m} = \Omega e^{-\eta^2/2} \eta^{|m|} L_n^{|m|}(\eta^2) \left( \frac{n!}{(n+m)!} \right)^{\text{sign}(m)/2},$$  (5.8)

where $\Omega_{n,n+m}$ is the Rabi frequency of the sideband transition from motional state $n$ to motional state $n+m$, $\Omega$ is the Rabi frequency for a free-space atom, and $L_n^\alpha$ is the associated Laguerre polynomial

$$L_n^\alpha(x) = \sum_{k=0}^{n} (-1)^k \binom{n+\alpha}{n-k} \frac{x^k}{k!}.$$  (5.9)

**Lamb-Dicke regime**

The Lamb-Dicke parameter is typically small for an ion trap that is designed for motional sideband control of trapped ions. For example, for the $S_{1/2} \rightarrow D_{5/2}$ clock transition of $^{226}\text{Ra}^+$ (728 nm) with a secular frequency of $2\pi \times 1$ MHz, $\eta = 0.04$ when the laser is parallel to the secular mode. With the approximation $\eta \ll 1$ and $n \sim 1$, we can apply Taylor expansion on Eq. 5.8, so Rabi frequencies of the carrier and 1st-order red and blue sideband transitions can be simplified to [94]

$$\Omega_{n,n} = \Omega(1 - \eta^2 n),$$  (5.10)

$$\Omega_{n,n-1} = \eta \sqrt{n} \Omega,$$  (5.11)

$$\Omega_{n,n+1} = \eta \sqrt{n+1} \Omega.$$  (5.12)

When $\Omega_{n,n}^2 \gg \Omega_{n,n-1}^2 + \Omega_{n,n+1}^2$, spontaneous decays from the excited state are unlikely to change the motional quantum number of the ion (the Rabi frequencies for higher order sidebands are even smaller so they are not considered). This is the so-called Lamb-Dicke regime, where

$$\eta^2(2n+1) \ll 1. \tag{5.13}$$

In the Lamb-Dicke regime, the Rabi frequencies for the first order sidebands are much smaller than the carrier Rabi frequency, and the higher order sidebands are even further suppressed. Therefore, when driving a typical dipole transition where the natural linewidth $\Gamma \gg \omega_i$, the motional number is unlikely to be changed when the ion is in the Lamb-Dicke regime. However, when driving a sideband resolved transition where $\Gamma \ll \omega_i$, the desired sideband to drive can be selected by detuning the laser, which makes sideband cooling of a trapped ion possible.

**Sideband cooling**

Doppler cooling alone can only decrease the temperature of the trapped ion to near the Doppler limit $\sim 0.5$ mK, which corresponding to a mean motional quantum number $\bar{n}_i \sim 10$ for a secular frequency $\omega_i = 2\pi \times 1$ MHz. At this point, the ion is in a thermal state following the Bose-Einstein distribution. To further cool the ion, we need to use sub-Doppler cooling techniques such as sideband cooling [95].

Sideband cooling relies on using a transition with linewidth $\Gamma < \omega_i$, where $\omega_i$ is the secular frequency of the motional mode to be cooled. For $\text{Sr}^+$ and $\text{Ra}^+$, the $S_{1/2} \rightarrow D_{5/2}$ transition is usually chosen. This transition has resolved sidebands, meaning that each secular sideband can be driven by detuning the laser without much off-resonant scattering on the other sidebands or the carrier transition. Therefore, the first-order red sideband

can be driven to reduce the motional quantum number of the ion by 1. If only this transition is continuously driven, the motional quantum number cannot be decreased by more than 1: Although the absorption process removes a phonon from the motional mode, the stimulated emission process adds a phonon. Due to the long lifetime of the $D_{5/2}$ state, a unidirectional dissipation process is needed to reset the ion to the $S_{1/2}$ state from the $D_{5/2}$ without changing the motional quantum number. This can be realized by driving the $D_{5/2} \rightarrow P_{3/2}$ "cleanout" dipole transition which pumps the population back to the $S_{1/2}$ state. By continuous driving of both the cleanout transition and the red sideband of the clock transition, the motional quantum number of the trapped ion can be reduced to a sideband cooling temperature limit determined from off-resonant scattering and spontaneous decays that changes the motional quantum number of the trapped ion.

In practice, there are multiple Zeeman sublevels in each of the electronic state of $^{88}\text{Sr}^+$ and $^{226}\text{Ra}^+$, so we must prepare the ion to a single Zeeman sublevel of the $S_{1/2}$ state before sideband cooling can be done. This can be done by driving either $\sigma^+$ or $\sigma^-$ transition of the Doppler cooling transition (polarization-based state preparation) or driving clock transitions between specific Zeeman sublevels (frequency-based state preparation). In this thesis all state preparation is done by driving specific Zeeman sublevels of the clock transitions. For example, to prepare the ion into the $S_{1/2}$, $m = +1/2$ state, we drive the $S_{1/2}, m = -1/2 \rightarrow D_{5/2}, m = +3/2$ transition while applying the cleanout and repumping light to optically pump the population to the desired Zeeman sublevel in the ground state. The repumping light is necessary as the $D_{5/2}$ has a small but nonzero branching fraction to the $D_{3/2}$ state.

After state preparation into the $S_{1/2}$, $m = +1/2$ sublevel, we drive the first-order red sideband of the $S_{1/2}, m = +1/2 \rightarrow D_{5/2}, m = +5/2$ transition to sideband cool while applying the cleanout and repumping light. We choose to excite to the $m = +5/2$ Zeeman sublevel of the $D_{5/2}$ state because this sublevel can only be excited to $P_{3/2}, m = +3/2$,

and decay to $S_{1/2}, m = +1/2$ which forms a closed cooling loop if we do not consider the

$P_{3/2}$ state branching fractions to the $D_{3/2}$ and the $D_{5/2}$ states. In practice, branchings

to the $D$ states require interleaving state preparation pulses and sideband cooling pulses

to get reliable sideband cooling results to the sideband cooling limit.

If Doppler cooling is not sufficient to cool the ion into the Lamb-Dicke regime, e.g.

when the secular frequencies are small $\omega_i \ll 2\pi \times 1$ MHz, the sideband cooling states in

the regime where Eqs. 5.11 and 5.12 are no longer valid and higher order contributions

from $\eta$ must be considered. For example, the Rabi frequencies for the carrier and low-

order sidebands are plotted in Fig. 5.1 with Eq. 5.8 for $\eta = 0.13$.
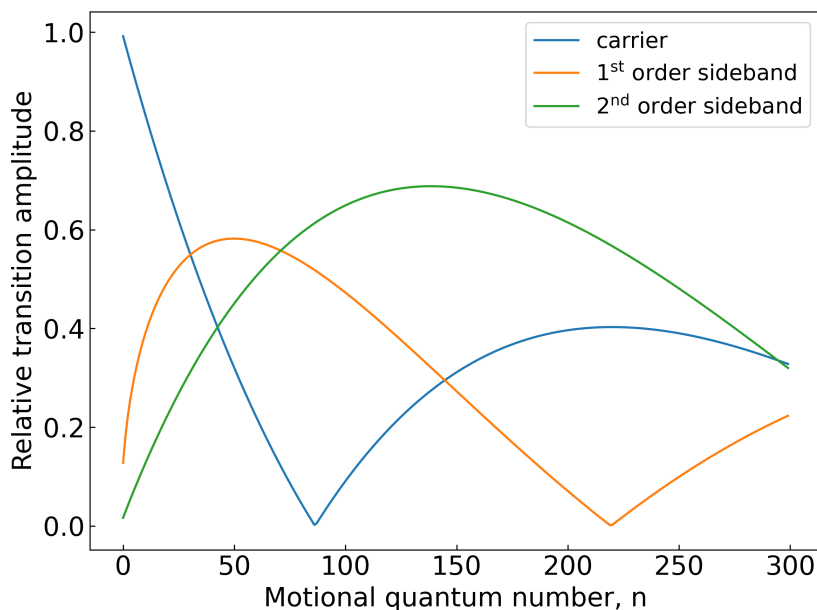


Figure 5.1: Relative Rabi frequencies of the carrier, first order sideband, and second order blue sideband for different motional quantum number for a single $^{226}$Ra$^+$ with a $2\pi \times 100$ kHz secular frequency ($\eta = 0.13$). The red sidebands have similar secular frequencies as the blue sidebands for $n > 0$. If the motional quantum number $n \sim 220$, the Rabi frequency of the first-order sideband approaches zero, stopping the cooling process, and higher-order red sidebands need to be driven to overcome these barriers [96].

Sideband cooling can also be done with the $S_{1/2} \rightarrow D_{3/2}$ $E2$ transition. However, the

laser to drive this transition is typically not available in most alkaline-earth ion trapping

experiments due to state detection techniques that will be discussed in Section 5.3.

**Thermometry**

Temperature measurements of the trapped ions can be done to confirm the results of Doppler cooling and sideband cooling.

First, the temperature of the ions can be estimated from the spatial extent seen on the camera. This technique is limited by the resolution of the imaging system, typically $\sim 1~\mu$m. Although this technique is usually not useful to determine the ion temperature in the quantum regime where the mean motional quantum number is small, it provides confirmation of ion crystallization and makes sure that the ion temperature $T \lesssim 1$ K.

After the trapped ions are crystallized, a spectroscopy of the dipole transitions, such as the $S_{1/2} \to P_{1/2}$ cooling transition can help checking the temperature of the ions. If the temperature of the ions is at the Doppler limit, the Doppler shift is $\sim 2\pi \times 1$ MHz, significantly smaller than the natural linewidth $\Gamma \sim 2\pi \times 20$ MHz, so the Doppler-induced transition broadening effect should be negligible.

More precise thermometry measurements typically rely on driving the $S_{1/2} \to D_{5/2}$ clock transition. One method is to measure the motion-induced decoherence on the carrier transition of the clock transition. According to Eq. 5.10, the Rabi frequencies of the carrier transition for different motional quantum number $n$ is different, so we can measure the decoherence rate of the carrier transition due to the thermal distribution of the motional quantum number to determine the mean motional quantum number of the trapped ion. Assuming that the motional state occupancies follow the Bose-Einstein distribution, the population in the excited state as a function of time for Rabi flopping on the carrier transition is [94] [1]

---

[1] The definition of the Rabi frequency differs from Eq. A.5 in [94] by a factor of 2. This re-definition follows the usual convention, e.g. [97].

$$p(t) = \frac{1}{2} - \frac{\cos(\Omega t) + \eta^2 \bar{n} \Omega t \sin(\Omega t)}{2(1 + (\eta^2 \bar{n} \Omega t)^2)}, \tag{5.14}$$

where $\bar{n}$ is the mean motional quantum number. If the laser is not parallel to a motional state or multiple ions are trapped, multiple motional modes contribute to the motional decoherence, and the temperatures of individual motional modes cannot be determined from this method. While this method is effective in probing the temperature of a single motional mode when $\bar{n}$ is relatively high, other decoherence mechanism such as magnetic field fluctuation may dominate at low $\bar{n}$, which may overestimate of the ion temperature with Eq. 5.14.

When the temperature of the ion is near the ground state ($\bar{n} \lesssim 1$), either direct measurements of the sideband heights or Rabi flopping on the sidebands can be used to measure the temperature accurately. At low $\bar{n}$, motional decoherence on the sidebands are much more evident than the carrier due to the large dependence of sideband Rabi frequencies as a function of the motional quantum number (See Eqs. 5.11 and 5.12). Alternatively, the first-order red and blue sideband heights can be probed directly, and the population in the motional ground state can be calculated from the ratio between the red and blue sideband [94]

$$P(n = 0) = 1 - \frac{p_{\text{red}}}{p_{\text{blue}}}, \tag{5.15}$$

where $p_{\text{red}}$, $p_{\text{blue}}$ are the red and blue sideband heights. These two methods based on the secular sidebands provide direct temperature measurements in a single motional mode.

## 5.3   State detection

The $S_{1/2} \to D_{5/2}$ transition provides a way to coherently manipulate the two clock states. In this section we discuss how to determine whether the ion is in the $D_{5/2}$ or the $S_{1/2}$ state.

State detection uses the same lasers as Doppler cooling, the cooling laser driving the $S_{1/2} \to P_{1/2}$ transition and the repumping laser driving the $D_{3/2} \to P_{1/2}$ transition. As the two lasers form a closed loop, we can observe continuous fluorescence from the ion if the ion is in the ground $S_{1/2}$ state. On the other hand, the upper state of the clock transition, $D_{5/2}$ state, is out of the Doppler cooling loop, so the ion does not emit fluorescence when the two lasers are on.

As the $D_{5/2}$ state lives for hundreds of milliseconds for $Sr^+$ and $Ra^+$, a state detection for $\sim 1$ ms introduces an error that is less than 1% due to spontaneous decay of the upper state. For a typical imaging system that collects $\sim 0.1\%$ of the fluorescence photons, the fluorescence photon rate from a single ion collected by a PMT is $\sim 20$ kHz, while the background photon rate on the PMT is $\lessapprox 1$ kHz. State detection for 1 ms on average collects $\sim 20$ photons when the ion is in the $S_{1/2}$ state, and $< 1$ photon when the ion is in the $D_{5/2}$ state. A state detection threshold of $\sim 5$ can be used to distinguish the two events with $< 0.01\%$ Poisson error for either state.

## 5.4   Quantum logic spectroscopy

The techniques discussed previously, including state preparation, sideband cooling, and state detection enable the quantum logic spectroscopy technique. The quantum logic spectroscopy was first demonstrated for spectroscopy of $Al^+$ ions [15]. It was then used for precision spectroscopy of diatomic $CaH^+$ molecule [16], an $Al^+$ optical ion clock [5],

and an $Ar^{13+}$ optical clock [98]. With this technique, we can prepare and detect the internal state of a radioactive molecular ion via a co-trapped $Ra^+$ ion.
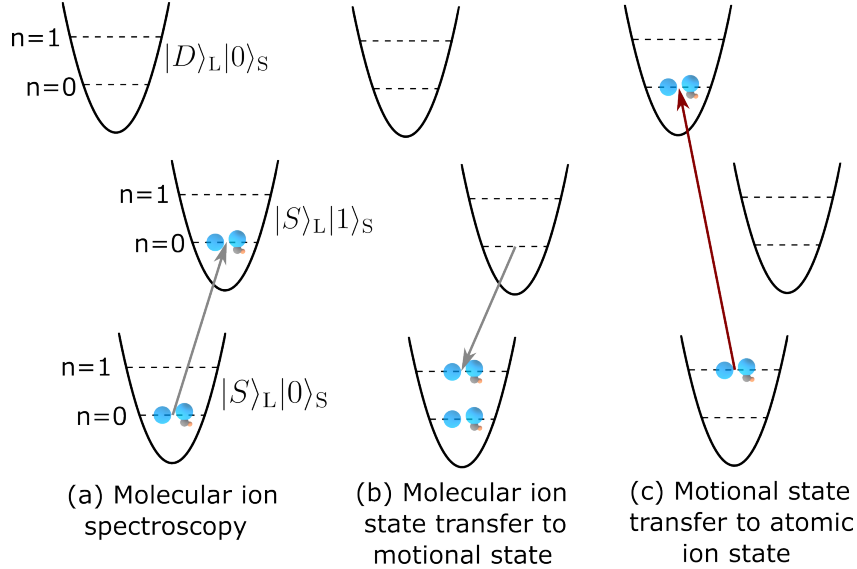


Figure 5.2: Quantum logic spectroscopy pulse sequence for a $RaSH^+$ molecular ion co-trapped with a $Ra^+$ ion after sideband cooling to the ground motional state. Each harmonic oscillator potential in the figure represents a two-qubit state. The logic ion $Ra^+$ can be in either the $|S\rangle_L$ ($S_{1/2}$) or the $|D\rangle_L$ ($D_{5/2}$) state. The spectroscopy ion $RaSH^+$ can be in either the $|0\rangle_S$ ground state or the $|1\rangle_S$ excited state. The two relevant motional state, $n = 0$ and $n = 1$ are shown in the figure. See the main text for a detailed explanation of the sequence.

For quantum logic spectroscopy, we first co-trap a $Ra^+$ (logic ion) and a molecular ion such as $RaSH^+$ (spectroscopy ion) and use sideband cooling on $Ra^+$ to cool a shared motional mode of the ion chain to the ground motional state. After sideband cooling, we use the pulse sequence shown in Fig. 5.2 for quantum logic spectroscopy: We apply a spectroscopy pulse on the molecular ion, which may be on-resonance so that it prepares the molecular ion to an excited state or off-resonance which does not change the molecular ion state. A red sideband pulse on the same transition of the molecular ion follows, which attempts to drive the molecular ion to the ground state and increase the shared motional mode quantum number by one if the transition is driven. After that, a red sideband pulse on the $Ra^+$ clock transition tries to drive the radium ion into the $D_{5/2}$ state, which

44

is possible only if the shared motional mode is in the $n = 1$ state. Through the steps, the quantum information in the molecular ion is transferred (the spectroscopy pulse succeeds or fails) to the motional state (motional quantum number $n = 1$ or $n = 0$), and then to the Ra$^+$ ion (ion is in the $D_{5/2}$ or the $S_{1/2}$ state). Finally state detection can be used to determine the state of the Ra$^+$ ion. Thus, a one-to-one mapping between the molecular ion state and the Ra$^+$ state is established, and this technique is generally applicable to any ion that has a mass-to-charge ratio similar to that of Ra$^+$.

Due to the high fidelity of single ion motional state control operations and state detections, the quantum logic spectroscopy technique can reach a high efficiency near unity. This enables efficient state preparation and detection for ions with complicated internal structures, such as molecular ions with a laser-cooled ion.

# Chapter 6

# Ion trapping apparatus

This chapter introduces the ion trap and associated apparatus for all $^{226}\mathrm{Ra}^+$ ion work in this thesis.

## 6.1   Ion trap

We use a linear Paul trap with $r_0 = 3$ mm and $z_0 = 7.5$ mm, a geometry used by the Hudson group at UCLA [99]. See Fig. 2.1 for a render of the ion trap. The z-geometry factor is experimentally measured to be $\kappa = 0.2005$. This trap is designed for relatively low rf driving frequencies $\Omega_{\mathrm{rf}} \sim 2\pi \times 1$ MHz that is compatible with the time-of-flight electronics in [100]. The trap does not have separate micromotion compensation electrodes, and micromotion compensation electric fields are applied by dc bias voltages on the radial electrodes.

## 6.2   Trap drive electronics

For initial trapping and cooling of radium ions [7], we use the electronics described in [100] which supports time-of-flight mass spectrometry of trapped ions. The trap drive frequency is $\Omega_{\mathrm{rf}} = 2\pi \times 2.1$ MHz. However, we have observed significant ion heating with these electronics. Without laser cooling, in a few seconds a crystallized ion is heated so it is no longer crystallized. We identified that the heating is mostly from rf electric field noise due to the driving electronics: The four rf electrodes are driven by independent rf resonators and rf sources, so the phase noise of the rf sources at the trap center does not cancel which contributes to heating. The time-of-flight mass spectrometry setup, which was removed after trapping and cooling of radium ions, is introduced with more details in [61].

To address the heating problem, we built new electronics that drive all rf electrodes from the same rf source and resonator, using a design similar to [101]. The schematic of the electronics is shown in Fig. 6.1. We use a homemade center-tapped toroidal resonator that provides out-of-phase rf voltages for the two pairs of radial electrodes. A Micrometal T200-2 iron toroid is used as the resonator core. Bias tee circuits are used to allow applying independent dc voltages on these electrodes for micromotion compenastion. All rf outputs from the electronics connect to the trap electrodes via 1 m long RG-316 cables with SMB connectors.
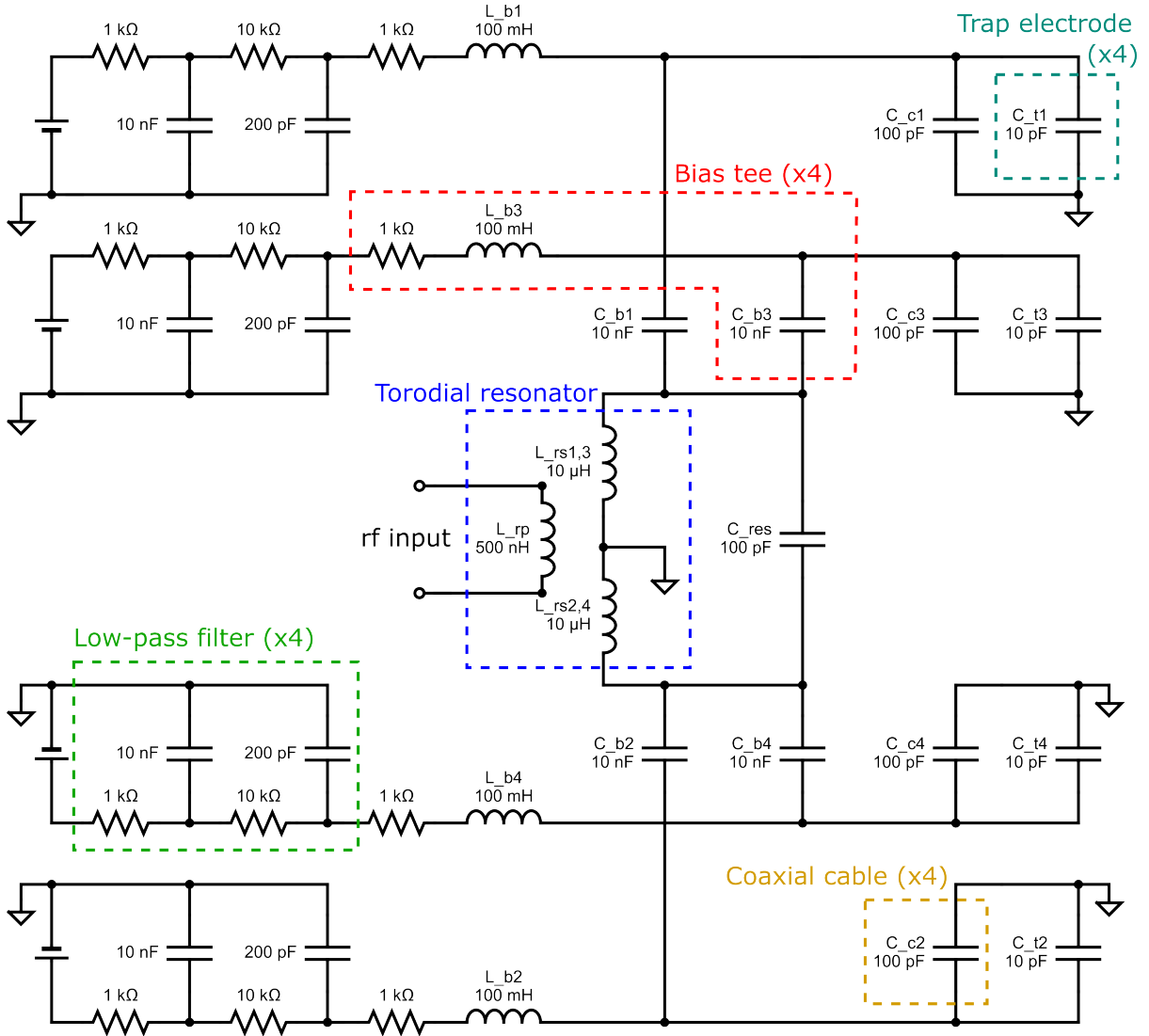
Figure 6.1: Custom trap driving electronics for $\sim 2\pi \times 2$ MHz driving frequency. The electrode pairs 1, 3 and 2, 4 are of the opposite rf phase. A slightly different version for $\sim 2\pi \times 1$ MHz driving frequency is finalized and used in this work.
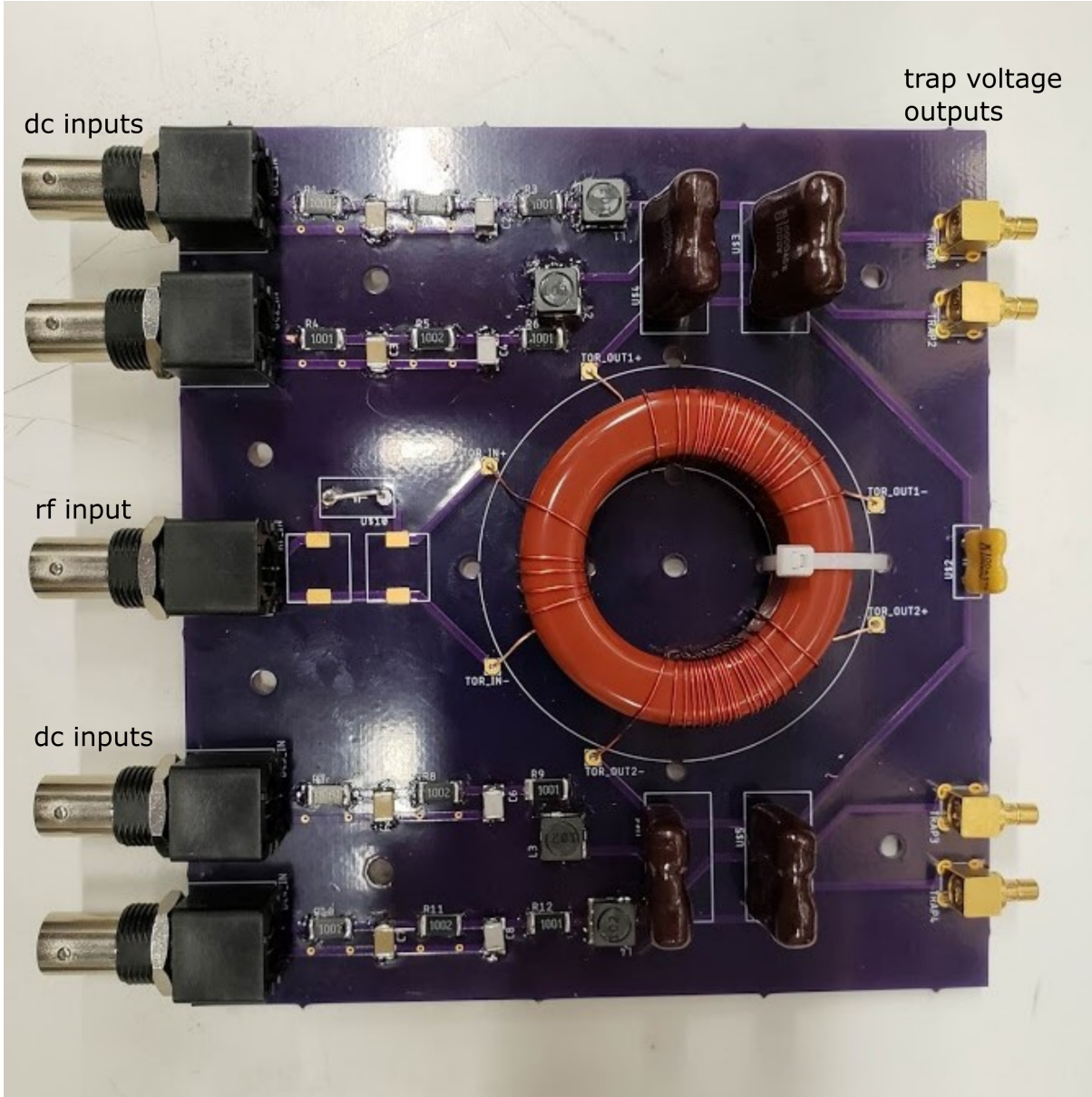
Figure 6.2: A picture of the trap electronics corresponding to Fig. 6.1.

The rf voltages on the trap electrodes can be estimated from the pickup voltages on the PCB adapter in [100]. We measured a $2\pi \times 993$ kHz resonant frequency of the resonator when it is connected to the trap, and a Q factor of $\sim 10$. The Q factor is relatively low because of the loss leaking to the DC side of the bias tee and the large

capacitance due to the coaxial cables.

The dc bias voltages on the radial electrodes is generated by a 8-channel low noise dc voltage sources included in the electronics for time-of-flight mass spectrometry [100]. The end cap voltages are supplied by a high voltage power supply [1].

## 6.3    Vacuum chamber and atom sources

The ion trap is enclosed in a CF 6" spherical octagon vacuum chamber [2]. The octagon has seven CF 2.75" side viewports available for optical access after the time-of-flight setup was removed, and a top viewport for imaging ions and for a laser for ablating the radium source. The chamber is initially pumped down by a turbomolecular pump. After a vacuum bake at 190 °C for $\sim$ 10 days, the pressure of the chamber is further pumped down by a 20 L/s ion pump [3] and a titanium sublimation pump [4] to reach a base pressure of $\sim 1 \times 10^{-10}$ mBar. The pressure is monitored with a hot filament ion gauge [5]. The chamber also has a manual precision leak valve [6] that allows introducing trace amount of chemicals to react with the trapped ions.

The strontium source for the ion trap is a homemade atomic oven shown in Fig. 6.3. It is consisted of four individual ovens formed by a stainless steel miniature tube [7], a Kapton-coated copper wire, and tantalum strip that is spot welded to make electrical connections between the stainless steel tube and the copper wire. We fill natural abundances strontium powder [8] (82% $^{88}$Sr, 7% $^{87}$Sr, 10% $^{86}$Sr, and 0.5% $^{84}$Sr) into the tube in an argon-filled glove bag, and install the loaded oven below the ion trap so that the

---

[1]ISEG SHQ 222M
[2]Kimball Physics MCF600-SphOct-F2C8
[3]Duniway Stockroom Coup. RVIP-020-ST-M
[4]Agilent 9160050
[5]Agilent UHV-24p
[6]VAT Group 59024-GE01
[7]McMaster 89935K69
[8]ESPI Metals, strontium flakes smaller than 1 mm

tip of the oven tubes are $\sim 25$ mm away from the trap center. The vacuum chamber is immediately pumped down after installing the strontium oven to prevent oxidation. To produce strontium atoms, we run a current through a stainless steel tube and a copper wire, which heats up the oven and vaporizes the strontium metal. The strontium atoms are photoionized in the ion trap via two-step photoionization at 461 nm and 405 nm [102].
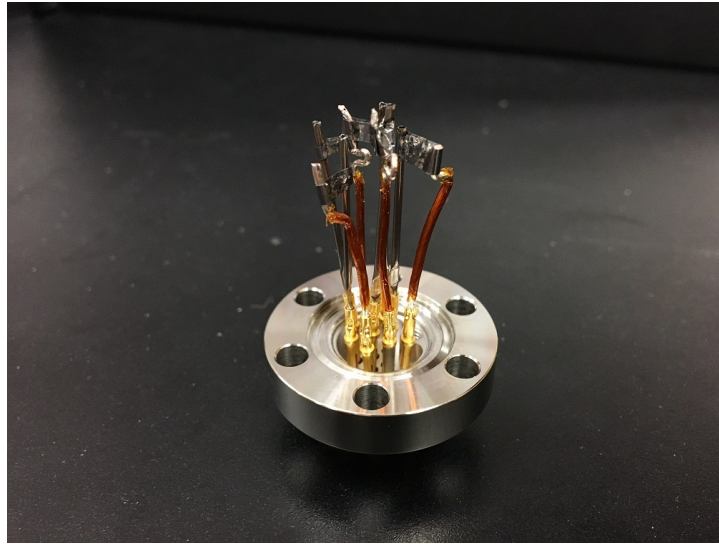
Figure 6.3: A picture of the homemade strontium ovens mounted on a CF 1.33 electrical feedthrough flange.

We also prepared a laser ablation target for radium-226. We dried 10 $\mu$Ci of $^{226}$RaCl$_2$ [9] dissolved in 5 mL of HCl (0.1 M concentration) on a stainless steel target [61], where the target is mounted on a linear motion feedthrough [10] and is placed 10 mm away from the trap center. The ablation target also holds other chemical including Ta, Ta$_2$O$_5$ and Yb for loading Ta$^+$, TaO$^+$, and Yb$^+$ in the ion trap, and the target is mounted on a motion feedthrough allowing switching the target being ablated without moving the ablation laser. A Q-switched 532 nm laser [11] is used for ablation of the target. Approximately $\sim 5$ mJ of pulse energy focused to $\sim 0.5$ mm spot size is used, which produces $^{226}$Ra$^+$

---

[9] Eckert & Ziegler
[10] MDC Precision 667001
[11] Amplitude Laser, Minilite II

ions that are trapped by turning on the trap rf voltages after $\sim 20~\mu$s of ablation to catch the ions when they enter the trap [103]. Each ablation pulse typically produces several trapped $Ra^+$ ions, and each ablation spot on the target can last tens of ablation pulses before the loading efficiency decreases. The other species of ions loaded in the trap can be removed by adjusting the rf voltages so they are no longer stable in the ion trap. After thousands of ablation pulses over $> 4$ years, we can still load $Ra^+$ from the target without noticeable efficiency decrease.

## 6.4  Fluorescence collection

We designed and built an imaging system for trapped $Sr^+$ and $Ra^+$ ions. It uses a homemade long working distance (WD $\approx 75$ mm) objective and a 750 mm focal length doublet to focus the light from the objective onto cameras and photomultiplier tubes (PMT). The collected fluorescence light passes through a long-pass dichroic beamsplitter [12] so $Sr^+$ fluorescence at 422 nm and $Ra^+$ fluorescence at 468 nm are split and sent to two sets of cameras [13] and PMTs [14]. For each set of camera and the PMT, the fluorescence light is filtered with a high-quality bandpass filter for respective wavelengths and is split with a 30:70 splitter, where 70% is sent to the PMT. An iris is installed before the PMT at the focal plane of the image to spatially filter scattered light from trap electrodes. In the rest of the section we discuss the design details of the homemade objective.

The objective design conceptually follows [104], and only uses stock spherical lenses from Thorlabs and Newport. The design requirements are listed below:

- Minimum objective working distance is 55 mm, limited by the vacuum chamber size. Optical elements *in vacuo* [105] or a re-entrant viewport [106] could reduce

---

[12]Semrock Di03-R442-t3-50x53
[13]$Sr^+$ camera: Thorlabs Quantalux CS2100M-USB; $Ra^+$ camera: Andor iXon 897 Ultra.
[14]Hamamatsu H10682-210

this number but the design would be more complicated.

- The viewport has a thickness of 5.08 mm (Corning 7056 borosilicate). The refraction due to the glass needs to be compensated in the design.

- The field of view of the objective is $\sim 1$ mm. This field of view allows seeing a large region between the radial electrodes while allowing distinguishing two ions separated by tens of micrometers. The corresponding magnification ratio of the objective and the focusing element needs to be $\sim 10$ for a typical camera sensor size of $\sim 10$ mm.

- The resolution of the imaging system should be $\sim 20$ $\mu$m or better, which is the ion spacing of a typical Coulomb crystal in this trap.

- The objective should have satisfactory performance at both 468 nm and 422 nm for imaging $Ra^+$ and $Sr^+$. However, the objective does not need to be achromatic (same effective focal length for both wavelengths). The distance between the camera and the objective can be varied for imaging at the two different wavelengths.

- The numerical aperture of the objective is inherently limited by the ion trap electrodes and the vacuum viewport size. We choose to use lenses of 2 inch diameters, which is the largest size with a good selection of stock optics and optomechanical components.

We use the CODE V program when designing this objective. Generally, we fix the design to use 4 elements including a positive meniscus lens, a plano-convex lens, a bi-convex lens, and a plano-concave lens. The focal lengths, orders, orientations, and positions of the lenses are varied to minimize the wavefront error of the image formed by parallel light transmitted through the objective and the viewport window in the reversed direction. The final design of the objective is shown in Table 6.1.

| Surface # | ROC (mm) | Thickness (mm) | Material | SA (mm) | Model |
|---|---|---|---|---|---|
| Object | Infinity | 50.038 | VACUUM | | |
| 1 | Infinity | 5.08 | 7056 | | viewport |
| 2 | Infinity | 20.224 | AIR | | |
| 3 | -119.32 | 7.29 | BK7 | 22.86 | LE1418 |
| 4 | -47.87 | 5.748 | AIR | 22.86 | |
| 5 | Infinity | 6.18 | BK7 | 22.86 | LA1979 |
| 6 | -103.01 | 27.612 | AIR | 22.86 | |
| 7 | 204.98 | 6.16 | BK7 | 22.86 | LB1199 |
| 8 | -204.98 | 2.519 | AIR | 22.86 | |
| 9 | -103.36 | 2.5 | BK7 | 22.86 | KPC070 |
| 10 | Infinity | 1.0 | AIR | 22.86 | |

Table 6.1: Custom objective design. Each line represents a surface in the objective. For example, the surface 3 is the concave surface of the Thorlabs LE1418 positive meniscus lens. "ROC" is radius of curvature, "Thickness" is the thickness of the surface along the optical axis, and "SA" is semi clear aperture of the surface. The LE1418, LA1979, and LB1199 lenses are from Thorlabs, and KPC070 is from Newport. All lenses and viewports are AR-coated for 422 nm and 468 nm.

This objective is simulated to produce a diffraction-limited image when optimized (resolution $\sim 1$ $\mu$m). The numerical aperture is approximately 0.25, and the effective focal length is $\sim 90$ mm.

The optical lenses are mounted in a Thorlabs SM2 lens tube. The spacings between the lenses are controlled by custom-machined delrin spacers [107]. We add another doublet lens of 750 mm focal length [15] after the objective to focus the image onto the camera. The objective is mounted on a 3-axis translation stage for alignment to the trap center. A composed image of co-trapped $Sr^+$ and $Ra^+$ ions is shown in Fig. 6.4.

For $Ra^+$, the measured resolution is $\sim 10$ $\mu$m. This is much larger than the simulated value because of imperfection in the imaging system assembly and tolerance in the optical lenses. The overall collection efficiency for 468 nm fluorescent photons is measured to be 0.26% [7], agreeing with the simulated numerical aperture and efficiencies of various stages of the imaging system.

---

[15]Thorlabs ACT508-750-A
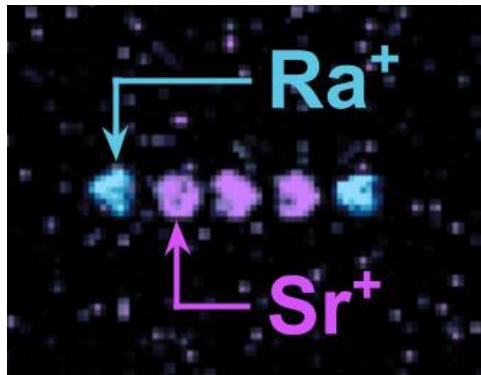
Figure 6.4: False-color fluorescence image of co-trapped radium and strontium ions. The Ra$^+$ and Sr$^+$ images are taken using two cameras, and then composed together.

# Chapter 7

# Optical systems and experiment controls

This chapter introduces the lasers relevant for controlling the ions and instruments related.

## 7.1 Lasers and cavities

### 7.1.1 Strontium

We have six lasers for strontium neutral atoms and ions. Two lasers at 461 nm and 405 nm are for photoionization of neutral strontium, and the other four lasers are for controlling $Sr^+$: Cooling laser at 422 nm, repumping laser at 1092 nm, clock laser at 674 nm, and cleanout laser at 1033 nm. The 674 nm and 1033 nm lasers are not used in work related to this thesis.

## 461 nm

The 461 nm laser is a commercial external-cavity diode laser (ECDL) with a cat-eye reflector and an interference filter from Moglabs. It drives the neutral strontium $5s^2\ {}^1S_0 \to 5s5p\ {}^1P_1$ transition which is the first step of the photoionzation process [102]. We observe enhanced photoionization for different strontium isotopes ($^{88}$Sr, $^{87}$Sr, $^{86}$Sr, and $^{84}$Sr) when the laser is tuned to the resonance frequencies of these isotopes [108].

## 405 nm

The 405 nm laser is a free-running diode laser using a Thorlabs DL5146-101S diode. It drives the neutral strontium $5s5p\ {}^1P_1 \to (5d^2 + 5p^2)\ {}^1D_2$ transition, where the $(5d^2 + 5p^2)\ {}^1D_2$ is an autoionization state above the ionization threshold. This transition has a linewidth $\sim 1$ nm [102], so the broad spectrum from a free-running diode still has enough cross section with the atom. We combine the 461 nm and 405 nm laser light into a single fiber, and send $\sim 1$ mW of 461 nm and 405 nm power each to the ion trap. The photoionization light to the ion trap is controlled by homemade shutters. The 405 nm light has another shutter just after the diode collimator to prevent blue/UV light degrading the optics when the laser is unused.

## 422 nm

The 422 nm laser is a Moglabs Littrow ECDL. It drives the Sr$^+$ $5s\ {}^2S_{1/2} \to 5p\ {}^2P_{1/2}$ transition for laser cooling. The laser is saturation absorption locked [61] to the $^{85}$Rb $5s\ {}^2S_{1/2}(F'' = 2) \to 6p\ {}^2P_{1/2}(F' = 3)$ transition which is 440 MHz red-detuned relative to the $^{88}$Sr$^+$ cooling transition frequency [38]. After locking, the 422 nm laser is 520 MHz red-detuned compared to the $^{88}$Sr$^+$ transition center [1], and we use a double-pass

---

[1]The extra 80 MHz frequency offset is due to a double-pass acousto-optical modulator at 80 MHz modulating the pump light in the saturation absorption lock setup

acousto-optical modulator (AOM) of 260 MHz center frequency to shift the light on-resonance with the transition and to control the light power. The 260 MHz AOM has a large bandwidth (single pass $\sim 100$ MHz) where the diffraction efficiency is high, allowing shifting of the laser to both sides of the transition for cooling, detection, and spectroscopy. A maximum of $\sim 500$ $\mu$W of 422 nm light is sent to the ion trap with a $k$ vector that is 45° angle with all trap motional modes for laser cooling.

**1092 nm**

The 1092 nm laser is a distributed Bragg reflector (DBR) laser from Photodigm. It drives the Sr$^+$ $4d$ $^2D_{3/2} \rightarrow 5p$ $^2P_{1/2}$ repumping transition. The laser is stabilized to a homemade laser cavity [109] via Pound-Drever-Hall (PDH) locking [110]. A double-pass AOM controls the detuning and power of the 1092 nm laser to the trap, with maximum $\sim 500$ $\mu$W power to the trap.

## 7.1.2   Radium

We have eight lasers related to Ra and Ra$^+$. A Q-switched 532 nm laser is used for laser ablation of the radium chloride target to produce the radium ions. The 483 nm and 450 nm lasers are used for photoionization of radium-224 (See Chapter 13), but they are not used for the current work related to $^{226}$Ra$^+$. The other lasers at 468 nm, 1079 nm, 728 nm, 802 nm, and 708 nm are for controlling the radium ion.

**Q-switched 532 nm laser**

A Q-switched 532 nm laser (Minilite II from Amplitude Lasers) is used for ablation of the $^{226}$RaCl$_2$ target to produce the radium ions for trapping. The laser has a pulse width of $\sim 5$ ns and is capable to send up to 25 mJ pulses at maximum 15 Hz. The laser

is sent to the ablation target via free-space optics, and focused to a $\sim 0.5$ mm spot size at the target. We use $\sim 5$ mJ of ablation laser power, which allows us to typically load one or a few ions in the trap.

**483 nm**

The 483 nm laser is a Moglabs Littrow ECDL. Similar to the 461 nm laser for Sr, this laser is used for first step of photoionization of neutral radium atoms, driving the $7s^2\,^1S_0 \to 7s7p\,^1P_1$ transition. Due to the large isotope shifts ($\sim 1$ GHz) in the heavy radium atom, the isotope shifts of this transition must be considered when loading different radium isotopes [44].

**450 nm**

The 450 nm laser is a free-running diode laser (Thorlabs PL450B). This diode does not drive any known radium transition, and it drives the radium atom from the $7s7p\,^1P_1$ state to above the ionization threshold which provides a nonzero cross section for photoionization.

**468 nm**

The 468 nm laser is a Moglabs Littrow ECDL for driving the Ra$^+$ $7s\,^2S_{1/2} \to 7p\,^2P_{1/2}$ cooling transition. It is PDH locked to a cavity, and controlled via a double-pass AOM. A maximum of $\sim 1$ mW of power is available for $^{226}$Ra$^+$. For future laser cooling work with $^{225}$Ra$^+$, we set up two additional ECDLs for driving transitions from different hyperfine levels.

## 1079 nm

The 1079 nm laser is a DBR laser from Photodigm for driving the $\mathrm{Ra}^+$ $6d\,^2D_{3/2} \rightarrow$ $7p\,^2P_{1/2}$ repumping transition. This laser is PDH locked to a cavity and controlled via a double-pass AOM. Laser power of $\sim 1$ mW is available at the ion trap. Another 1079 nm laser will be set up for laser cooling of $^{225}\mathrm{Ra}^+$.

## 728 nm

The 728 nm laser is a Moglabs Cateye ECDL for driving the $\mathrm{Ra}^+$ $7s\,^2S_{1/2} \rightarrow 6d\,^2D_{5/2}$ optical clock transition. It is PDH locked to a high-finesse cavity ($\mathcal{F} \sim 150\,000$) from Stable Laser Systems [61], resulting in a locked laser linewidth of $\sim 100$ Hz measured from $\mathrm{Ra}^+$ spectroscopy. The laser is controlled by a double-pass AOM, and the available optical power at the ion trap is $\sim 1$ mW, which is focused to a beam waist of $\sim 25$ $\mu$m.

## 802 nm

The 802 nm laser is a homemade Littrow ECDL using an Eagleyard EYP-RWE-0810-03010-1300-SOT02-0000 diode based on a design modified from [111]. This laser drives the $\mathrm{Ra}^+$ $6d\,^2D_{5/2} \rightarrow 7p\,^2P_{3/2}$ cleanout transition, and it is locked to a HighFinesse WS8 wavemeter via a software feedback loop running on a computer.

## 708 nm

The 708 nm laser is another homemade ECDL based on the same design as the 802 nm laser for driving the $\mathrm{Ra}^+$ $6d\,^2D_{3/2} \rightarrow 7p\,^2P_{3/2}$ transition. This laser is only used in the $P_{3/2}$ branching fraction measurement in Sections 9.2.1. It uses a Thorlabs HL7001MG diode which requires heating the laser to $\sim 60$°C to pull the transition to the target frequency. It is also locked to the WS8 wavemeter.

### 7.1.3   Molecular ions

All molecular ions we currently plan to work with, including $RaH^+$, $RaSH^+$, and $RaOCH_3^3$, are closed-shell molecules and they are not compatible with laser cooling and optical pumping to a single state. We plan to control the internal states of the molecular ions using stimulated Raman transitions. Therefore, we set up a 1064 nm fiber laser from Azurlight that can output 20 W continuous wave power. Two double-pass AOM setups are used for controlling the detuning and power of the Raman beams. This laser is not used in the work reported in the thesis.

## 7.2   Absolute frequency measurement equipment

Most of the transitions that we use do not have a convenient alkali-atom transition nearby that allows us to stabilize the laser to. Many lasers are locked to cavities with a 1.5 GHz free spectra range, so we need to measure the absolute frequencies of the lasers better than $\sim 750$ MHz to confirm that the longitudinal mode in the cavity is correct. In addition, to determine the absolute transition frequency measurements of $Ra^+$ we also need optical frequency references. In this section we discuss the wavemeters and the molecular vapor cells which are the current apparatuses we use for absolute frequency measurements.

### 7.2.1   Wavemeters

We use a HighFinesse WS8 wavemeter with an 8-channel photon crystal fiber switch to determine the absolute transition of the lasers in the daily experiments. This wavemeter allows us to monitor the frequencies of up to 8 lasers simultaneously and make sure that the modes of the lasers are correct (i.e. operating in a stable single-frequency

mode). Without calibration, we measured that the wavemeter measurement error from the absolute frequency is $\sim 500$ MHz with the exact error sign and magnitude wavelength dependent. The day-to-day shift of the wavemeter is typically a few MHz. We also set up a Moglabs Fizeau wavemeter with a 8-channel switch for monitoring more lasers. The absolute error of the Moglabs wavemeter is $\sim 1$ GHz with day-to-day shift of $\sim 10$ MHz.

### 7.2.2   Molecular vapor cells

Iodine and tellurium transition lines are typically used for dense frequency reference lines in the visible to near infrared range. We use an $^{127}I_2$ cell and a $^{130}Te_2$ cell for determining the absolute frequencies within $\sim 500$ MHz in these wavelength ranges. The altas for these lines [112, 113, 114, 115] typically have a reported precision of tens of MHz. The software Iodine Spec 5 [116, 117] can generate the calculated spectrum of iodine via software, which we found to be more precise and easier to compare with our measured data than the iodine altas.

## 7.3   Experiment control

### 7.3.1   Pulser

We initially used the pulser [118] for controlling this setup. The pulser is an FPGA-based system that is capable of producing pre-programmed transistor-transistor logic (TTL) and direct digital synthesis (DDS) rf pulse sequences. The pulser supports up to 16 DDS outputs, and $\sim 40$ TTL channels. It can also count the pulses output from a PMT. The interface to control the pulse sequences is written in python and is compatible with the experiment control framework LabRAD [119] that we have used. All AOMs that control lasers sent to the ion trap are driven using the DDSes in the pulser, and the clock

signal for all DDSes are generated by a rubidium microwave clock (Stanford Research Systems CG635). For operating an ion optical clock, we also implemented a pulser feature that allows more flexible triggering of the pulse sequence with the ac power line to reduce the magnetic field fluctuations in the experiment.

## 7.3.2   Sinara devices and ARTIQ

We started to hit limits in the pulser's capabilities with more complex experiments such as clocks and preparing for quantum logic spectroscopy. For example, the pulser has a maximum limit ($\sim$ 1000) on the number of pulses it can generate in a pulse sequence, which poses a limit on the state preparation and sideband cooling sequences for an experiment. Also, the pulser does not support realtime logic to modify pulse sequences based on inputs such as PMT counts. Such real time capabilities would help us in a quantum logic spectroscopy experiment. These features are supported by Sinara hardware and the accompanying ARTIQ software [120]. We have set up Sinara systems for all ion trapping experiments in our lab.

# Chapter 8

# Laser Cooling of Radium Ions

The contents of this chapter include our paper *Laser Cooling of Radium Ions* [7].

The unstable radium nucleus is appealing for probing new physics due to its high mass, octupole deformation and energy level structure. Ion traps, with long hold times and low particle numbers, are excellent for work with radioactive species, such as radium and radium-based molecular ions, where low activity, and hence low total numbers, is desirable. We address the challenges associated with the lack of stable isotopes in a tabletop experiment with a low-activity ($\sim 10 \ \mu$Ci) source where we laser-cool trapped radium ions. With a laser-cooled radium ion we measured the $7p \ ^2P^o_{1/2}$ state's branching fractions to the ground state, $7s \ ^2S_{1/2}$, and a metastable excited state, $6d \ ^2D_{3/2}$, to be $p = 0.9104(7)$ and $0.0896(7)$, respectively [7]. With a nearby tellurium reference line we measured the $7s \ ^2S_{1/2} \rightarrow 7p \ ^2P^o_{1/2}$ transition frequency, $640.096\,63(6)$ THz [7].

Radium, the heaviest alkaline earth element, has no stable isotopes. Singly ionized radium's simple electronic structure is amenable to optical pumping and laser cooling with wavelengths far from the challenging UV of most alkaline earth type ions. Radium's heavy nucleus, atomic number $Z = 88$, is well suited to searches for new physics, where sensitivity to symmetry breaking forces scales as $\propto Z^3$ [121, 64]. Certain radium isotopes,

such as radium-225, have additional nuclear structure enhancements to $CP$ (charge-parity) violating new physics [57, 6]. Setting limits to sources of $CP$ violation will help us understand the baryon asymmetry in the observed Universe [122].

Pioneering work with trapped HfF$^+$ molecular ions has made significant progress in constraining leptonic $CP$ violation, and has rigorously studied potential systematic effects for future experiments [71]. A complementary hadronic $CP$ violation experiment with radioactive molecular ions RaOH$^+$ or RaCOH$_3^+$ [86] is an intriguing possibility, where the low densities and long hold times of ion traps are well matched to working with radioactive isotopes, because low total activity is desirable. The radium-225 nucleus ($I = 1/2$) has octupole deformed parity doublets that enhance sensitivity to $CP$ violating forces by a factor of 100-1000 compared to the current touchstone atomic system, $^{199}$Hg [123, 4, 52]. A radium-based molecular ion, such as $^{225}$RaOH$^+$, has an additional sensitivity advantage because of the molecule's closely spaced, opposite parity electronic states in addition to the enhancements from the closely spaced, opposite parity radium nuclear states. Trapped and laser-cooled radium ions could be the starting point for generating such radium-based molecular ions, where optical pumping Ra$^+$ may provide control of chemical reactions to produce RaOH$^+$, as seen in other alkaline earth ions Ca$^+$ and Be$^+$ [124, 125].

For quantum simulation with trapped ions, qubit states protected from environmental noise with long lifetimes are favorable. A spin-1/2 nucleus with a single electron atom, such as in $^{171}$Yb$^+$, $^{133}$Ba$^+$ [103], or $^{225}$Ra$^+$, provides such levels that are first-order insensitive to magnetic fields. The qubit state is typically read out through optical cycling, with readout fidelity limited by the $P_{1/2}$ state's hyperfine splitting (2.1 GHz in $^{171}$Yb$^+$). Though a massive nucleus is at odds with high secular frequencies, it is desirable for its large hyperfine interactions, as off-resonant pumping during qubit readout decreases quadratically with hyperfine splitting. The $P_{1/2}$ hyperfine splitting of $^{225}$Ra$^+$ is 5.4 GHz [44], which suppresses the qubit readout error by a factor of $\sim 8$ compared

to $^{171}$Yb$^+$ [126]. Radium also has favorable transitions where abundant optical power and photonic technology are available, see Fig. 8.1 (b). The radium ion supports optical qubits on the $S_{1/2} \to D_{5/2}$ transition. The $D_{5/2}$ state of $^{225}$Ra$^+$, like the ground state, has 2 hyperfine "clock" states, which, when combined with the ground state qubit levels, offers the possibility to simulate spin-1 or spin-3/2 physics with four magnetic field insensitive states [127].
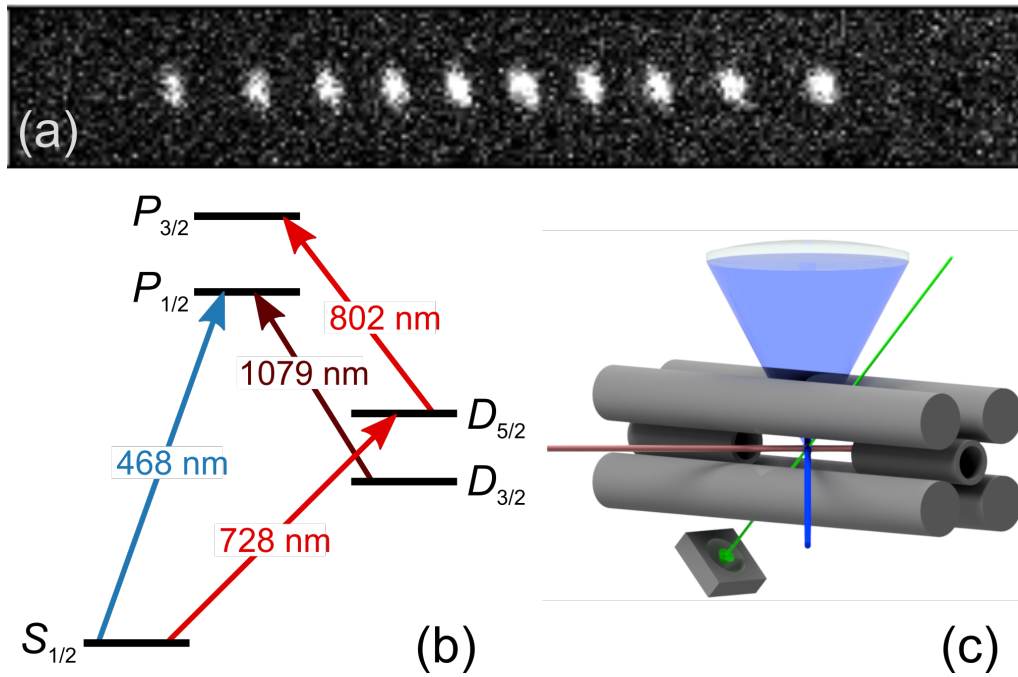


Figure 8.1: A Coulomb crystal of 10 trapped radium-226 ions (a) that were loaded into the trap via laser ablation and laser cooled with a combination of 468 nm and 1079 nm radiation. The relevant level structure of Ra$^+$ for the laser cooling and measurements done in this work [7] are shown in (b), in addition to the transitions necessary for controlling the ion via the narrow $^2S_{1/2} \to {}^2D_{5/2}$ quadrupole transition at 728 nm and the $^2D_{5/2} \to {}^2P^o_{3/2}$ dipole transition at 802 nm. In (c) the ion trap is depicted with the radium ablation target and the ablation laser (green), the 468 nm cooling light (blue), and the 1079 nm repump light (red). The diagonal rf electrodes are separated by 6 mm and the end cap electrodes by 15 mm. The rf trapping frequency is 2.1 MHz.

In this work we trap and laser cool $^{226}$Ra$^+$ ($I = 0$) to form Coulomb crystals, as seen in Fig. 8.1 (a). We used the crystallized radium ions to measure the $7p\ ^2P^o_{1/2}$

state's branching fractions to the $7s\ ^2S_{1/2}$ and $6d\ ^2D_{3/2}$ states, a necessary measurement to determine dipole matrix elements for the respective transitions. Our measurement at 2 digits of precision is sufficient to support optical pumping or basic simulations with optical Bloch equations, but we extended the measurement to higher precision to support PNC measurements in Ra$^+$ at the 0.8% level [128, 129]. We also measure the $7s\ ^2S_{1/2} \rightarrow 7p\ ^2P^o_{1/2}$ transition frequency with respect to a Te$_2$ molecular absorption line, which establishes a convenient frequency reference for the radium-226 ion's most important transition [115].

In previous work at a nuclear facility singly ionized radium isotopes 209 through 214 were produced and trapped [130, 50]. We apply a different technique to trap radium-226. The radium is ionized and loaded into the trap by ablation with a 532 nm $\sim 10$ mJ pulse from a Nd:YAG laser with 0.5(1) mm $1/e$ intensity diameter. The ion trap's rf trapping voltage is switched on 20 $\mu$s after the ablation pulse to enhance radium ion loading efficiency [100]. The radium was received as $^{226}$RaCl$_2$ in 5 mL 0.1 M HCl solution with an activity of 10(2) $\mu$Ci, which corresponds to $\sim 3 \times 10^{16}$ radium-226 atoms. We made a laser ablation target by drying the radium solution on a 316 stainless steel mount which was installed in the vacuum system on a translation stage to position the target $\sim 15$ mm from the trap center, see Fig. 8.1 (c).

The radium ion fluoresces when near resonant light addresses the $S_{1/2} \rightarrow P_{1/2}$ transition at 468 nm and the $D_{3/2} \rightarrow P_{1/2}$ transition at 1079 nm, see Fig. 8.1 (b). The ion is laser cooled when the 468 nm laser is red detuned from the $S_{1/2} \rightarrow P_{1/2}$ transition. Electronic branching from the $P_{1/2}$ state populates the $D_{3/2}$ state, which the 1079 nm light repumps back into the fluorescence cycle. To prevent coherent dark states a magnetic field of a few gauss is applied [93].

The signals for our measurements are the 468 nm photons spontaneously emitted by radium ions. These photons are focused onto a photomultipler tube (PMT), Hama-

matsu H10682-210, whose output is sent to an integrated direct digital synthesizer and field-programmable gate array control and measurement system that can convert the PMT pulses to time-tagged photons [118]. The same system synchronously controls the measurement sequences by driving acousto-optic modulators (AOMs) which set the amplitude and frequency offsets for the 468 and 1079 nm lasers. The AOM extinction ratios are $\geq$ 60 dB. Measurement sequences, based on the techniques developed by Ramm *et al.* [131] and Pruttivarasin *et al.* [25], eliminate challenging systematics, such as AC Stark shifts, by addressing only one transition at a time.
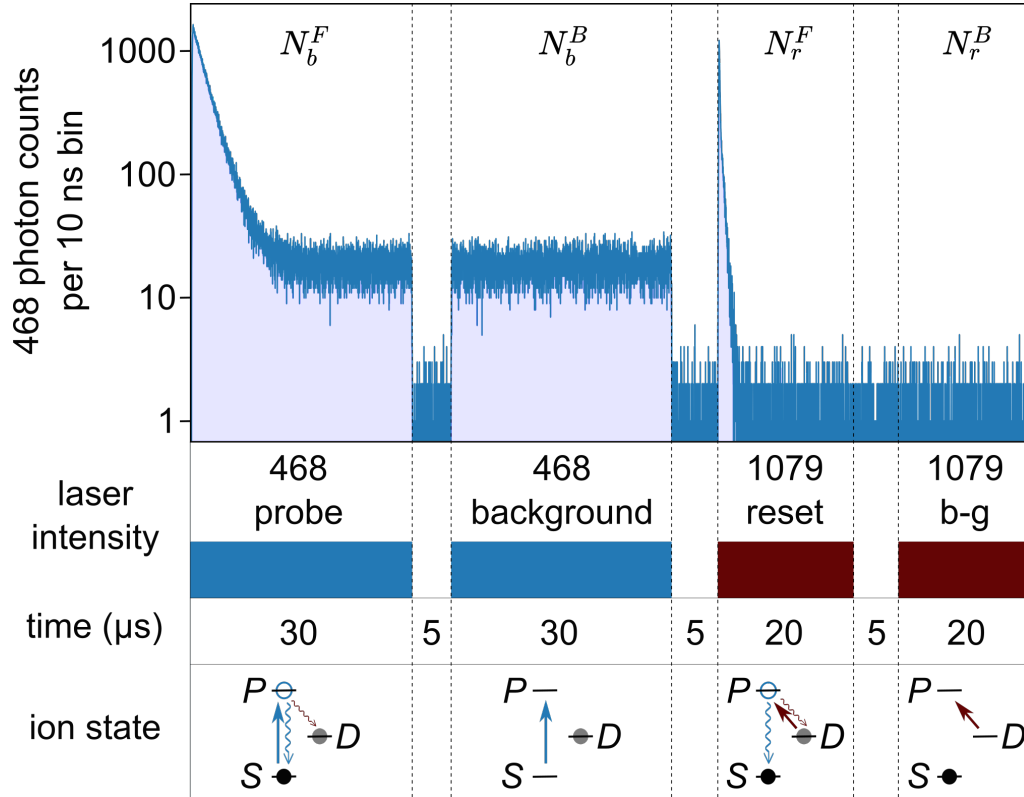


Figure 8.2: The total PMT counts during the $P_{1/2}$ branching fraction measurement are shown, along with the corresponding laser pulses and the measurement timing sequence. The bottom panel shows the electronic population, applied optical fields, and expected decays.

The branching fraction measurement sequence is summarized in Fig. 8.2. Before each measurement, we Doppler cool the radium ion for 100 $\mu s$ and then optically pump

population into the $S_{1/2}$ state by applying 1079 nm light for 20 $\mu s$. After cooling and state preparation the electronic population is optically pumped to the $D_{3/2}$ state and collected 468 nm photons are time tagged, $N_b^F$. The background scattered 468 nm light is then measured, $N_b^B$, while the ion is shelved in the $D_{3/2}$ state. The population is then pumped back to the $S_{1/2}$ ground state with 1079 nm light, and if the single emitted 468 nm photon is collected it is time tagged, $N_r^F$, and a corresponding background, $N_r^B$, is recorded. We subtract the respective backgrounds to determine the number of collected photons emitted by the radium ion, $N_b$ and $N_r$. From these counts we calculate the branching fraction to the ground state, $p = [N_b/(N_b + N_r)]$ [131]. The measurement is repeated $11.5 \times 10^6$ times in approximately one hour with a single radium ion. The raw photon counting results are $N_b^F = 359\,583$, $N_b^B = 55\,297$, $N_r^F = 31\,386$, and $N_r^B = 1443$, which yields a statistical branching fraction of $p = 0.9104(5)$. The $N_r$ counts are also used to measure the imaging system detection efficiency (0.26%).

The largest systematic uncertainty in the branching fraction measurement comes from residual birefringence of the imaging system and the Hanle effect. If the 468 and 1079 nm lasers are perfectly linearly polarized, the Hanle effect is not present, and an equal number of right- and left-handed circularly polarized photons will be collected [132]. However, if either laser beam has a circularly polarized component, then there will be an imbalance in the right- and left-handed circularly polarized photons collected. The imbalance will depend on the direction and magnitude of the applied magnetic field which sets the quantization axis. Residual birefringence of the imaging system may result in different detection efficiencies for the two circular polarizations, which in turn will shift the branching fraction measurement. The applied magnetic field is parallel to the 1079 nm laser, and both 1079 and 468 nm lasers are linearly polarized to suppress the Hanle effect. We set a limit on the uncertainty due to residual birefringence and the Hanle effect by reversing the applied magnetic field. The field reversal will flip the

imbalance between right- and left-handed circularly polarized photons collected [133], giving a different value for the branching fraction [131, 134]. The measured branching fraction with the field reversed, $p = 0.9107(5)$, agrees with the original field configuration. Therefore, uncertainty due to the combined effects of residual birefringence and the Hanle effect is at the level of the statistical uncertainty.

The systematic uncertainties and shifts due to other sources we considered are significantly less than those due to residual birefringence. For shifts due to collisions we considered worst case scenarios. For example, after shelving to the $D_{3/2}$ state, a collision could put the ion in an orbit that is dark to the 1079 nm pump pulse, and then a second collision could return the ion to the trap center where it emits a 468 nm photon during the 1079 nm background pulse. From our measurements we estimate the average collision rate to be less than 0.32 collision per second. PMT dead time (20 ns) results in both systematic error and shift. We evaluate systematic shifts due to the finite lifetime of the $D_{3/2}$ state, the finite measurement time, and the finite extinction ratio of the AOMs using optical Bloch equations that describe the three-level system [131]. To solve the Bloch equations we use Rabi frequencies determined from fitting the spontaneous decays in $N_b^F$ and $N_r^F$, a theoretical $D_{3/2}$ state lifetime of 638(10) ms [56], and the $P_{1/2}$ branching fraction, $p = 0.9104$, from our statistical results. More details are included in the Supplemental Material [134].

The uncertainties and shifts for the branching fraction measurement are summarized in Table 8.1. When we add the uncertainties in quadrature the branching fraction to the ground state is $p = 0.9104(7)$, where systematic shifts do not contribute as their sum is far below the measurement uncertainty. The measurement verifies theoretical techniques applied to this multielectron system that previously gave the only knowledge of the branching fraction [56, 135, 136], see Fig. 8.3. The measurement can also be expressed as a ratio of the reduced dipole matrix elements between the $S_{1/2} \to P_{1/2}$ and

Table 8.1: Uncertainties and shifts for the $P_{1/2}$ branching measurement.

| Source | Shift | Uncertainty |
|---|---|---|
| Statistical | ... | $5 \times 10^{-4}$ |
| Birefringence | ... | $5 \times 10^{-4}$ |
| Collisions | ... | $< 4 \times 10^{-5}$ |
| PMT dead time | $3 \times 10^{-6}$ | $3 \times 10^{-6}$ |
| $D_{3/2}$ state lifetime | $2 \times 10^{-7}$ | $2 \times 10^{-8}$ |
| Measurement time | $5 \times 10^{-9}$ | $3 \times 10^{-7}$ |
| AOM extinction ratio | ... | $5 \times 10^{-7}$ |
| **Total** | $3 \times 10^{-6}$ | $7 \times 10^{-4}$ |

$D_{3/2} \to P_{1/2}$ transitions, $m_{SP}/m_{PD} = 0.912(4)$.

The $S_{1/2} \to P_{1/2}$ transition of Ra$^+$ is crucial to laser cooling and state detection. We measure this transition's linewidth and center frequency with a linescan measurement [25]. From the linewidth we infer a lower limit on the $P_{1/2}$ state's lifetime of 7.3(1) ns, consistent with the theoretical value of 8.57(10) ns [135]. With tellurium vapor cell spectroscopy we determine the $^{226}$Ra$^+$ $7s$ $^2S_{1/2} \to 7p$ $^2P^o_{1/2}$ transition frequency to be 640.096 63(6) THz. Our measurement agrees with a transition frequency of 640.096 647(23) THz, which was inferred from a measurement of this transition in $^{214}$Ra$^+$ anchored to tellurium line 178 [50], and separate Ra$^+$ isotope shift measurements at the CERN ISOLDE facility [44].

For the Ra$^+$ linescan we trap and laser cool a chain of four radium ions. In the measurement sequence the ions are excited by a 468 nm laser probe pulse (2 $\mu$s), and then reset back to the ground state by a 1079 nm pulse (10 $\mu$s). The pulse sequence is repeated for different detunings, and before every ten sequences the ions are Doppler cooled for 500 $\mu$s and optically pumped to the electronic ground state. We run the pulse sequence $2 \times 10^5$ times at each of 56 detunings set by an AOM with randomized measurement ordering. The 468 nm laser is Pound-Drever-Hall locked to a Corning Ultra-Low Expansion (ULE) glass cavity sealed in a vacuum chamber with multiple layers of
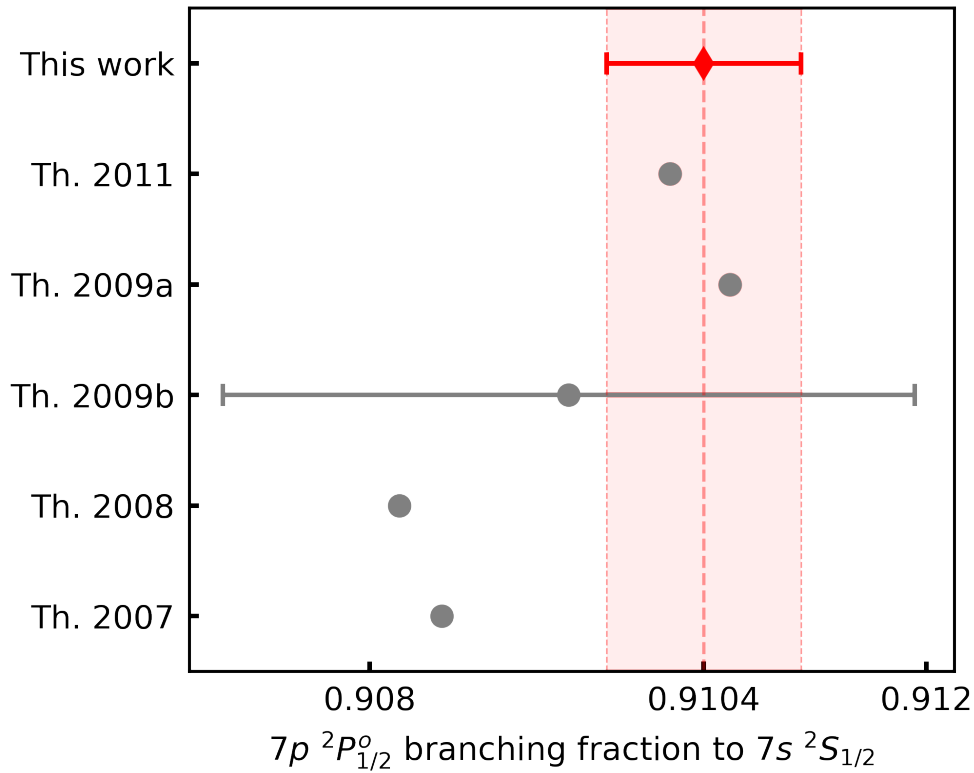
Figure 8.3: The measured branching fraction of the $^{226}$Ra$^+$ $P_{1/2}$ to the $S_{1/2}$ (diamond), $p = 0.9104(7)$, compared to previous theoretical values (circles) where error bars are included when uncertainty is available. The theoretical branching ratios are determined from reduced dipole matrix elements in the corresponding references: Th. 2011 [136], Th. 2009a [56], Th. 2009b [135], Th. 2008 [137], Th. 2007 [138] .

acoustic, seismic, and thermal isolation with active temperature stabilization [109]. In order to determine the transition frequency by a comparison with tellurium spectroscopy, the stabilized laser frequency during the measurement is recorded with a wave meter. The photon counts for the measurement are plotted in Fig 8.4.

The nearest measured $^{130}$Te$_2$ line to the radium transition is line 176 at $640.098\,99(5)$ THz [115]. We measure the line in a 10 cm long tellurium vapor cell at 550°C by scanning a laser while recording the absorption on a photodetector and the frequency with a wave meter (High Finesse WS-8), see Fig. 8.4 (b). The line center is determined with a Gaussian fit and is then compared to the recorded frequency of the radium linescan to de-

termine its detuning, -2.36 GHz. The largest uncertainty in the frequency measurement is the 50 MHz uncertainty in the Te$_2$ line [115]. There is a 10 MHz uncertainty contribution due to the wavemeter, which is determined with multiple linescans of the radium ion's $S_{1/2} \rightarrow P_{1/2}$ transition, and an additional 10 MHz uncertainty in the measured Te$_2$ transition's center frequency.

We fit the photon counts of the Ra$^+$ linescan to a Lorentzian and get a linewidth of 21.7(4) MHz, see Fig. 8.4 (a). The largest broadening contribution is likely micromotion Doppler broadening [11], which we estimate broadens the line by $\sim 2.1$ MHz [134].
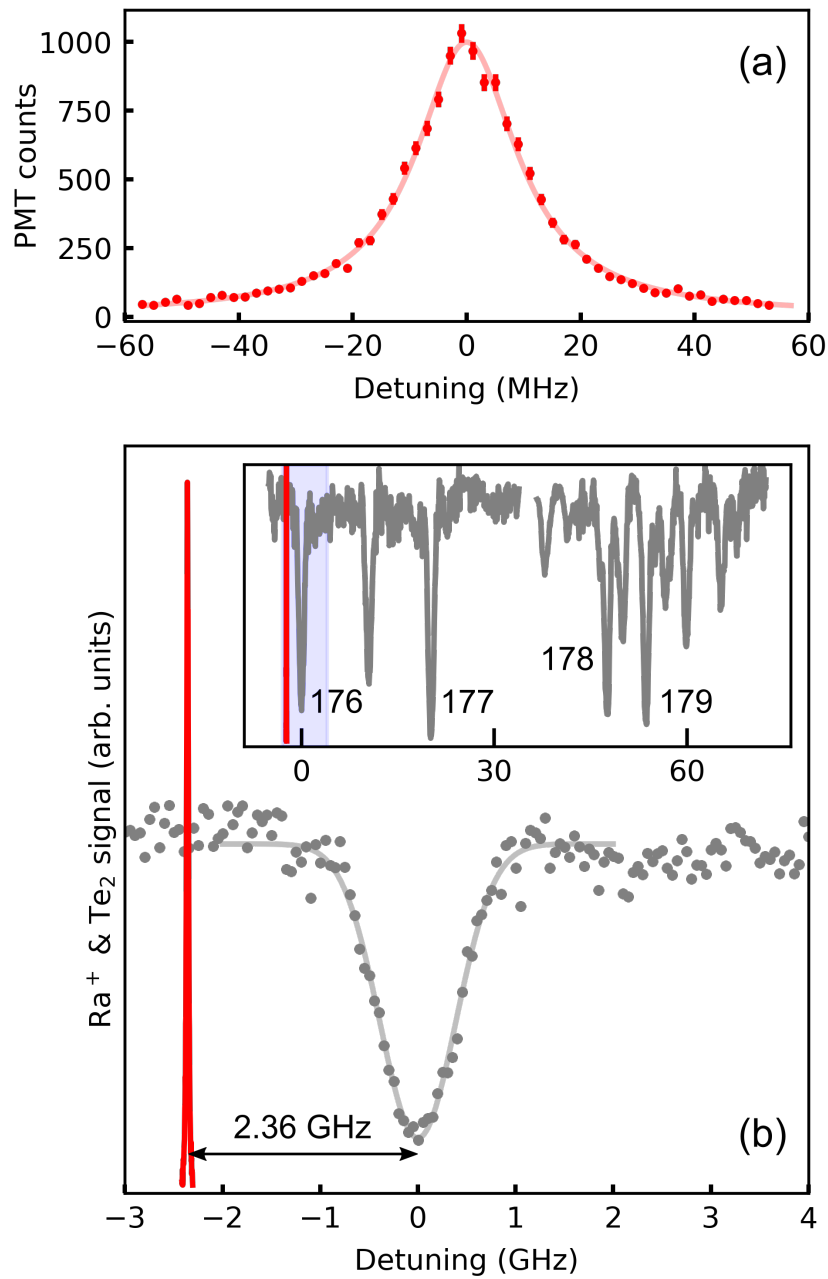
Figure 8.4: Collected photons from the Ra$^+$ linescan measurement with a Lorentzian fit (a). The tellurium absorption spectrum is plotted with the Ra$^+$ linescan (b), where the tellurium data (grey) and Ra$^+$ data (red) are scaled and offset to highlight the detuning between the transitions. The inset of (b) shows tellurium lines in the vicinity of the Ra$^+$ transition labelled with their atlas numbers, and the frequency span of the outset region highlighted in blue.

In this work we laser cooled trapped $Ra^+$, an element where the most stable isotope, radium-226, has a 1600 year half-life, in a tabletop experiment ($< 4$ L vacuum volume). Laser cooling the trapped radium ions helped keep the ions well localized in the trap for $> 12$ h at a time, enabling a precision measurement of the $P_{1/2}$ state's branching fraction.

This work opens the door to research with laser-cooled radium ions, including isotopes such as radium-225. The low charge-to-mass ratio of $Ra^+$ is well suited to sympathetic cooling of heavy atoms and large molecular ions. Cold $Ra^+$ could be used to make molecular ions such as $RaOH^+$, and to sympathetically cool their motion and control their internal states with quantum logic spectroscopy [16].

# Chapter 9

# Measurement of low-lying states of $^{226}$Ra$^+$

The trapping and laser cooling of radium ions allow us to measure fundamental properties of the low-lying electronic structure of the radium ion. This chapter summarizes the published measurement results and the plans for unfinished measurements.

## 9.1    Frequency measurements

The low-lying electronic structure of Ra$^+$ is shown in Fig. 3.1 (b). The only direct measurement of $^{226}$Ra$^+$ transition frequencies dates back to 1933 [40] with several GHz uncertainties. Several transition frequencies of short-lived radium isotopes from $^{209}$Ra$^+$ to $^{214}$Ra$^+$ have been measured in an ion trap with buffer gas cooling [46, 47, 48, 49, 50], and thus some of the transition frequencies of $^{226}$Ra$^+$ can be determined indirectly from isotope shift measurements [44, 45].

We have measured all low-lying transition frequencies of $^{226}$Ra$^+$ to tens of MHz uncertainties. These measurements have enough precision to support future radium ion trap-

ping and cooling experiments. The measurement results are summarized in Table 9.1, with more details discussed in [61].

Table 9.1: Experimentally measured $^{226}$Ra$^+$ transition frequencies.

| Transition | Frequency (GHz) |
|---|---|
| $7s\ ^2S_{1/2} \to 7p\ ^2P_{3/2}$ (382 nm) | 785 722.11(3) [139] |
| $7s\ ^2S_{1/2} \to 7p\ ^2P_{1/2}$ (468 nm) | 640 096.63(6) [7] |
| $6d\ ^2D_{3/2} \to 7p\ ^2P_{3/2}$ (708 nm) | 423 444.39(3) [140] |
| $7s\ ^2S_{1/2} \to 6d\ ^2D_{5/2}$ (728 nm) | 412 007.701(18) [140] |
| $6d\ ^2D_{5/2} \to 7p\ ^2P_{3/2}$ (802 nm) | 373 714.40(2) [140] |
| $7s\ ^2S_{1/2} \to 6d\ ^2D_{3/2}$ (828 nm) | 362 277.68(5) [140] |
| $6d\ ^2D_{3/2} \to 7p\ ^2P_{1/2}$ (1079 nm) | 277 818.95(8) [140] |

## 9.2 Measurements of branching fractions and lifetimes

The branching fractions and lifetimes of the low-lying states are measured too. These measurements are important to determine the transition matrix elements, which are important for understanding the radium ion and for determining key systematic effects of a radium ion optical clock [8]. In addition, high-precision measurements of radium ions can serve as benchmark for theoretical calculations of heavy radioactive atoms. Previously, only an lower bound of the $D_{5/2}$ state lifetime is measured [46]. Our measurements are summarized in Table 9.2, with measurement details reported in this section. The $P_{1/2}$ state branching fraction measurement is described in Chapter 8.

### 9.2.1   $P_{3/2}$ state branching fractions

The $P_{3/2}$ state decays to three states, $S_{1/2}$, $D_{3/2}$, and $D_{5/2}$. We prepare the ion in the $D_{3/2}$ state or the $D_{5/2}$ state, and use the $D_{3/2} \to P_{3/2}$ or the $D_{5/2} \to P_{3/2}$ transition

Table 9.2: $^{226}$Ra$^+$ lifetime and branching fraction measurements. * Denotes preliminary measurements

| Ra$^+$ State | Lifetime | Branching Fraction |
|---|---|---|
| $7p\ ^2P_{1/2}$ | $\geq 7.3(1)$ ns [7] | 0.9104(7), 0.0896(7) [7] |
| $7p\ ^2P_{3/2}$ | 4.78(3) ns [141] | 0.87678(20), 0.10759(10), 0.01563(21) [142] |
| $6d\ ^2D_{3/2}$ | 303.4(9)* ms | N/A |
| $6d\ ^2D_{5/2}$ | 623(15)* ms | N/A |

to optically pump the ion to the other two states, and finally measure the population in the two states. We report the experimentally-measured $P_{3/2}$ branching fractions to the $7s\ ^2S_{1/2}$ ground state 0.876 78(20), the $6d\ ^2D_{5/2}$ state 0.107 59(10), and the $6d\ ^2D_{3/2}$ state 0.015 63(21). We also collaborated with theorists to benchmark our experimental values with improved theoretical calculations. Further details are provided in [142].

## 9.2.2 $P_{3/2}$ state lifetime

We also measured the lifetime of the $P_{3/2}$ state by measuring the ac Stark shift and scattering rate on the $D_{5/2} \to P_{3/2}$ transition from an off-resonant light that is $\sim$ GHz detuned, and we report a 4.78(3) ns lifetime from a ratio of the ac Stark shift and the scattering rate. For more details see [141].

## 9.2.3 $P_{1/2}$ state lifetime

The lifetime of the $P_{1/2}$ state is important for estimating systematic effects of the Ra$^+$ ion optical clock [8] such as the Stark shift due to the black-body radiation [143]. It can be measured with a similar technique as the $P_{3/2}$ lifetime measurement described above, as demonstrated with the Ca$^+$ $4p\ P_{1/2}$ state in [144]: We can measure the scattering rate and ac Stark shift from 468 nm light off-resonantly driving the $S_{1/2} \to P_{1/2}$ transition. The ac Stark shift can be measured from the energy shift on the $S_{1/2} \to D_{5/2}$ clock transition. The scattering rate requires measuring the rate that population moves between the two

Zeeman levels of the ground state, which relies on high-fidelity state preparation and detection of the $S_{1/2}$ Zeeman sublevels and precise polarization and $k$ vector control of the off-resonant laser. These requirements are difficult to realize in our current ion trap, which is not optimized for high-fidelity coherent control. However, they may be achievable in the new ion trap we are testing (See Appendix A).

Another method to measure the lifetime of the $P_{1/2}$ state is from a ratio of the dipole matrix elements $\langle S_{1/2}|D|P_{1/2}\rangle$ and $\langle S_{1/2}|D|P_{3/2}\rangle$. This ratio can be measured from the magic wavelength of the $S_{1/2} \to D_{5/2}$ transition that is between the $S_{1/2} \to P_{1/2}$ and the $S_{1/2} \to P_{3/2}$ transition wavelengths, where the ac Stark shifts from the two transitions on the $S_{1/2}$ state cancel. This magic wavelength is calculated to be around $\sim 435$ nm for Ra$^+$ [145]. A similar measurement has been done for Ca$^+$ [146]. In the following paragraphs we discuss the requirements and expected precision from this measurement.

The $\langle S_{1/2}|D|P_{3/2}\rangle$ dipole matrix element is measured to be $4.484(13)$ $ea_0$ [141], having a fractional uncertainty of 0.3%. To determine the $\langle S_{1/2}|D|P_{1/2}\rangle$ matrix element to a similar precision, we need to measure a matrix element ratio that is $\lesssim 0.3\%$. For simplicity, we assume that the ac Stark shift on the $S_{1/2} \to D_{5/2}$ transition is only due to the $S_{1/2} \to P_{1/2}$ (D1) and the $S_{1/2} \to P_{3/2}$ (D2) transitions. The ac Stark shift contributions from other transitions is small near 435 nm due to the very large laser detuning, and these contributions can be theoretically calculated to a sufficient precision [147].

The ac Stark shift due to off-resonant light driving a transition is

$$\delta_{\text{S,single transition}} = \frac{\Omega^2}{4\Delta},\tag{9.1}$$

where $\Delta$ is the light detuning, and $\Omega$ is the Rabi frequency of the light

$$\Omega = \frac{eE_0\mu}{\hbar},$$ (9.2)

where $e$ is the elementary charge, $E_0$ is the electric field amplitude of the light, and $\mu$ is the reduced dipole matrix element of the transition.

The total ac Stark shift on the $S_{1/2}$ state due to the D1 and D2 transitions is

$$\delta_{\mathrm{S}} = \frac{e^2 E_0^2}{4\hbar^2}\left(\frac{\mu_{\mathrm{D1}}^2}{\Delta_{\mathrm{D1}}} + \frac{\mu_{\mathrm{D2}}^2}{\Delta_{\mathrm{D2}}}\right).$$ (9.3)

At the magic wavelength $\lambda_{\mathrm{magic}}$ ($\omega_{\mathrm{magic}} = 2\pi c/\lambda_{\mathrm{magic}}$), the ac Stark shift is zero so

$$\frac{\mu_{\mathrm{D1}}^2}{\Delta_{\mathrm{D1}}} = -\frac{\mu_{\mathrm{D2}}^2}{\Delta_{\mathrm{D2}}}.$$ (9.4)

After plugging $\omega_{\mathrm{magic}}$ in,

$$\mu_{\mathrm{D1}} = \mu_{\mathrm{D2}}\sqrt{\frac{\omega_{\mathrm{magic}} - \omega_{\mathrm{D1}}}{\omega_{\mathrm{D2}} - \omega_{\mathrm{magic}}}},$$ (9.5)

where $\omega_{\mathrm{D1}}$ ($\omega_{\mathrm{D2}}$) is the D1 (D2) transition frequency in radians.

After plugging the transition frequencies in, the expected uncertainty of $\mu_{\mathrm{D1}}$ from the uncertainty of $\omega_{\mathrm{magic}}$ is

$$\delta\mu_{\mathrm{D1}} = \frac{\delta\omega_{\mathrm{magic}}}{2\pi \times 1.1 \times 10^{-14}\,\mathrm{Hz}}\mu_{\mathrm{D2}},$$ (9.6)

so $\delta\omega_{\mathrm{magic}}/2\pi \gtrsim 300$ GHz is required to limit the fractional uncertainty due to the magic wavelength measurement to $\lesssim 0.3\%$.

From [147], we can determine that the slope of the dynamic dipole polarizability of the $S_{1/2}$ state near the magic wavelength is $8 \times 10^{-3}$ a.u./$(2\pi \times \mathrm{GHz})$. Therefore, the

measurement must be sensitive to the Stark shift due to a dynamic dipole polarizability of $\sim 2$ a.u., which corresponds to $\sim 2\pi \times 10$ Hz ac Stark shift resolution [148] assuming light power of $\sim 1$ mW focused to a $\sim 25$ $\mu$m beam waist is used. The required power at the desired wavelength can be obtained from a shared Ti:sapphire laser (BIFROST) in the UCSB physics department.

Such a small ac Stark shift can be resolved with a $^{226}$Ra$^+$ optical clock running for $\sim 100$ s [8], with a systematic uncertainty of $< 1$ Hz. However, we anticipate that a future $^{225}$Ra$^+$ optical clock would reduce both the statistical and the systematic uncertainty, and therefore we plan to measure this with $^{225}$Ra$^+$ in the future.

It is important to note that systematic effects are not included in the above analysis yet, such as the ac Stark shifts of other transitions and the $D_{5/2}$ state and the laser amplified spontaneous emission noise [149].

## 9.2.4 $D_{3/2}$ and $D_{5/2}$ state lifetimes

We are also working on lifetime measurements of the $6d$ states. Previously, only a lower bound on the $D_{5/2}$ state lifetime is available ($\tau_{D_{5/2}} > 232$ ms [46]). Accurate measurements of the $6d$ state lifetimes are important for estimating the expected performance of a radium ion optical clock and for testing theoretical calculations of heavy atoms.

We measure the lifetimes of the $6d$ states with a single trapped $^{226}$Ra$^+$. The pulse sequences of both measurements are shown in Fig. 9.1. Measurements of both states start with Doppler cooling and a state detection (SD1) of the ion. For the $D_{5/2}$ state lifetime measurement, we prepare the ion in the $D_{5/2}$ state by optical pumping of the $S_{1/2} \rightarrow P_{1/2}$ and the $D_{3/2} \rightarrow P_{3/2}$ transitions (P1). After that, a state detection (SD2) follows to confirm that the ion is prepared in the $D_{5/2}$ state. A variable wait time and another state detection (SD3) follows to determine the probability of decay during the wait time.

The $D_{3/2}$ state lifetime measurement is similar, except that the state preparation is done by the $S_{1/2} \to D_{3/2}$ transition, and before state detection, we use the $D_{3/2} \to P_{3/2}$ transition to pump a fraction of the $D_{3/2}$ population to the $D_{5/2}$ state, limited by the branching fraction from the $P_{3/2}$ state to the $D_{5/2}$ state. The state detection measures the population in the $D_{5/2}$ state which is proportional to the population in the $D_{3/2}$ state at the end of the wait time.

| step | SD1 | P1 | SD2 | Wait | SD3 |
|------|-----|-----|-----|------|-----|
| ion state | | | | | |
| time (µs) | 1000 | 200 | 1000 | variable | 1000 |

a) D$_{5/2}$ lifetime sequence

| step | SD1 | P1 | Wait | P2 | SD2 |
|------|-----|-----|------|-----|-----|
| ion state | | | | | |
| time (µs) | 1000 | 50 | variable | 50 | 1000 |

b) D$_{3/2}$ lifetime sequence

Figure 9.1: Lifetime measurement pulse sequences of (a) the $D_{5/2}$ state and (b) the $D_{3/2}$ state. The inset figures show how population moves between the low-lying states of Ra$^+$ during these steps. Solid arrows represent lasers on during a step, and dashed arrows indicate the decay paths during optical pumping. Double-sided arrows are cycling transitions that form closed loops.

Preliminary data of the $D_{5/2}$ state lifetime measurement is shown in Fig. 9.2. For data points with wait times less than 1.5 s, the population in the $D_{5/2}$ state follows an exponential decay with time as expected. However, for wait times greater than 2 s, it is clear that the exponential trend is no longer true. We think the deviations at longer wait times are due to elastic collisions between the trapped radium ions with the residual

gas in the vacuum chamber, potentially due to collisions with $^{222}$Rn atoms from $^{226}$Ra radioactive decays. If all decayed radon atoms are released in the vacuum chamber, the equilibrium partial pressure due to $^{222}$Rn is approximately $10^{-9}$ torr [1]. These collisions could heat up the trapped $^{226}$Ra$^+$ ion so the number of collected fluorescence photons during the final state detection may be small and the state detection event is characterized as "dark" even if the ion has decayed to the $S_{1/2}$ state. The particles emitted from radioactive decays may also collide with the trapped ion and cause heating.
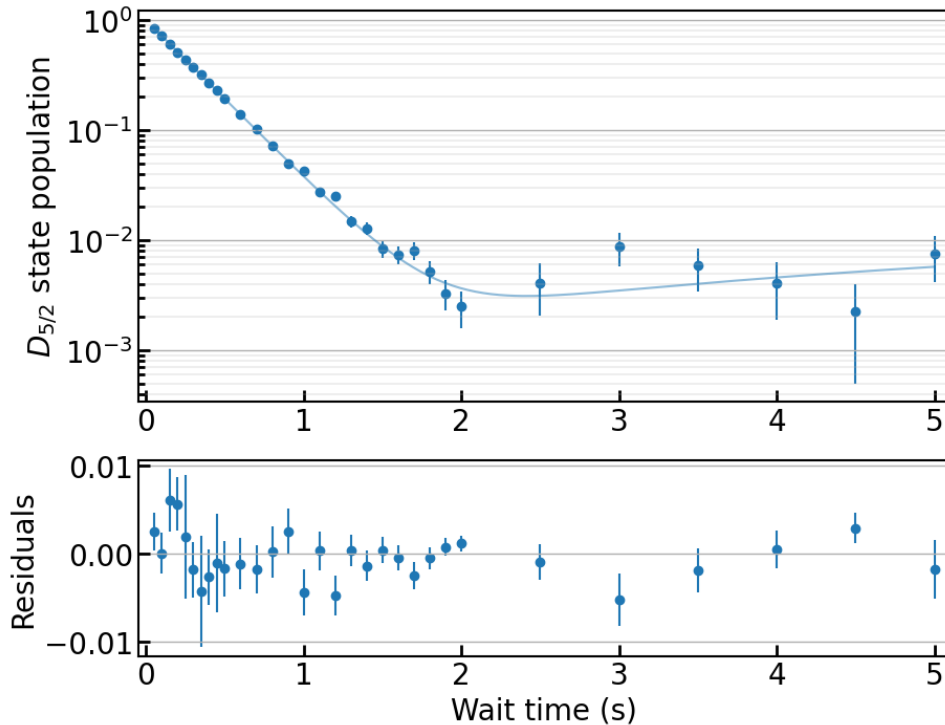


Figure 9.2: Measurement data of the $D_{5/2}$ state lifetime. The upper panel shows the dark state detection (SD) probability as a function of wait time. The blue line shows the fitting (see main text). The lower panel shows the residuals of the data to the fit.

We fit the data to a model that assumes the probability of such elastic collisions is

---

[1] Due to the large recoil energy on radon after the alpha decay, we anticipate most of the radon atoms embed into the vacuum chamber after decaying. The exact fraction of radon atoms released as gas is difficult to estimate.

proportional with dark time. With this model the dark state detection probability is

$$p_{\text{dark}} = e^{-t/\tau} + bt(1 - e^{-t/\tau}), \tag{9.7}$$

where $\tau$ is the $D_{5/2}$ lifetime, and $b$ is the collision rate. The data in Fig. 9.2 gives a statistical $D_{5/2}$ lifetime of $\tau_{D_{5/2}} = 303.4(9)$ ms, and a collision rate $b = 1.6(2) \times 10^{-3}$ Hz. We also measured the statistical lifetime of the $D_{3/2}$ state to be $\tau_{D_{3/2}} = 623(15)$ ms, and a collision rate $b = 2.0(6) \times 10^{-3}$ Hz.

As the measurement is limited by the background gas collisions right now, we postponed publishing the preliminary measurements and work on improving the vacuum. One important planned upgrade is changing the radium isotope from radium-226 to radium-225. As radium-225 does not have gas element such as radon in its decay chain, switching to $^{225}$Ra$^+$ should improve the vacuum and reduce the collision rate. We also note that we do not observe collisions up to 1.5 s ($\sim 5\tau_{D_{5/2}}$) for the $D_{5/2}$ lifetime measurement. We note that such measurements at longer wait times than $5\tau$ is not typical [35, 150, 151, 152, 153], and we extend the measurement times and check for such systematic effects because the statistical uncertainty of this measurement is exceptionally small ($\sim 0.3\%$ for the $D_{5/2}$ state).

We can also update the pulse sequence with the new control capabilities we have realized since this preliminary measurement. Previously, we were using optical pumping through the 708 nm $D_{3/2} \rightarrow P_{3/2}$ transition to detect population in the $D_{3/2}$ state by shelving it to the $D_{5/2}$ state. An alternative method is to use $S_{1/2} \rightarrow D_{5/2}$ clock pulses to transfer the population of the ground state to the $D_{5/2}$ state. Either a $\pi/2$ pulse can be used or adiabatic rapid passage [154] can be implemented to improve efficiency and reliability. This will effectively increase the detection efficiency by $\sim 10$ times for the $D_{3/2}$ lifetime measurement.

# Chapter 10

# Coherent control of the Ra$^+$ optical qubit

The optical clock transition in the radium ion enables coherent control of the radium ion optical qubit. In this chapter we report the progress on the optical qubit and manipulation of the motional states with the optical qubit.

## 10.1    $^{226}$Ra$^+$ $S_{1/2} \to D_{5/2}$ transition

The $S_{1/2} \to D_{5/2}$ 728 nm transition in Ra$^+$ is an $E2$ transition with sub-Hz linewidth. The $D_{5/2}$ metastable state has a natural lifetime of $\sim 0.3$ s, and predominately decays to the $S_{1/2}$ ground state with a small branching fraction to the $D_{3/2}$ state via $M1$ decays [56]. For $^{226}$Ra$^+$ which has a nuclear spin of zero, there are two Zeeman levels in the ground state and six in the metastable state. According to the $E2$ transition selection rule $|\Delta m| \leq 2$, a total of ten transitions between the Zeeman levels of the two states are allowed. The relative strength of driving these different Zeeman transitions are controlled by the laser $k$ vector, polarization, and the magnetic field [94]. These transitions are

typically spaced $\sim 1 - 10$ MHz apart with an applied magnetic field of a few gauss, and they are fully resolved with a narrow-linewidth laser.

The secular motion and micromotion of the trapped ion modulate the laser frequency via the Doppler effect which results in secular motion and micromotion sidebands of these Zeeman transitions (See Sections 2.1 and 2.3). Because the secular motion is thermal, we can use the secular sidebands to control the motional quantum number of the trapped ion in the corresponding secular mode, as introduced in Section 5.2.1. The secular sidebands both enable sideband cooling of a secular motion mode to the ground state of the harmonic oscillator and provide a method to entangle different ions in the same trap using the shared motional mode.

Before controlling the qubit using the transition, we first observed quantum jumps of the ion [155] by scanning an unstabilized 728 nm laser across the transition. We conducted spectroscopy on the transition to determine its frequency [140], and then ran a self-compared optical clock using the transition [8] with a stabilized laser locking to a high-finesse cavity. More details about the radium ion optical clock can be found in [61].

## 10.2   Sideband cooling

The narrow linewidth also enables driving a single carrier or sideband transition for state preparation and sideband cooling. We set up the 728 nm laser along the trap axis, so the laser is only sensitive to the axial secular motion of the ion. The axial secular frequency is $2\pi \times 232$ kHz for a single $^{226}$Ra$^+$ ion, corresponding to a Lamb-Dicke parameter of 0.084. After Doppler cooling, the mean phonon number on the axial mode is $\bar{n} \approx 50$, so the ion is outside of the Lamb-Dicke regime, and cooling on multiple red sidebands are helpful for efficient sideband cooling to the ground motional state.

We sideband cool the ion using first the second order red sideband and then the first

order red sideband to achieve a mean phonon number of 0.12(2) after sideband cooling, measured from the ratio of red and blue sidebands after cooling (See Fig. 10.1).
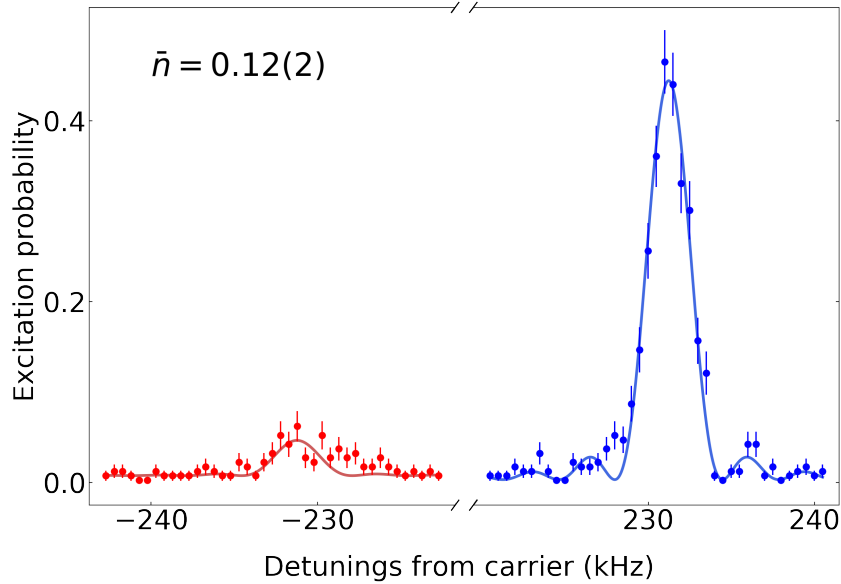


Figure 10.1: Spectroscopy on the first-order red and blue sidebands after sideband cooling. The mean phonon number is calculated from Eq. 5.15.

After cooling the axial motional mode to near the ground state, the majority of the population is in the $n = 0$ motional state, and we can conduct Rabi flopping on the blue sideband, shown in Fig. 10.2. At $t = 300 \, \mu$s, approximately 80% of the population is in the $n = 1$ Fock state. Future experimental upgrades such as higher secular frequencies, using first-order magnetic field insensitive transitions in $^{225}$Ra$^+$, and magnetic field stabilization should improve the fidelity.

## 10.3   Magnetic field fluctuations

There is no magnetic-field insensitive clock transition with $^{226}$Ra$^+$. The $S_{1/2}$ state has a Landé $g$ factor of $\sim 2$, and the $D_{5/2}$ state has a Landé $g$ factor of $\sim 1.2$. The least magnetic field sensitive transitions, $m_{S_{1/2}} = \pm 1/2 \rightarrow m_{D_{5/2}} = \pm 1/2$, have a Zeeman shift

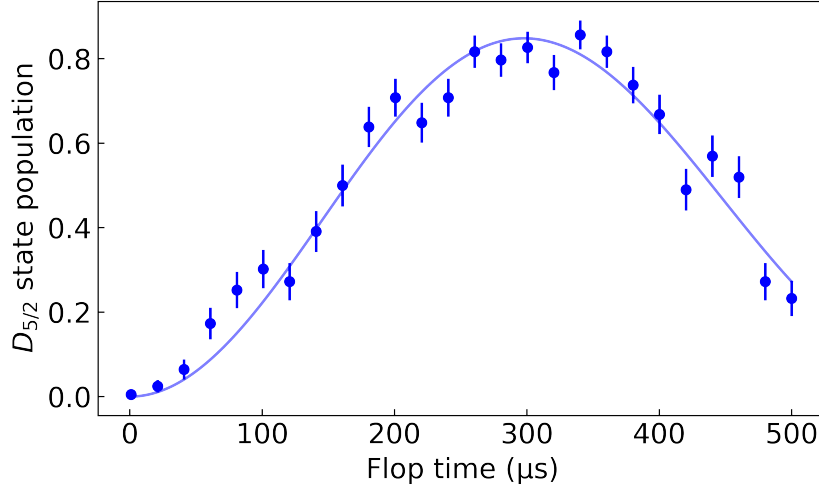Figure 10.2: Rabi flopping on the blue-sideband after sideband cooling. The fidelity is limited by the phonon distribution after sideband cooling and magnetic field fluctuations.

sensitivity of $\mp 2\pi \times 0.56$ MHz/gauss. The most sensitive transitions, $m_{S_{1/2}} = \pm 1/2 \rightarrow m_{D_{5/2}} = \mp 3/2$, have a sensitivity of $\mp 2\pi \times 3.92$ MHz/gauss. A sub-Hz second-order Zeeman shift arises from fine-structure mixing of the $D_{3/2}$ and the $D_{5/2}$ state [8] which is negligible in most of the experiments except the optical clock.

One of the largest short-term fluctuating magnetic field comes from the ac power line at 60 Hz. We trigger the experiment pulse sequences relative to the ac power line to suppress the effect of the 60 Hz power line noise. By changing phase of the trigger on the 60 Hz power line, we can map out the Zeeman shift of the $m_{S_{1/2}} = 1/2 \rightarrow m_{D_{5/2}} = 5/2$ transition as a function of the phase relative to the ac power line as shown in Fig. 10.3. The corresponding peak-to-peak magnetic field fluctuation at 60 Hz is $\sim 10^{-3}$ gauss. We use feedforward current in a coil near the ion trap to suppress the 60 Hz noise [156]. The feedforward signal is supplied by a Red Pitaya STEMlab 125-14 with its output triggered by the ac power line. The Red Pitaya output is amplified by a low-noise current amplifier. This feedforward setup can reduce the 60 Hz noise by a factor of 5.

The long-term fluctuation of the magnetic field is monitored with a clock experiment.
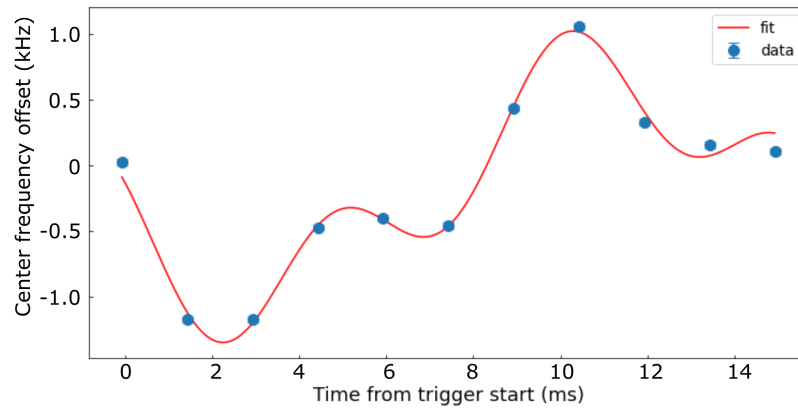
Figure 10.3: Transition frequency shift of the $S_{1/2}, m = 1/2 \to D_{5/2}, m = 5/2$ transition at different phase relative to the 60 Hz ac power line without feedforward compensation. A probe time of 1 ms is used. The fit curve is a superposition of the first three harmonics of 60 Hz sine waves.

A recording of typical magnetic field fluctuations is shown in Fig. 10.4. We are working on implementation of long-term magnetic field feedback with magnetic field sensors close to the ion trap and wire coils on all three axes to compensate for the magnetic field fluctuations.
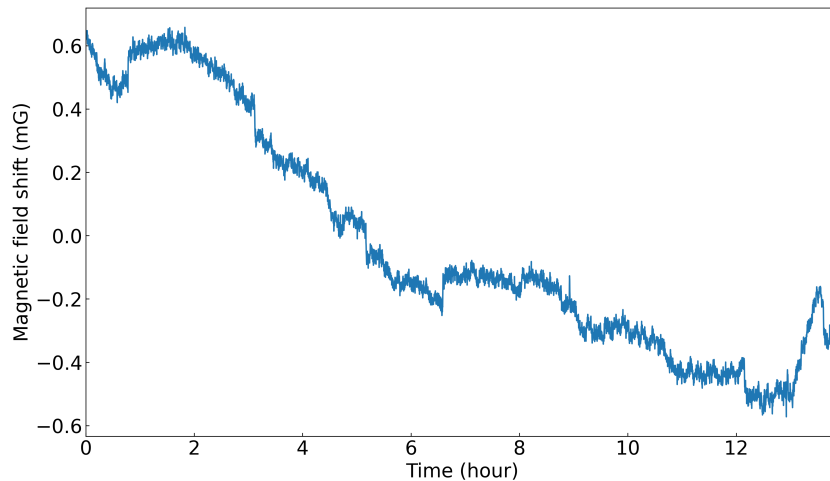


Figure 10.4: Magnetic field fluctuation during a $\sim 14$ hour run of the $^{226}$Ra$^+$ optical clock. Fluctuation of a few milligauss over a day is typical.

We are also working on trapping $^{225}$Ra$^+$ which has magnetic field insensitive transitions that will reduce the Zeeman shifts. The $S_{1/2}, F = 0, m_F = 0 \to D_{5/2}, F = 2, m_F = 0$

89

transition, for example, is first-order magnetic field insensitive at zero field. The second-order Zeeman shift coefficient is calculated to be -1.13 kHz/gauss$^2$ for this transition, so the magnetic field sensitivity of this transition is approximately 1% of the least sensitive clock transition in $^{226}$Ra$^+$ at a typical experimental field of a few gauss. We anticipate that both magnetic field stabilization and using magnetic field insensitive transitions in $^{225}$Ra$^+$ can help us to improve the coherence time of the optical qubit.

# Chapter 11

# Production and detection of heavy radioactive molecules

To realize our goal of a hadronic $CP$ violation measurement using radioactive molecular ions, we need to produce and identify them first. In the chapter, we summarize our work on producing $^{226}$Ra-containing molecular ions, whose $^{225}$Ra isotopologues have high $CP$ violation sensitivities. We also introduce a new optical mass spectrometry technique for identification of molecular ions.

## 11.1  Optical mass spectrometry of cold RaOH$^+$ and RaOCH$_3^+$

This section describes production and detection of RaOH$^+$, RaOD$^+$, RaOCH$_3^+$, and RaOCD$_3^+$. The contents of this section include our paper *Optical mass spectrometry of cold RaOH$^+$ and RaOCH$_3^+$* [9].

We present an all-optical mass spectrometry technique to identify trapped ions. The new method uses laser-cooled ions to determine the mass of a cotrapped dark ion with

a sub-dalton resolution within a few seconds. We apply the method to identify the first controlled synthesis of cold, trapped $RaOH^+$ and $RaOCH_3^+$. These molecules are promising for their sensitivity to time and parity violations that could constrain sources of new physics beyond the standard model. The nondestructive nature of the mass spectrometry technique may help identify molecular ions or highly charged ions prior to optical spectroscopy. Unlike previous mass spectrometry techniques for small ion crystals that rely on scanning, the method uses a Fourier transform that is inherently broadband and comparatively fast. The technique's speed provides new opportunities for studying state-resolved chemical reactions in ion traps.

*Introduction.*—Ion traps are powerful tools because their ability to trap only depends on two properties: the mass and charge of a particle. Therefore they can trap ionic species with rich internal structures that preclude laser cooling or fluorescence. Such dark ions include molecules, highly charged ions, and atoms with transitions that are deep in the UV. These ions can be sympathetically cooled by cotrapped laser-cooled ions, where they appear as dark ion defects in a Coulomb crystal. Dark ions have seen great successes in optical clocks, e.g., $Al^+$[5], constraining new physics, e.g., $HfF^+$[71] and studying state-resolved chemical reactions, e.g., $BaCl^+$[157] and $RbSr^+$[158]. There has also been much progress with highly charged ions, which generally lack strong fluorescence transitions, for metrology and tests of fundamental constant variations [159, 160, 161]. In this work we have synthesized a pair of molecular ions that are promising for probing new physics: $RaOH^+$ and $RaOCH_3^+$.

Recent measurements of parity ($P$) and time-reversal ($T$) violating moments are now probing physics at energy scales beyond the direct reach of the Large Hadron Collider [70]. Radium-based molecules are promising for constraining hadronic $P$, $T$-odd forces [91, 86, 54]. The heavy and octupole-deformed radium nucleus enhances sensitivity to new physics in the hadronic sector [162, 4]. This sensitivity is further enhanced when radium

is incorporated into molecules such as $RaOH^+$ or $RaOCH_3^+$ [163, 86, 91] that have large effective electric fields and molecular structure that is critical for reducing systematic uncertainties. An ion trap is advantageous for working with radioactive molecules as high measurement sensitivity can be achieved with small sample sizes due to long measurement times [71, 164]. For example, the long trap times combined with the high sensitivity of $^{225}RaOCH_3^+$ are sufficient for an experiment with even a single trapped molecule to set new bounds on hadronic $P$, $T$ violations [87].

Because dark ions do not fluoresce, mass spectrometry techniques are commonly used for species identification. We present a new nondestructive optical mass spectrometry (OMS) technique to identify a trapped dark ion in a Coulomb crystal by measuring a motional frequency of the crystal. In this work, we use cotrapped laser-cooled ions to amplify the secular (normal mode) motion of the crystal by using coherent population trapping (CPT) in the $S_{1/2}$ - $P_{1/2}$ - $D_{3/2}$ $\Lambda$-level system [165] common to $Ca^+$, $Sr^+$, $Ba^+$, and $Ra^+$. For these ions, it is fast and straightforward to realize CPT by changing the frequency and power of the $P_{1/2} \rightarrow D_{3/2}$ repumping laser from the laser cooling values with an acousto-optical modulator. With CPT, the optical spectrum of the $S_{1/2} \rightarrow P_{1/2}$ cooling transition can be modified so the ion's motion is coherently amplified [93], which modulates the scattered light at the motional frequency and its harmonics, which can then be measured with a Fourier transform. Because the motional modes of the ion crystal are set by the charge and mass of the trapped particles, motional frequencies can be used to determine the ion's mass. The OMS technique can be used with any laser-cooled ion, even without using a $\Lambda$ structure, e.g., $Be^+$, $Mg^+$, or $Yb^+$, via "phonon lasing" with bichromatic light [166].

Many techniques have been used to identify trapped dark ions in Paul traps. The best technique for large Coulomb crystals (hundreds to thousands of ions) with multiple dark ion species is time-of-flight mass spectrometry, but it is inherently destructive and

requires a purpose-built trap and custom electronics [167, 168, 169]. In the regime of small ion crystals with a few dark ions, multiple techniques have been developed that rely on measuring a trap secular frequency, including secular motion excitation by applied electric fields (tickle scans) [170, 171, 172], optical sideband spectroscopy [173], and ion crystal phase transitions [174]. Optical sideband spectroscopy requires a narrow linewidth laser and is also slow ($\sim$ 1 minute). Measuring phase transitions has limited performance due to the large mass uncertainties ($\sim$ 5 daltons [174]). A tickle scan typically requires a $\geq$ 1 minute measurement where an electrical drive is scanned over the secular frequency, which results in a broad resonance peak due to the damping from the laser cooling that is required by the technique. The applied electric field can also destructively drive ions out of the trap. Despite these drawbacks and the need for additional electrical connections (which are a noise conduit), for small crystals the tickle scan has been the most widely used technique. A variation of the tickle scan method modulates the cooling light intensity instead of modulating an electrical drive [175]. This removes some drawbacks but with an increase in technical overhead. In order for any of these techniques to achieve reasonable measurement times ($\sim$1 minute), *a priori* knowledge of the trapped dark ions is required to reduce the secular frequency scan range. In comparison to these small ion crystal mass spectrometry techniques, the reported OMS technique is faster, does not require knowledge of the dark ion's mass, is less invasive, and is a simple extension to Doppler cooling.

*Secular motion amplification by coherent population trapping*—We use CPT in Ra$^+$ to amplify the ion crystal's motion. For Doppler cooling, the cooling laser at 468 nm is red-detuned, $\Delta_{\mathrm{SP}} < 0$, from the $S_{1/2} \to P_{1/2}$ transition, and a repumping laser at 1079 nm is blue-detuned, $\Delta_{\mathrm{DP}} > 0$, from the $D_{3/2} \to P_{1/2}$ transition that brings the population back into the cooling cycle [93], see Fig. 11.1. The high scattering rate of laser cooling can be significantly reduced by the CPT that occurs when $\Delta_{\mathrm{SP}} = \Delta_{\mathrm{DP}}$ [176]. For CPT

motional amplification the condition is less stringent as setting $\Delta_{\mathrm{SP}} < \Delta_{\mathrm{DP}} < 0$ (see Fig. 11.1), heats the ion crystal because the 468 nm spectrum has a local slope that is negative due to the excitation suppression from CPT at $\Delta_{\mathrm{SP}} = \Delta_{\mathrm{DP}}$. However, the heating is bounded by the 468 nm global spectrum which has a positive slope for $\Delta_{\mathrm{SP}} < 0$, that cools the heated ion's motion once it reaches a sufficient amplitude where the global cooling spectrum is Doppler shifted into resonance. The trapped ions then maintain an amplified equilibrium orbit when the optically induced "local heating" and "global cooling" effects balance [177, 24].
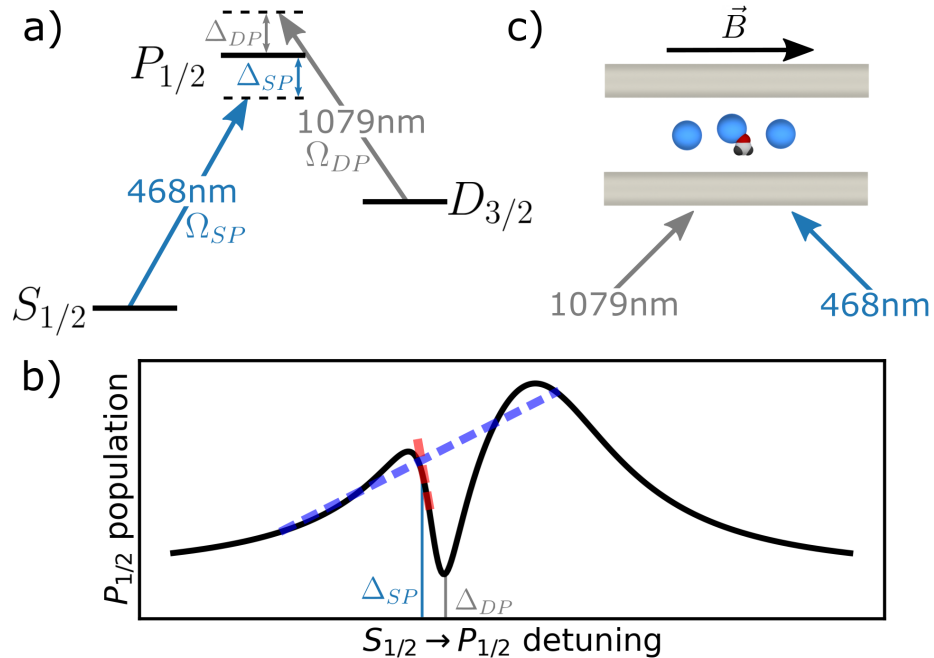


Figure 11.1: (a) $\mathrm{Ra}^+$ energy levels and transitions used in this work. $\Delta_{\mathrm{SP}}$ ($\Delta_{\mathrm{DP}}$) is the detuning, and $\Omega_{\mathrm{SP}}$ ($\Omega_{\mathrm{DP}}$) is the Rabi frequency of the 468 (1079) nm light. (b) The $S_{1/2}$ to $P_{1/2}$ spectrum with $\Delta_{\mathrm{SP}}$ and $\Delta_{\mathrm{DP}}$ set to amplify ion motion. The local slope at $\Delta_{\mathrm{SP}}$ (red dashed line) is negative, while the global slope (blue dashed line) is positive. (c) OMS geometry with two $\mathrm{Ra}^+$ and one $\mathrm{RaOCH_3}^+$ shown between two radial trap electrodes, as well as the relative orientation of the cooling and repumping light and the magnetic field.

For OMS identification of $\mathrm{RaOH}^+$ and $\mathrm{RaOCH_3}^+$, we apply a 2.5 gauss magnetic field along the trap axial direction. The $k$ vectors of both lasers are at $45°$ with respect to

Figure 11.2: $P_{1/2}$ state population as a function of 468 nm detuning. A fit of the spectrum to a numerical solution of the $\Lambda$-level system that accounts for all Zeeman levels [178, 179] gives: $\Delta_{DP}/2\pi = -10\,\mathrm{MHz}$, $\Omega_{SP}/2\pi = 19\,\mathrm{MHz}$, and $\Omega_{DP}/2\pi = 13\,\mathrm{MHz}$. The blue line at $\Delta_{SP}/2\pi = -22\,\mathrm{MHz}$ is the detuning of the 46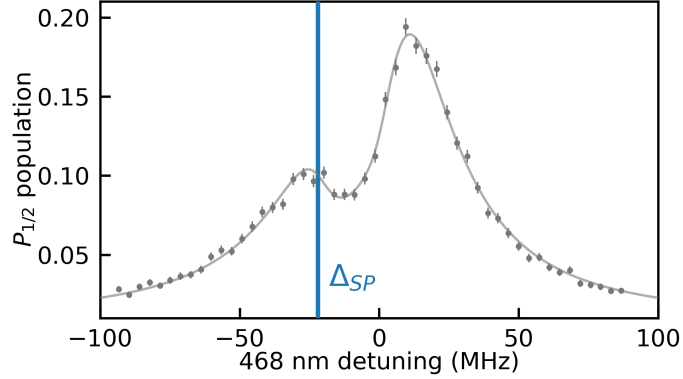8 nm light used for CPT amplification. The $P_{1/2}$ state population is not suppressed to zero at $\Delta_{SP} = \Delta_{DP}$ due to the finite linewidths of both the 468 and 1079 nm lasers ($\sim 3$ MHz).

all trap axes and are linearly polarized perpendicular to the magnetic field direction (see Fig. 11.1). Each laser's frequency and amplitude is controlled with an acousto-optical modulator. The multipeak spectrum of the cooling laser (see Fig. 11.2), enables "local heating, global cooling" that amplifies the ion motion up to a fixed value. The 1079 nm light, with a $k$ vector perpendicular to the 468 nm light, see Fig. 11.1 (c), breaks the degeneracy between the axial and radial directions so that the CPT only amplifies motion along the axial direction, see [177]. To switch from CPT amplification to Doppler cooling, we detune $\Delta_{DP}$ positive so the CPT excitation suppression is far from $\Delta_{SP}$.

*OMS of radium-based molecular ions*—We trap $^{226}\mathrm{Ra}^+$ ions in a linear Paul trap with a radio frequency (rf) drive of $\Omega_{rf}/2\pi = 1\,\mathrm{MHz}$, radial electrode to trap center distance $r_0 = 3.0\,\mathrm{mm}$ and axial electrode to trap center distance $z_0 = 7.5\,\mathrm{mm}$ (for details see [7]). For a single $\mathrm{Ra}^+$, the axial secular frequency is $\omega_z/2\pi = 27.8\,\mathrm{kHz}$. The 468 nm fluorescent photons are collected and sent to a camera and a photomultiplier tube (PMT), and the counts are time-tagged using a field-programmable gate array [118].

We laser cool three $\mathrm{Ra}^+$ ions and apply CPT amplification to increase the secular
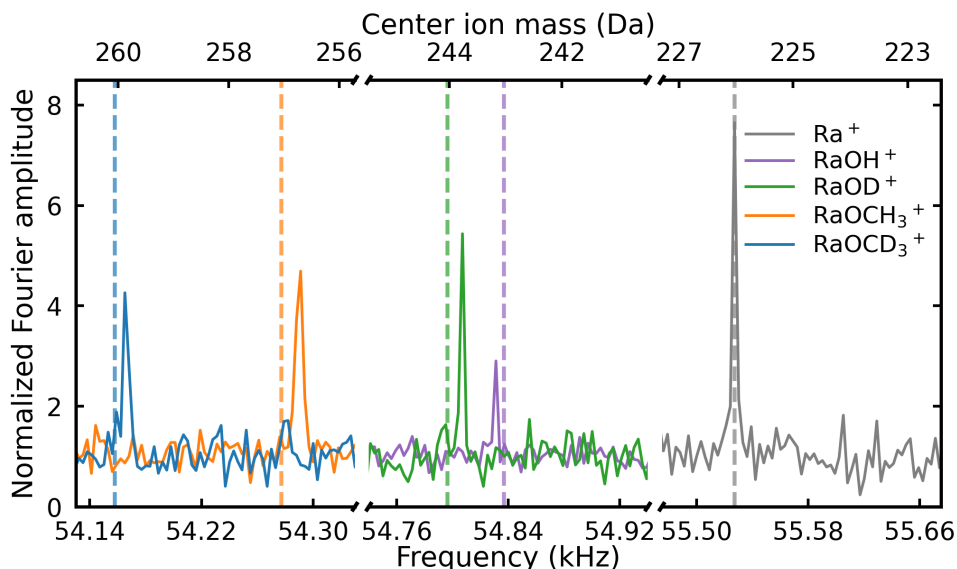
Figure 11.3: Fourier transformed PMT counts for Coulomb crystals where two $Ra^+$ surround a third ion, labeled in the legend, in a linear chain. The Fourier amplitudes are normalized by their backgrounds for clarity. The dashed vertical lines show the calculated center ion masses. The peak amplitudes vary due to drift in the power and frequency of the 468 and 1079 nm lasers over the span of several days during which the measurements were taken.

motion amplitude on the axial center-of-mass (COM) mode to 22(3) $\mu$m. A Fourier transform of the PMT counts while the ion motion is CPT amplified gives the OMS signal. The signal is calibrated by using known (fluorescing) ions. In this case three $Ra^+$ ions are used for calibration (see Fig. 11.3). Next, either methanol vapor or the deuterated equivalent is introduced to react with the laser-cooled $Ra^+$. A chemical reaction produces a dark ion defect in the crystal and drops the PMT counts by roughly 1/3. If the dark ion is not in the middle of the crystal we re-order the ions to meet this condition by blue-detuning the 468 nm light, $\Delta_{SP} > 0$, for $\sim 1$ s, which heats the trapped ions. We apply OMS to find the secular frequency and with the calibration measurement we can calculate the center ion's mass [177], see Fig. 11.3. Each trace is an average of ten 1/3 s long measurements. The second harmonics of the secular frequencies are used because in our experimental setup they are the strongest Fourier components.

|        | RaOH$^+$     | RaOD$^+$     | RaOCH$_3$$^+$ | RaOCD$_3$$^+$ |
|--------|-------------|-------------|--------------|--------------|
| Stat.  | 243.19(7)   | 243.79(7)   | 256.72(8)    | 259.85(8)    |
| Syst.  | 0.01(11)    | 0.21(11)    | 0.34(11)     | 0.22(11)     |
| Final  | 243.20(14)  | 244.01(14)  | 257.06(14)   | 260.07(14)   |
| Calc.  | 243.03      | 244.03      | 257.04       | 260.06       |

Table 11.1: Statistical results (Stat.) and systematic shifts and uncertainties (Syst.) of the radium-based molecular ion masses measured by OMS in daltons. The final molecular ion masses are calculated from a linear sum of the shifts, and the final uncertainties are given by summing the uncertainties in quadrature. See [177] for details on the systematics. For comparison the calculated molecular ion masses (Calc.) are given [184].

The difference in the mass spectrum of molecules when the trapped ions are exposed to methanol versus deuterated methanol confirms that we are producing the molecular ions identified by mass. When methanol is introduced only RaOCH$_3$$^+$ [180, 181, 182] and RaOH$^+$ [183] are created, while RaOCD$_3$$^+$ and RaOD$^+$ are only formed with deuterated methanol. The differences between the measured and calculated second harmonics of the secular frequencies are all within 13 Hz, corresponding to a fractional mass difference of $m/\Delta m \sim 800$ in a 3 s measurement. We observe that with a methanol (deuterated) background pressure of $\sim 5 \times 10^{-10}$ torr, RaOH$^+$ (RaOD$^+$) is not chemically stable and typically reacts in a few minutes to form RaOCH$_3$$^+$ (RaOCD$_3$$^+$), which is easily detected because the OMS technique is fast, precise, and broadband.

The OMS statistical uncertainty of 3 Hz was set by the Fourier transform resolution, which in turn comes from a 1/3 s data acquisition memory limit. The line center is found with a Lorentzian fit, which has an uncertainty ($< 0.1$ Hz) that is much less than the Fourier frequency resolution. We also consider systematic effects including trap potential drift, secular motion amplitude shifts, and micromotion shifts [177]. Both the statistical and systematic effects contribute to the ion mass uncertainty or shift by much less than 1 dalton, as summarized in Table 11.1.
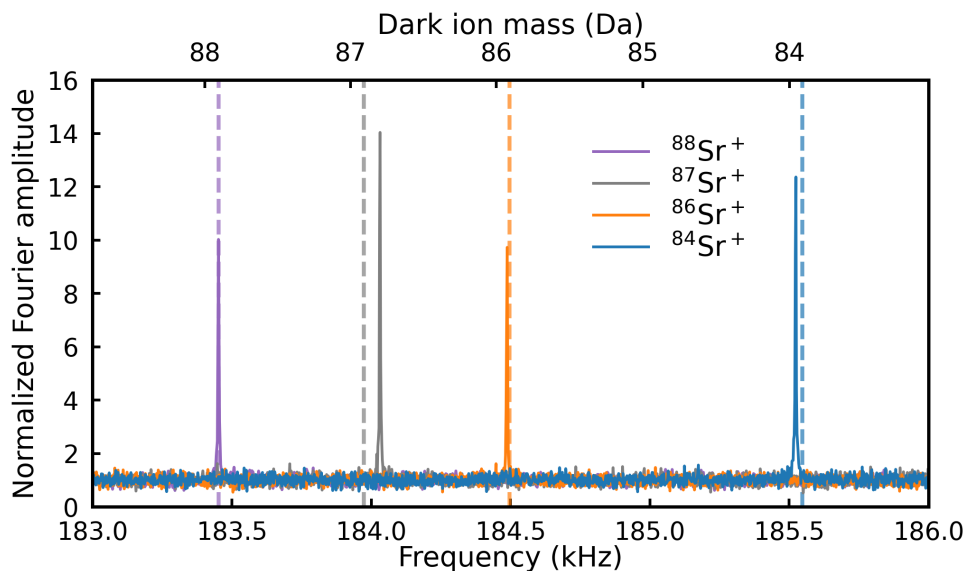
Figure 11.4: Fourier spectra of the fluorescent light from $^{88}Sr^+$ which is in a crystal with a second $^{88}Sr^+$, $^{87}Sr^+$, $^{86}Sr^+$, or $^{84}Sr^+$ ion. The calculated dark ion masses for the above crystals are shown as dashed vertical lines in the plot [177].

*OMS in a high frequency ion trap*—In a separate experimental apparatus, we confirm the OMS technique with strontium isotopes 88, 86, and 84, which we also identify with fluorescence. We demonstrate that the statistical mass sensitivity can be enhanced with a higher frequency ion trap ($r_0 = 0.6\,\mathrm{mm}$, $z_0 = 2.5\,\mathrm{mm}$, $\Omega_{\mathrm{rf}}/2\pi = 22\,\mathrm{MHz}$). The axial secular frequency for a single $^{88}Sr^+$ is $\omega_z/2\pi = 91.7\,\mathrm{kHz}$. We trap two-ion crystals with one $^{88}Sr^+$ and one $^{88,87,86,84}Sr^+$, and measure the axial COM secular frequencies of the crystal by OMS with CPT amplification applied to the $^{88}Sr^+$. $^{87}Sr^+$ is identified only with OMS.

The Fourier spectra of second harmonics of the axial COM secular frequency are shown in Fig. 11.4. The mass labels are calibrated using two $^{88}Sr^+$ ions [177]. Each trace is an average of ten 0.5 s measurements. The corresponding statistical mass resolution is $m/\Delta m_{\mathrm{stat}} \sim 20\,000$. The sub 1 dalton discrepancies between measured and calculated masses are primarily due to temporal drift of the trap potential.

*Conclusion*—We have produced $^{226}RaOH^+$ and $^{226}RaOCH_3^+$ molecules in this work.

Their isotopologues $^{225}$RaOH$^+$ and $^{225}$RaOCH$_3{}^+$ are proposed for nuclear Schiff moment measurements [86, 91], and can be produced with trapped $^{225}$Ra$^+$ and methanol. The production, sympathetic cooling, and fast nondestructive identification of these radioactive polyatomic molecular ions enables studying their internal structure with techniques such as photodissociation spectroscopy [185] or quantum logic spectroscopy [15, 186].

The short measurement time and sub-dalton mass resolution could enable detection of short-lived molecular ions, as demonstrated in this Letter using RaOH$^+$ and RaOD$^+$ which are metastable when in the presence of a methanol background. We note that the measurement time can be further reduced to $0.1\,\mathrm{s}$ or less with an iris to selectively collect ion fluorescence on one end of the amplified ion motion. With such a short measurement time it is possible to apply this technique to study the dissociation channels of radium-based molecular ions. For example, Ra$^+$ in the $D_{5/2}$ state (lifetime $0.3\,\mathrm{s}$ [56]) is optically indistinguishable from a radium-based molecular ion as neither of them fluoresce during Ra$^+$ Doppler cooling, but can be distinguished with mass spectrometry. This provides a new tool to study the electronic states of chemical reaction products. The simultaneous determination of product and reactant states can be achieved by combining this method with optical pumping, which will help investigate full reaction pathways with single particles [158, 187]. The technique may also be used to rapidly characterize the motional frequencies of an ion trap. For example, it could be incorporated into a feedback loop for the long-term stabilization of trap motional frequencies [188].

## 11.2  Production and detection of RaSH$^+$

Compared to the linear and symmetric-top polyatomic molecules RaOH$^+$ and RaOCH$_3^+$ molecules, the asymmetric-top RaSH$^+$ provides some advantages for a precision measurement using molecular ions. Similar to RaOCH$_3^+$, RaSH$^+$ has $K$-doublets in excited rotational states that live for more than minutes in cryogenic environments [87], much longer than the $\sim 1$ s lifetime of RaOH$^+$ vibrational science state [86]. The zero-field splitting of the $K$-doublet in RaSH$^+$ is $\sim 10$ MHz, which is much higher than the $\sim 100$ Hz splitting in RaOCH$_3^+$. A larger splitting reduces the unwanted coupling due to a rotating electric field that is necessary for polarizing trapped ions [71], as discussed further in Chapter 12.

We produce RaSH$^+$ from a chemical reaction of trapped $^{226}$Ra$^+$ and H$_2$S gas. We trap and cool three Ra$^+$ ions, and introduce H$_2$S from the precision leak valve until the vacuum chamber pressure measured from an ion gauge is $\sim 5 \times 10^{-9}$ torr. A radium ion reacts with H$_2$S gas typically after a few minutes, and we close the leak valve, and use OMS to measure the mass of the dark ion. A mass spectrum that confirms production of RaSH$^+$ is shown in Fig. 11.5.

With continuous laser cooling with saturated 468 nm and 1079 nm light, we observe that the RaSH$^+$ molecule dissociates after $\sim 1$ hour to Ra$^+$. With reduced 468 nm and 1079 nm light intensities, we have trapped RaSH$^+$ sympathetically cooled by Ra$^+$ for several hours without dissociation, but eventually the H$_2$O impurity introduced with H$_2$S reacted with RaSH$^+$ to produce RaOH$^+$, which is detected via another mass spectrometry.

The H$_2$S gas used above is produced from a chemical reaction of CuSO$_4$ and HCl. Due to the impurities in the produced H$_2$S (mostly HCl and H$_2$O), we detect RaCl$^+$ molecular ions, at masses $226 + 35$ Da for $^{35}$Cl or $226 + 37$ Da for $^{37}$Cl when leaking in
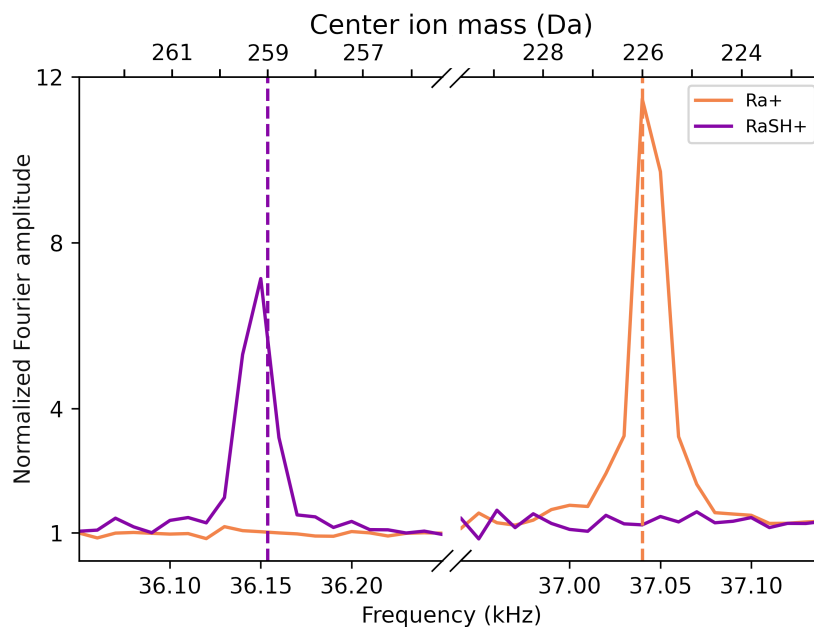
Figure 11.5: Fourier spectra of the $Ra^+$ fluorescent light from a $Ra^+$ - $RaSH^+$ - $Ra^+$ ion crystal. The calculated dark ion masses for the above crystals are shown as dashed vertical lines in the plot.

$H_2S$. In the future we can use commercially available argon - $H_2S$ mixture to prevent these problems.

## 11.3    Attempts to produce $RaH^+$ and $RaD^+$

We have produced radium-containing polyatomic molecular ions that are promising for $CP$ violation measurements. However, due to the geometry complexity and heavy masses of the ligands, these polyatomic molecular ions have many rotational levels that are populated at room temperature, which makes them difficult to study with a room temperature ion trapping setup. The diatomic molecules, $RaH^+$ and $RaD^+$, on the other hand, have only one rotational degree of freedom and the rotational constants are large (see Table 11.2), so at room temperature a significant fraction of population will be in the lowest five rotational states ($\sim 30\%$ for $RaH^+$ and $\sim 20\%$ for $RaD^+$). These

| | Rotational constant $B_e$ (GHz) | Vibrational constant $\omega_e$ (cm$^{-1}$) |
|---|---|---|
| $^{226}$RaH$^+$ (1 $^1\Sigma_{0+}$) | 102 | 1315 |
| $^{226}$RaH$^+$ (2 $^1\Sigma_{0+}$) | 69 | 683 |
| $^{226}$RaD$^+$ (1 $^1\Sigma_{0+}$) | 51 | 929 |
| $^{226}$RaD$^+$ (2 $^1\Sigma_{0+}$) | 35 | 483 |

Table 11.2: Rotational and vibrational constants of the two lowest singlet states of $^{226}$RaH$^+$ and $^{226}$RaD$^+$ [189].

states have relatively simple structures, and thus these molecular ions are good choices for benchmark quantum logic spectroscopy [16] before implementing the technique on polyatomic molecules which are more complex.

Similarly to the previous molecular ion experiments, we introduce hydrogen or deuterium from the precision leak valve to react with laser cooled radium-226 ions. The maximum hydrogen or deuterium pressure in the vacuum chamber where the Ra$^+$ ions remain trapped is about $1 \times 10^{-7}$ torr. This is similar or higher than the pressure required to produce other alkaline earth ion hydrides [190, 191, 192, 193]. At this pressure, for more than 10 hours of gas leaking we did not observe any molecular ion that lives longer than a few seconds and have a mass close to RaH$^+$ or RaD$^+$. All long-lived molecular ions that we have observed are confirmed to be RaO$^+$ or RaOH$^+$ from OMS.

During gas leaking, we saw several events where a bright Ra$^+$ became dark for $\sim 1$ s and is then bright again. The spacings between the ions did not change when the ion went dark, so these events are not due to elastic collisions where one ion is kicked out of the ion chain temporarily. In addition, the $D_{5/2} \to P_{3/2}$ cleanout laser is always on, so the possibility that a dark ion is produced due to collisional $j$-mixing from the $D_{3/2}$ state to the $D_{5/2}$ state is excluded. These short-lived dark ions are likely RaH$^+$ and RaD$^+$, but they dissociate too fast to be confirmed with available mass spectrometry techniques.

It is unclear why long-lived RaH$^+$ and RaD$^+$ are not produced. The reaction Ra$^+$($P_{1/2}$) + H$_2$ $\longrightarrow$ RaH$^+$($1\Sigma_{0+}$) + H is exothermic at 0.10 eV (RaH$^+$ ground electronic and vi-

brational state has a dissociation energy of $D_0 = 1.97$ eV [189]). The corresponding reactions for other alkaline earth ions release more energy, as shown in Table 11.3, and these reactions also happen faster. It is possible that the reaction of hydrogen with radium ion in the $P_{1/2}$ state does not emit enough energy to occur frequently.

| Species | Reaction released energy | Reaction rate at $1 \times 10^{-7}$ torr $H_2$ pressure |
|---------|--------------------------|----------------------------------------------------------|
| $Be^+$ | 2.6 eV [194] | $\sim 100$ mHz [190] |
| $Mg^+$ | 1.2 eV [195] | $\sim 100$ mHz [191] |
| $Ca^+$ | 0.8 eV [196] | $\sim 10$ mHz [197] |
| $Ba^+$ | 0.4 eV [193] | $\sim 1$ mHz [193] |
| $Ra^+$ | 0.1 eV [189] | $\sim 1$ mHz or $\lesssim 0.01$ mHz |

Table 11.3: Exothermic energy release of the $M^+(P_{1/2}) + H_2 \longrightarrow MH^+(1\Sigma_{0+}) + H$ and the approximate $1/e$ reaction rate for laser-cooled $M^+$ ions normalized to $1 \times 10^{-7}$ torr $H_2$ pressure, where M is Be, Mg, Ca, Ba, or Ra. No experimental literature on $Sr^+$ reaction with $H_2$ or $D_2$ has been found. The $Mg^+$ and $Ca^+$ reaction rate is calculated assuming the population in the $P_{1/2}$ excited state is 10%. All reaction rates are only for order-of-magnitude comparisons as they depend strongly on laser cooling parameters. The reaction rate for $Ra^+$ is not determined. If the short-lived molecular ions are not $RaH^+$, the reaction rate is less than 0.01 mHz. Otherwise, the reaction rate is approximately 1 mHz.

It is also possible that the short-lived dark ions are $RaH^+$ and $RaD^+$ that dissociate quickly to $Ra^+$ after reactions. As I do not have an alternative explanation of the dark ions, I think this hypothesis is likely true. However, the reason for dissociation is unknown. The most probable theory is that the 468 nm cooling laser for $Ra^+$ drives a two-step photodissociation process in the $RaH^+$ and $RaD^+$ molecules, similarly to how 397 nm light drives the $1\ ^1\Sigma_{0+} \to 2\ ^1\Sigma_{0+}$ and the $2\ ^1\Sigma_{0+} \to$ continumm transitions to dissociate $CaH^+$ [192, 198]. If photodissociation is indeed the case, both $^{226}RaH^+$ and $^{226}RaD^+$ must have a rotational transition within $1\ ^1\Sigma_{0+}, \mu = 0 \to 2\ ^1\Sigma_{0+}, \mu'$ that is reasonably close ($\lesssim 100$ GHz) to the $^{226}Ra^+$ cooling frequency at 640 096.63(6) GHz [7]. This possibility is confirmed by theoretical calculations as the $RaH^+$ $1\ ^1\Sigma_{0+}, \mu = 0 \to 2\ ^1\Sigma_{0+}, \mu' = 0$ transition is calculated to be 642.7 THz with several THz of uncertainty [189], see

Fig. 11.6.
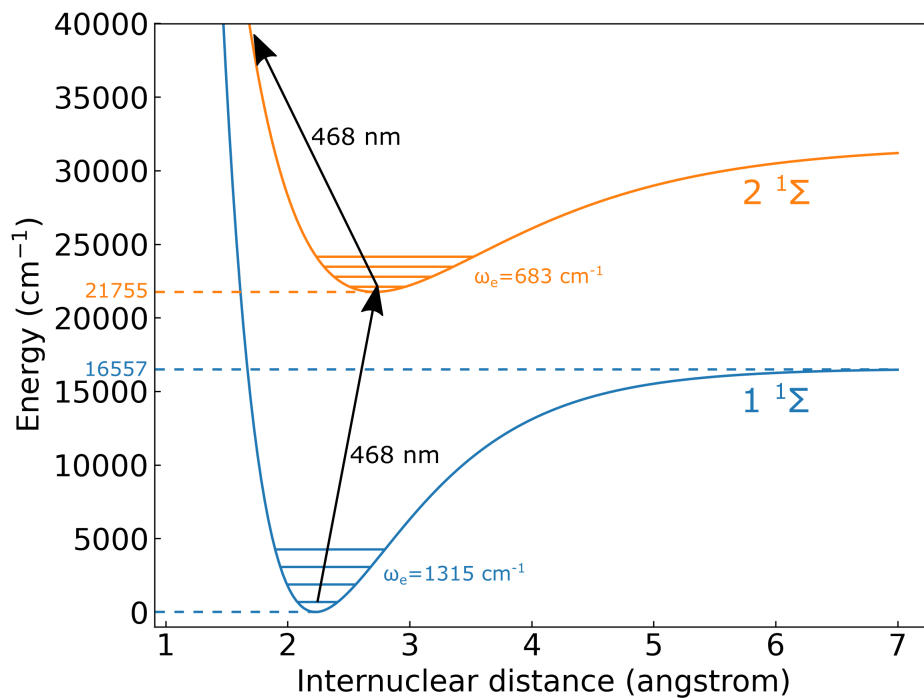


Figure 11.6: Possible photodissociation scheme of $^{226}$RaH$^+$. All spectroscopic constants are calculated by [189], and the potential energy curves are approximated using the Morse potential.

To test photodissociation, we could reduce the Ra$^+$ cooling laser power when leaking in H$_2$ or D$_2$. However, this will also reduce the population in the $P_{1/2}$ state and make short-lived dark ion events even scarcer. We plan to test reaction with H$_2$ and D$_2$ again with $^{224}$Ra$^+$ and $^{225}$Ra$^+$. The large isotope shift in both the molecular ion and the radium ion may help reduce the photodissociation rate if this is indeed the issue.

# Chapter 12

# Towards a hadronic $CP$ violation measurement

As discussed in Section 4.2.4, radioactive polyatomic molecular ions such as RaOH$^+$, RaOCH$_3^+$, RaSH$^+$, and corresponding protactinium-containing molecules are promising for hadronic $CP$ violation measurements. These molecular ions are diamagnetic systems that do not have optical cycling transitions for laser cooling and state detection, so we plan to use quantum logic spectroscopy to prepare and readout the molecular ion state via a radium ion. We consider measurements of the radium nuclear Schiff moment in $^{225}$Ra-containing molecular ions in this section for simplicity, and the techniques discussed in this chapter is generally applicable to other molecular ions too.

The Schiff moment can only be measured with an asymmetry in the electron wavefunction in the nucleus, see Eq. 4.6. Polar molecules provide this asymmetry by ionic or polar covalent bonds, where an electron is fully or partially transferred from an atom to another atom. However, the parity is always a good quantum number for a state without perturbation [1], so the electron wavefunction asymmetry in unperturbed molecules is not

---

[1]Weak interaction does create states where parity is not a good quantum number. The electromag-

helpful in a measurement that happens in the lab-frame: A state with good parity is an equal superposition of the molecule orientation pointing up and down in the lab frame so the wavefunction asymmetry cancels. An external field is needed to break the good parity states so the molecule orientation is quantized by the external field. Therefore, the Schiff moment measurements need to be done in closely-spaced opposite-parity doublets where a reasonable-sized lab-frame electric field can fully polarize the molecules to use the full sensitivity provided by the electron wavefunction asymmetry.

I would like to thank Phelan Yu from Caltech and John Bohn from JILA for their help in my theoretical understanding of the molecules and the molecular structure calculation code they generously shared [200, 201].

## 12.1   Science states of radium-containing molecules

Most of the candidate molecules for hadronic $CP$ violation measurement have zero valence electrons. These molecules have relatively simple electronic states for both experiments and theoretical calculations. A radium atom has two valence electrons in the $7s$ orbital and therefore all simple radium-containing molecular ions must have zero valence electrons, one removed from ionization and the other used in chemical bonding. Such a diamagnetic system provides experimental advantages such as reduced sensitivity to magnetic field fluctuations, but does not provide enough electron spin to create the $\Omega$-doublets that many molecular EDM experiments rely on [70, 72]. On the other hand, polyatomic molecules have vibrational or rotational degree of freedom that is coupled with parity, which produces $l$- and $K$-doublets [86, 87]. Such doublet states in polyatomic molecules are independent of the electronic structure, and can be used to polarize

---

netic interactions between the nucleus and the electrons dominate the weak interaction, and therefore the states have approximately good parity quantum numbers. This is related to another topic in precision measurement about parity non-conservation effects in atoms and molecules [199, 128].

the molecule for a Schiff moment measurement.

We first discuss linear polyatomic molecules such as $RaOH^+$. The "bending" vibrational modes of these molecules allow bending in either of the two directions perpendicular to the molecular symmetry axis [86]. With no external electric field, each eigenstate of the system is a superposition of the two bending directions, so the molecule is effectively rotating clockwise or counterclockwise around the symmetry axis [86, 202]. The two eigenstates, $|\mu_2^{+l}\rangle \pm |\mu_2^{-l}\rangle$, are split by the Coriolis force from other molecular angular momenta, where $\mu_2$ is the bending mode vibrational number, and $l$ is the bending mode angular momentum around the symmetry axis. The splitting in this so-called $l$-doublet in the lowest vibrational excited state $\mu_2 = 1$ of $RaOH^+$ is $\sim 10$ MHz, which can be polarized with an external electric field of $\sim 100$ V/m [86]. However, the lifetime of the excited vibrational state is only $\sim 1$ s [86], which limits the coherence time [72, 90].

The symmetric-top ($RaOCH_3^+$) or asymmetric-top ($RaSH^+$) molecules have similar parity doublets in rotational excited states that enable measuring the Schiff moment in the vibrational ground state to increase the science state lifetime. The molecular frame projection, $K$, of the rotational quantum number around a symmetry axis, $N$, interacts with other angular momentum in the system to form parity doublets in the excited rotational states, similar to the $l$-doublets in excited vibrational states [87]. We consider using the lowest rotational state with $K$-doublets, $N = |K| = 1$, as the science state. The science state is hundreds of GHz above the ground state and the $K$-doublet splitting is $\sim 100$ Hz for $RaOCH_3^+$ [87] and $\sim 20$ MHz for $RaSH^+$ [200]. The radiative lifetime of the science state is $> 1$ h [87], and black-body excitation rate from the science state to other states is tens of minutes in a cryogenic environment [87], and it seems promising to reach $\sim 100$ or $\sim 1000$ s coherence time with these symmetric-top or asymmetric-top molecules with magnetic field shielding and stabilization [4].

## 12.1.1 Hyperfine structure

The three molecular ions discussed here, $^{225}$RaOH$^+$, $^{225}$RaOCH$_3^+$, and $^{225}$RaSH$^+$, have similar science state hyperfine structure. The $N = |K| = 1$ ($\mu_2 = |l| = 1$ for RaOH$^+$) state can be described with the following quantum numbers:

- $m_{I_{\mathrm{Ra}}} = \pm 1/2$, the lab-frame projection of the radium nuclear spin.

- $m_{I_{\mathrm{H}}} = \pm 1/2$, the lab-frame projection of the hydrogen nuclear spin. For RaOCH$_3^+$, the nuclear and rotational wavefunction symmetry only allows the ortho nuclear spin isomer state [87] in the science state so the total hydrogen nuclear spin $I_{\mathrm{H}}$ is 1/2.

- $K$ ($l$)$= \pm 1$, the molecular-frame projection of the rotational (vibrational) quantum number.

- $m_N(m_{\mu_2}) = \pm 1$ or $0$, the lab-frame projection of the rotational (vibrational) quantum number.

The combination of these quantum numbers gives 24 Zeeman states in the rotational (RaOCH$_3^+$, RaSH$^+$) or vibrational doublet (RaOH$^+$) split by spin-spin and spin-rotational interaction respectively. Due to the analogy in the rotational and vibrational doublets, we discuss the hyperfine structure in terms of the $K$-doublet of RaSH$^+$, but the results are generally applicable to all three molecular ions.

The following hyperfine structure calculations are based on Yu's code [200]. We define $F_{\mathrm{Ra}} = N + I_{\mathrm{Ra}}$ and the total angular momentum $F = F_{\mathrm{Ra}} + I_{\mathrm{H}}$. The zero-field hyperfine structure of RaSH$^+$ is shown in Fig. 12.1. In this case, any Zeeman state in the upper and lower manifolds is an equal superposition of $K = \pm 1$, so molecule polarization is not defined in any state, so the states have no Schiff moment sensitivity.
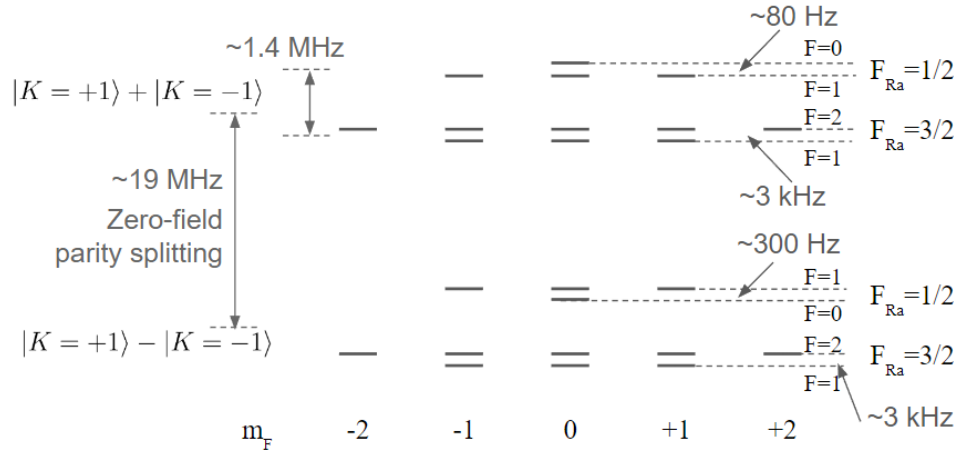
Figure 12.1: The hyperfine and Zeeman structures in the $N = |K| = 1$ state of RaSH$^+$ with no external electric field. The upper and lower parts of the parity doublet are split by $\sim 19$ MHz.

An external electric field is necessary to mix the parity doublet so the $K$ quantum numbers for some states are well-defined. The Stark shift due to the electric field must be much greater than the zero-field splitting of $\sim 19$ MHz for full polarization of the molecular ion. For example, the RaSH$^+$ hyperfine structure at an electric field of 100 V/cm is shown in Fig. 12.2. The Zeeman states in the upper and lower manifolds that have opposite $m_F$ quantum number allow us to isolate the energy shift due to the Schiff moment. For example, the frequency difference between the states $a$ and $b$ (and $a'$ and $b'$) in Fig. 12.2 cancels the Stark shift, but is sensitive to the Zeeman shift and the Schiff moment. The two pairs of states have the same Zeeman shift direction but opposite Schiff moment sensitivities. Therefore, a comparison of the frequency differences in the two pairs of states could isolate the Schiff moment signal from electric and magnetic field fluctuations.
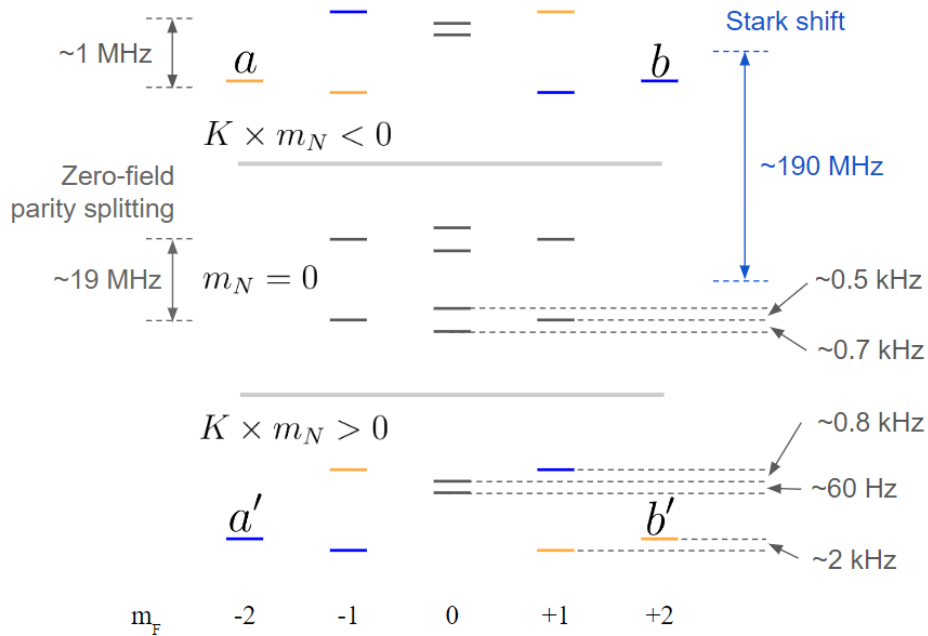
Figure 12.2: The hyperfine and Zeeman structures in the $N = |K| = 1$ state of RaSH$^+$ when the molecule is fully polarized (external electric field $E = 100$ V/m). A small magnetic field is needed to split the Zeeman states with the opposite $m_F$ signs. The Zeeman states with $m_N \neq 0$ and $m_F \neq 0$ have well-defined radium nuclear spin orientation in the molecule and well-defined molecular orientation in the lab frame, and they have an equal magnitude of Schiff moment sensitivity. These states are shown in blue and yellow in the figure, where the different colors indicate opposite Schiff moment sensitivity signs. Two pairs of Zeeman states with opposite Schiff moment sensitivities in the upper and lower Stark manifolds are labeled as $a$, $b$, and $a'$, $b'$.

## 12.1.2   Rotating frame coupling

We consider measuring $CP$ violating moments with molecular ions which requires rotating electric fields to polarize the molecules. If a static electric field is applied to the ions, they will accelerate and could not be trapped. An eEDM experiment has demonstrated dynamic polarization of molecular ions using a rotating electric field in the radial plane of a linear Paul trap with a magnetic field that is effectively co-rotating with the electric field [71]. We can apply similar techniques to Schiff moment measurements. By using a rotating electric field to polarize the molecules, the experiment is effectively done in a rotating frame where the inertial force could interact with the hyperfine and Zeeman structures [203, 204, 205]. With the assumption that the polarization of the molecule is always perpendicular to the rotating axis, the rotating frame dressed Hamiltonian of the molecule is [203, 201]

$$H_{\mathrm{dressed}} = H + \omega_{\mathrm{rot}} F_x, \tag{12.1}$$

where $H$ is the Hamiltonian in the stationary frame, $\omega_{\mathrm{rot}} = 2\pi \times f_{\mathrm{rot}}$ is the angular frequency of the rotating electric field, $F_x$ is the $x$-component of the total angular momentum of the molecule. Conceptually, for two states with $|\Delta m_F| = 1$, if the energy difference of the two states in the stationary frames, see Fig. 12.2, is smaller than the rotating frequency $f_{\mathrm{rot}}$, the two states are mixed together in the rotating frame. Higher order effects also mix states with $m_F = \pm 1$ or $m_F = \pm 2$ to create the avoided crossings discussed in [204, 205]. For example, the states $a$ and $b$ in Fig. 12.2 are fully mixed in the rotating frame by the $\Delta m_F$-th order coupling forces, and a magnetic field is necessary to split the two states to gain Schiff moment sensitivities. Such rotating-frame induced coupling imposes design requirements on the experiment that we will discuss later.

The hyperfine splittings in the $\mathrm{RaOCH_3^+}$ molecular ion are smaller than those in

RaSH$^+$, and therefore the rotating frame coupling effect is larger in RaOCH$_3^+$ at the same rotating electric field frequency.

## 12.2 Quantum logic spectroscopy

Quantum logic spectroscopy (QLS) allows us to prepare and readout a single quantum state of a molecular ion with near unity efficiency [16, 89]. This technique is especially synergistic with radioactive molecules, enabling use of a single radioactive molecular ion for repeated measurements with long coherence times. We discuss the QLS technique in Section 5.4. To realize QLS, we need to create a quantum logic gate between the radioactive molecular ion and a radium ion via a shared motional mode of the two ions in the trap. For high fidelity gate operation over this shared motional mode, the secular frequency of the mode needs to be $\sim$ 1 MHz or larger [16, 161]. A smaller secular frequency slows down the gate operation which gives time for decohercing effects, e.g. trap heating, and makes off-resonant couplings with the carrier transition more likely. Typically an axial motional mode is used for QLS due to the lower heating rate on these motional modes, and the radial secular frequencies need to be similar or higher so the ion crystal is stable in the axially aligned configuration. This configuration reduces the impact from micromotion as the two ions are sitting along the rf null of the trap. This lower limit on the radial secular frequencies imposed by QLS affects the design of a potential Schiff moment experiment.

## 12.3    Experimental realizations

### 12.3.1    JILA eEDM technique

If we follow the approach of [71] where a rotating electric field in the radial plane of the ion trap is applied, the radial secular frequencies of the ions must be much smaller than the Stark shift of the polarizing electric field to be effective [204]. Otherwise, the secular motion is fast enough to follow the rotating motion, and the ion no longer sees a rotating electric field. To demonstrate the effect, consider an extreme case where the rotating electric field has a very small frequency so it is essentially a dc external electric field. This electric field effectively displaces the ions to an equilibrium position where force from the external electric field cancels with the trap pseudopotential, and the total electric field on the ions is the trap rf field at the equilibrium position. Therefore, the polarizing electric field must rotate at a frequency much higher than the typical radial secular frequencies of the ions ($\sim$ 1 MHz). The resulting rotating frequency is much greater than the spin-rotational and spin-dipolar interaction due to the radium nuclear spin ($\sim$ 1 MHz) and mixes the states with opposite sensitivities to the Schiff moment as discussed in the Section 12.1.2.

### 12.3.2    Ring trap

To allow QLS and to avoid mixing states with opposite Schiff moment sensitivities at the same time, we can use a ring-shaped ion trap that is similar to the traps developed in [206, 207, 208]. Compared to a typical linear Paul trap, the radial electrodes of a ring trap are bent into circles, so the trap can confine ions in a donut-shaped volume. A schematic of a 2D ring trap is shown in Fig. 12.3, where the radial electrodes are simplified to the two concentric rings, and the other electrodes provide local confinement
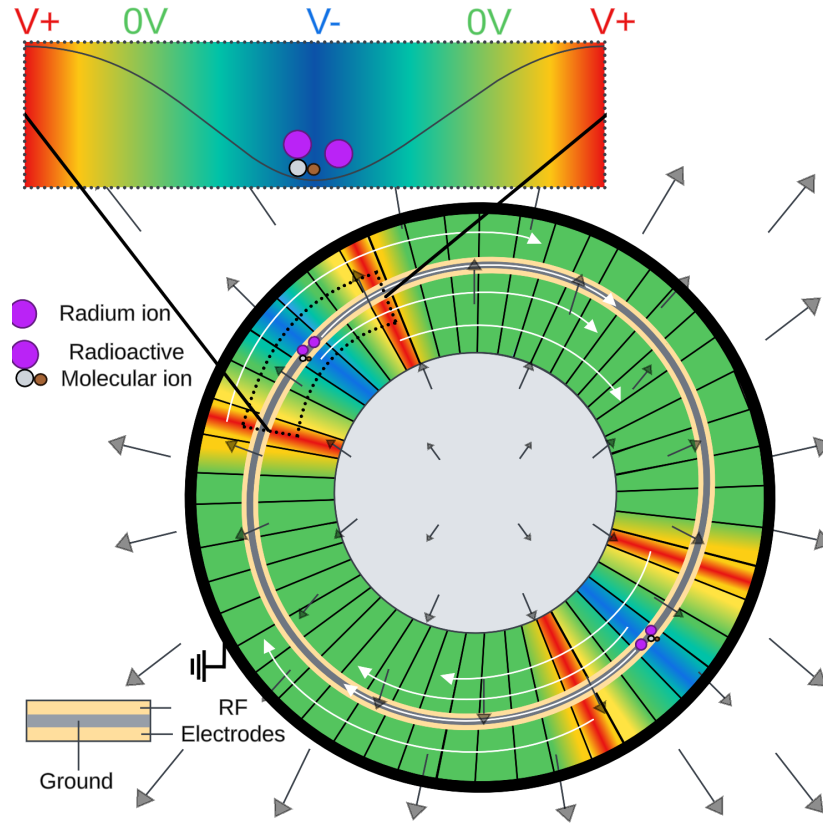
Figure 12.3: Schematic of a ring trap for a molecular ion hadronic $CP$ violation measurement. It has two trapping regions with a radium ion and a radioactive molecular ion trapped in each of the region. The trapping regions rotate around the trap center by changing the electrode voltages. A quadrupole magnetic field is used to split the symmetric Zeeman states coupled by the rotating frame. The directions and magnitudes of the magnetic field in the trap plane are shown as the gray arrows. This figure, inspired by [209], is authored by Spencer Kofford and is reproduced with permission

and can accelerate the ions along the ring. The ions can be locally confined by a potential well formed by voltages on the electrodes, and the potential well can rotate around the ring. We can first trap the $RaSH^+$ and $Ra^+$ in a potential well, and rotate the trapping region around the trap. A dc bias voltage can be applied between the rf ring electrodes to provide a constant electric field that both provides the centripetal force and polarizes the ions. A similar scheme was also recently proposed in [209].

As we need the ring trap to support QLS, the ring spacing needs to be similar to

other ion traps ($\sim 0.5$ mm) that provides $\sim 1$ MHz secular frequencies with a reasonable voltage $< 1000$ V. The ring radius is determined by the rotating frequency and the polarizing electric field. For example, a 1 cm ring radius with 100 kHz rotational frequency corresponds to a 100 V/cm electric field that can fully polarize RaSH$^+$. The rotating frequency will fully mix $|\Delta m_F| = 1$ Zeeman states with the opposite hydrogen nuclear spins which are split by $\sim 1$ kHz, but the mixed states still have the same sensitivity to the Schiff moment. Higher order effects mix the states with opposite $m_F$ quantum numbers, but a co-rotating magnetic field of $> 0.1$ mG can split these states [201, 200]. The co-rotating magnetic field could be produced by a quadrupole magnetic field from anti-Helmholtz coils [71]. Switching RaSH$^+$ to RaOCH$_3^+$ allows using a smaller trap radius or a smaller rotating frequency to polarize the molecular ions to reduce the technical difficulties with trap fabrication and trap drive electronics.

The Schiff moment can be measured by the energy differences between the states with opposite sensitivities to the Schiff moment. A Ramsey sequence between the two states is usually employed [71, 72], which requires preparing an equal superposition of the two states. Similar to other molecular EDM experiments, there are several reversal knobs for testing systematic effects, including measuring in different internal states and opposite quadrupole magnetic field directions.

However, there is a challenge associated with this ring trap technique. We would need to conduct QLS in the rotating frame to prepare the states in the rotating frame. This is a challenging task as the rotating ions move in the ring trap at a speed of several km/s, and rotating electric field noise heating of the motional modes may reduce the fidelity of the gate. Certain RaOCH$_3^+$ states are polarized with $\sim 1$ mV/cm of electric field which may reduce the difficulty. It may also be possible to prepare the state in the stationary frame which is adiabatically or diabatically transferred to desired states in the rotating frame [209, 205], but the hyperfine structure of the considered polyatomic molecular ions

complicates such operations.

### 12.3.3 Optical dipole trap

Optical dipole traps (ODTs) are often used in EDM measurements with neutral laser-cooled species [52, 210], and we discuss whether the optical dipole traps are applicable for trapped ions. Confining an ion with an optical dipole trap is demonstrated in [211], and is realized with an off-resonant light in [212]. For an EDM experiment, off-resonant light could produce a local trapping region that has both high enough secular frequency for QLS and can compensate the Coulomb force on the ion due to the external electric field.

However, optical dipole traps typically cannot confine charged species for a long time. We can consider a hybrid trap that is composed of both an ion trap and an ODT. The ion trap provides long-term stability of the ions that can be measured over days. Assuming the ODT is formed by a perfect Gaussian beam, we need $\sim 10$ W of 1064 nm power focused to a beam waist of $\sim 5$ $\mu$m to provide a sufficient dipole force to compensate the Coulomb force from a 1 mV/cm electric field that can polarize stretch states in $RaOCH_3^+$. For $l$-doublets or $K$-doublets based on asymmetric top molecules which have larger zero-field doublet splittings, the maximum Coulomb force that a reasonable optical dipole trap can compensate is not enough for polarization.

The off-resonant scattering rate from the ODT is estimated to be $\sim 1$ Hz. This would limit the coherence time of the experiment to $\sim 1$ s. This could allow a proof-of-principle measurement with radioactive molecular ions, but is probably not sufficient to realize order of magnitudes gain in hadronic $CP$ violation sensitivities compared to existing measurements [4, 3].

## 12.4    Conclusion

This section discusses technical details of the proposed hadronic $CP$ violation measurements with radioactive molecular ions. Several experimental schemes are described with potential difficulties. Future work is needed to solve these problems or to develop new measurement schemes.

# Chapter 13

# Development of a long-term source for short-lived radium isotopes

All radium ion work introduced so far is based on $^{226}$Ra$^+$, which is a naturally occurring radium isotope with a 1600 year half life. However, for hadronic $CP$ violation measurements, we need to use an isotope with an nonzero nuclear spin. Both $^{225}$Ra ($I = 1/2$) and $^{223}$Ra ($I = 3/2$) have closely-spaced nuclear parity doublets that enhance the Schiff moment and half-lives of $\sim 10$ days, so they are suitable choices for hadronic $CP$ violation measurements [53, 213].

We plan to use $^{225}$Ra, which has a half life of 15 days. $^{225}$Ra$^+$ has a nuclear spin of 1/2, leading to hyperfine structures with simple state preparation and readout techniques [58]. It is also synergistic with our other projects including a radium-225 ion optical clock [61]. However, the short half-life compared to $^{226}$Ra makes using a direct source of $^{225}$Ra difficult. A typical precision measurement takes months or years to finish, while in this period the number of $^{225}$Ra atoms decays to a small fraction of the initial value. Therefore, we desire a long-term source that continuously generates radium-225 atoms in the vacuum chamber.

## 13.1    Tests of a thorium-228 oven

The parent isotope of radium-225, thorium-229, has a half life of 7917 years [214], and it can serve as a long term source for radium-225 that replenishes approximately every half life of radium-225. Previous works on radioactive atom sources from the parent isotopes include [215, 216]. Specifically, a thorium-229 oven was used in [216] for spectroscopy of neutral $^{225}$Ra atoms. This oven contains 10 $\mu$Ci (50 $\mu$g) of thorium-229 nitrate, $\sim$ 50 mg of BaCO$_3$ together with fine grain zirconium powder. The oven is heated to $\sim$ 900 K [216], where the vapor pressure of radium is high enough for releasing radium atoms from the surface while the vapor pressure of thorium is negligibly low. With every week of $^{225}$Ra accumulation, the oven can produce radium atom flux for $\sim$ 1 hour [217].

Our radium source uses the same principle as [216]. Since the supply of thorium-229 is scarce, we use thorium-228 (1.9 year half life) which decays to radium-224 (3.6 day half life) for testing. We tested custom-designed ovens including 3D-printed titanium ovens and homemade tantalum-wire heated ovens [61], but these ovens cannot reach the target temperature reliably. The 3D printed titanium ovens has a resistance $\ll$ 1 ohm, and requires a current of $\sim$ 10 A (30 W power) to reach $\sim$ 700 K. Applying higher currents will exceed the current limit of the vacuum feedthrough flange [1] that is used. The homemade tantalum-wire heated ovens require disassembling the oven when changing the crucible that contains the thorium source. The tantalum wire becomes brittle after heating and almost always breaks when we try to replace the crucible, which makes testing different thorium compounds and reducing agents for radium difficult.

Therefore, we use a commercially-available molecular beam epitaxy (MBE) oven [2] that contains a heated effusion cell and a replaceable crucible. The effusion cell is designed

---

[1]Accuglass 110630.
[2]E-science hot lip effusion cell.

to operate in ultra high vacuum (UHV) environments reliably to higher than 1000 °C, and it has a hot lip at the crucible top to make sure that the entire crucible is heated. The effusion cell also has an integrated type C thermocouple for monitoring its temperature. The crucibles of these ovens can be easily replaced to test different sources. The end of the crucible is a 12.7 mm long, 2 mm diameter aperture for atomic beam collimation.

We dried 40 $\mu$Ci of thorium-228 nitrate solution in the crucible, and added $\sim$ 10 mg Zr powder and $\sim$ 1 mg Sr powder. We receive the Zr powder as suspended in water and we dry a small amount of Zr powder under a heat lamp before adding it into the oven. After adding the Sr powder in, the crucible is quickly installed on the effusion cell, the entire oven is mounted on a testing vacuum chamber, and a turbo pump connecting to the chamber is immediately started to pump down the chamber. These steps need to be done quickly to prevent strontium oxidization in air.

### 13.1.1   Neutral radium detection

The vacuum chamber for oven testing is shown in Fig. 13.1. The laser beam diameter is approximately equal to the camera's field of view ($\sim$ 2 mm), and the PMT collection and detection efficiency of fluorescence photons from the field of view is $\sim$ 0.1%. The end of the crucible aperture is approximately 20 mm to the detection region. A turbo pump maintains the pressure of the chamber to less than $< 10^{-5}$ torr.

We wait for $\sim$ 4 days for radium atoms to accumulate in the oven, and then heat the MBE oven. Between 800 K to 900 K we saw fluorescence on the $^1S_0 \rightarrow {}^1P_1$ transition from the neutral radium atoms produced by the oven, and we confirmed the fluorescence by scanning the 483 nm laser frequency to conduct a spectroscopy (See Fig. 13.2). Although the measurement is not Doppler-free and is not measured against a reliable absolute frequency standard, this measurement determines the approximate transition
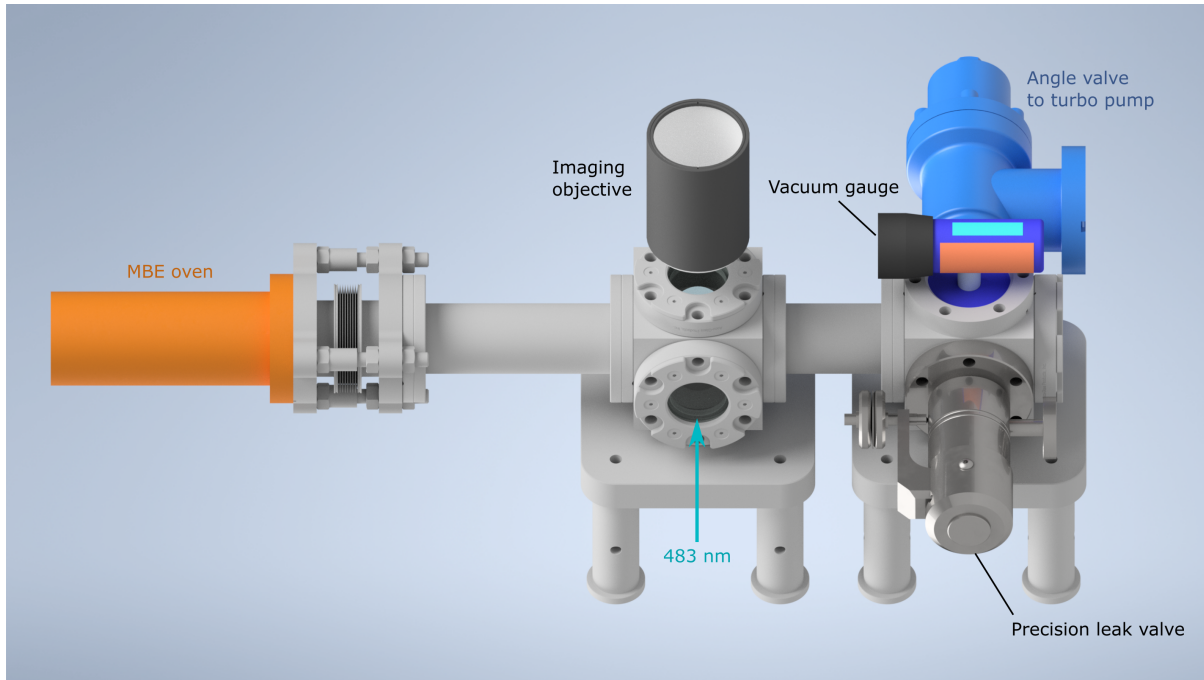
Figure 13.1: The vacuum chamber for $^{224}$Ra oven testing. The MBE oven (orange) extends in the vacuum chamber approximately to the edge of the viewport that the 483 nm laser enters. The electric connectors of the MBE oven are not shown in detail. The 483 nm laser drives the neutral radium $^1S_0 \rightarrow {}^1P_1$ transition, and the fluorescence light is collected via a homemade objective (See Chapter 6) to a PMT and a camera. A precision leak valve (MDC 315012) is available for optionally leaking in helium or argon buffer gas to slow down the recoiled radium atoms from the thorium decay [218] to prevent the atoms from embedding too deep into the crucible wall. A vacuum gauge (Kurt J Lesker KJL275238) is used to monitor the buffer gas pressure. The chamber is supported by two stainless steel base plates which are connected to Thorlabs 1-inch pedestal posts.
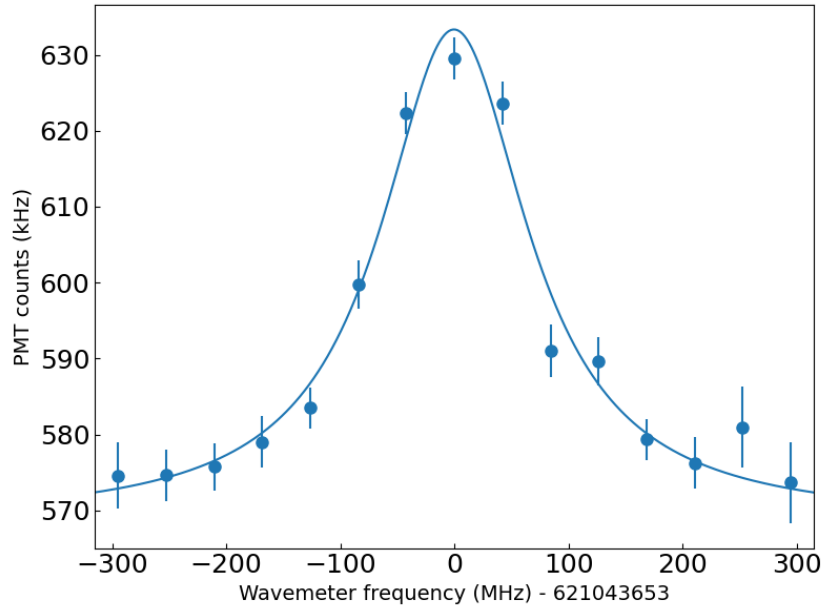
Figure 13.2: The spectrum of the $^{224}$Ra $^1S_0 \to {}^1P_1$ transition at an oven temperature $\sim 900$ K. The frequency is measured with a wavemeter. The solid curve is the data fitted to a Lorentzian function, which gives a center frequency of 0(3) MHz and a Doppler-broadened linewidth of 158(14) MHz.

frequency on our wavemeter and allows testing photoionization of the radium atoms in an ion trap. We are working on a Doppler-free spectroscopy setup with a Te$_2$ absolute frequency reference cell to measure the absolute transition frequency of this transition. This frequency measurement can be compared with the spectroscopy of the corresponding transition in $^{225}$Ra [217, 219] and isotope shift measurements [44].

We repeated the tests of neutral fluorescence a total of five times and found that the magnitude of the fluorescence decreases for following tests despite waiting a similar amount of time between tests. Fig. 13.2 is taken during the third test of the oven. We think the decreases may be related to strontium evaporation loss every time we run the oven, so there is less strontium available in the crucible to reduce the radium compounds formed with either residual gas or other compounds in the crucible.

## 13.1.2   Trapping and cooling of $^{224}$Ra$^+$

After the five neutral fluorescence tests, we moved the radium oven from the testing chamber to the ion trap chamber described in Chapter 6. We also refilled Sr in the crucible to increase the radium atom flux in the following tests for ion trapping. The previously added Sr and Zr that remain in the crucible were not removed. The oven aperture is $\sim 35$ mm from the ion trap. We use 483 nm ($^1S_0 \rightarrow^1 P_1$) and 450 nm ($^1P_1$ to above continuum) lasers for photoionization of radium atoms in the trap. Approximately 1 mW power from each of the laser goes through the end cap electrodes of the ion trap with a $\sim 1$ mm beam diameter. The frequencies of the 468 nm (cooling) and 1079 nm (repumping) lasers for $^{224}$Ra$^+$ are calculated according to Table 9.1, isotope shift measurements [44], and a King plot analysis.

Similar to the neutral radium fluorescence tests, we let radium accumulate in the oven for $\sim 4$ days before running the oven. In the meantime, the trap is calibrated and optimized with Sr$^+$ ions. During run 1 of the thorium-228 oven, we did not see fluorescence from Ra$^+$ ions due to a pressure problem. The absorbed water on the radium oven and other vacuum parts limit the vacuum pressure to $\gtrsim 10^{-7}$ torr when the oven is $\sim 800$ K. At this pressure, the heating rate and reaction rate is too high to laser cool $^{224}$Ra$^+$ in our trap. We heated the oven at $\sim 500$ K for several hours after this run to remove the water absorbed on the oven.

During run 2, the pressure is lower ($10^{-7}$ torr) when the oven is heated to $\sim 850$ K where we observed a fluorescence signal from $^{224}$Ra$^+$. The counts from the radium ions are distinguished from the background by turning off the repumping laser, see Fig. 13.3. The fluorescence lasted for $\sim 200$ s and after that we have not trapped and cooled Ra$^+$. The collision rate is too high and the fluorescence did not last long enough, so we were not able to crystalize Ra$^+$.
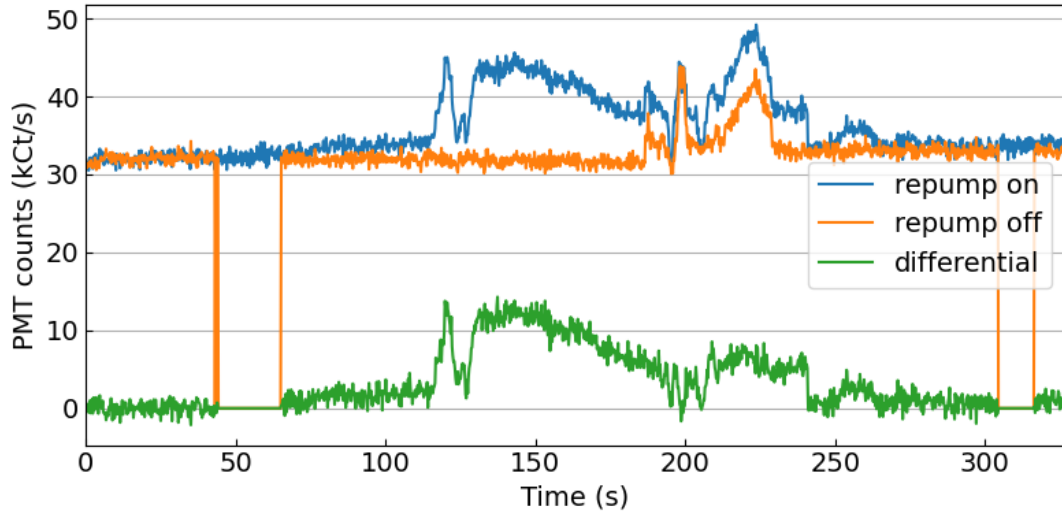
Figure 13.3: Fluorescence signal of the $^{224}$Ra$^+$ $S_{1/2} \rightarrow P_{1/2}$ transition when we trapped and laser-cooled radium ions for the first time. The repumping laser is either always on (when repump off and differential counts are both zero), or switched between on and off with a 200 ms period. The differential signal of PMT counts between repumping laser on and off gives the net photons counts from the radium ions. The background (repump off counts) is from scattered laser photons on trap electrodes.

After run 2, runs 3, 4, and 5 never produced laser-cooled radium ions at temperatures up to $\sim 950$ K. However, we may have been using incorrect 483 nm frequency for these tests, so they are not conclusive. At the highest temperatures of these runs, the vapor pressure of metallic strontium is $\sim 0.1$ torr, so we think that nearly all metallic strontium in the crucible should be gone.

To increase the number of radium atoms available in the oven, we waited for 11 days instead of the typical 4 days before run 6. This should increase the number of radium atoms in the oven by approximately a factor of 2. We were able to detect fluorescence at $\sim 700$ K, a lower temperature than the successful run 2. We also detected the possible 483 nm frequency problem during this run, after successful trapping and cooling. The pressure at $\sim 700$ K is $\sim 5 \times 10^{-8}$ torr and we were able to crystallize $^{224}$Ra$^+$ for the first time. We were able to trap ions for $\sim 30$ minutes during this run. As we think that the metallic strontium is depleted in the oven during the previous runs, we think this oven

125

may work long term. i.e. it does not depend on metallic strontium to work.

In order to confirm that the oven could work long-term, we tested the oven again after 7 days. We are able to see fluorescence again in run 7. During this run, we can trap and cool $Ra^+$ at a rate of $\sim 1$ ion per 10 seconds for more than 1 hour at $\sim 680$ K (pressure $\sim 5 \times 10^{-8}$ torr). After that, we slowly decreased the oven temperature and tested the lowest temperature that we could trap radium ions, and we detected $Ra^+$ down to $\sim 620$ K where the trapping rate is $\sim 1$ ion per several minutes. This final run indicates that every week, the oven accumulates enough atoms to produce $\sim 1000$ trapped ions in this trap. During a typical experiment we would only need to load at most one or a few ions per day, so we think this oven is sufficient to be used in this experiment to produce $^{224}Ra^+$. Therefore, we are currently doing a vacuum bake of this vacuum chamber to achieve a lower pressure for working with $^{224}Ra^+$. We think this oven design should work for producing $^{225}Ra^+$ from $^{229}Th$ too.

### 13.1.3  Discussions

In the radium oven testing chamber, we observe that the neutral radium fluorescence decreases with each test. However, we did not seem to see the ion loading rate decreasing when tested in the ion trap chamber. We think this may relate to the difference of pressure in the chamber. In the testing chamber, the pressure is rather high ($\sim 10^{-6}$ torr background, $\sim 10^{-4}$ torr when heated), so the produced radium atoms bond with residual water, oxygen, or nitrogen in the chamber. Therefore, strontium is required to break the chemical bonds in the radium compounds so radium can be released as atoms when heated. However, the amount of strontium in the crucible quickly reduces at the testing temperatures $\sim 900$ K and therefore the oven efficiency decreases over time as the fraction of radium as compounds increases. On the other hand, the pressure in the

ion trap vaccum chamber is low ($5 \times 10^{-9}$ torr background, $\sim 5 \times 10^{-8}$ when heated), so a higher fraction of radium may exist as atoms, which do not need a reducing agent to be released via heating. We anticipate that the pressure will be lower after the vacuum bake, so the oven may perform better. If the pressure is low enough, the reducing agent may not be necessary.

The aspect ratio between the length $l$ and the diameter $d$ of the oven aperture is currently small ($l/d \sim 6$). Our ion trap has a trapping volume with lengths on the scale of $\sim 2$ mm, and the ion trap is 35 mm away from the oven, which has an aspect ratio of 17.5. For a smaller ion trap that is typically used for coherent control of ions, the trapping volume is smaller and the aspect ratio is even larger. As the aperture aspect ratio is smaller than the trap aspect ratio, the collimation of atoms from the oven is not optimal [220]. To deliver a larger fraction of atoms to the trapping volume, we need to increase the aspect ratio of the aperture. The fraction of atoms from the aperture reaching the trapping volume is shown in Fig. 13.4. For the current trap and aperture, approximately 0.4% of the atoms from the aperture reach the trapping volume. With thinner and longer apertures b and c, we can improve the efficiency by $\sim 4$ times. The efficiency gain from a larger aperture aspect ratio is higher for a smaller ion trap such as the vertical brown line in the figure. We anticipate a factor of 9 gain from aperture b, and a factor of 20 gain from aperture c when compared to the current aperture a.

One concern from decreased aperture diameter and increased length may be that the aperture will not be able to provide enough conductance for the pressure in the crucible to be released fast enough. Following [221], we calculated the vacuum conductance for the apertures used in Fig. 13.4 to be $C_{\text{aperture1}} = 60$ mL/s, $C_{\text{aperture2}} = 0.07$ mL/s, and $C_{\text{aperture3}} = 0.02$ mL/s. The internal volume of the current crucible we use is $\sim 4$ mL, so multiple parallel apertures are probably necessary to reduce the pumping time constant of the crucible to 1 to 10 s if either the aperture b or c is used. On the other hand, some
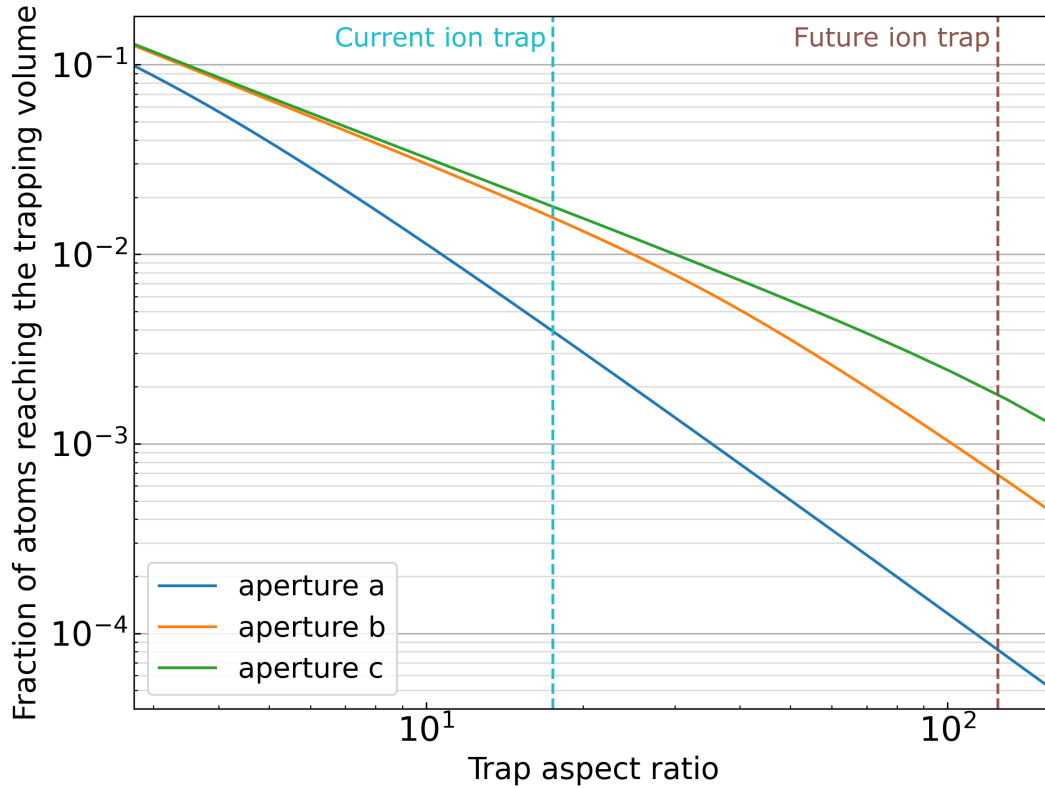
Figure 13.4: Calculated atom number fraction from the oven aperture to the trapping volume for different oven aperture aspect ratios following [220]. Aperture a is the current aperture we use (12.7 mm long, 2 mm diameter). Aperture b is 12.7 mm long and 0.2 mm diameter. Aperture c is 50.8 mm long and 0.2 mm diameter. The aspect ratio of the current trap is shown as the vertical blue line ($\sim 2$ mm trapping volume diameter, 35 mm away from the trap center), and the aspect ratio for a smaller trap (0.4 mm trapping volume diameter, 50 mm away from the trap center) is shown as the vertical brown line.

apertures will be off-centered if multiple apertures are added, so the fraction of atoms reaching the trap center from these apertures is reduced. Different experimental setups may have different optimal aperture diameter, length, and numbers.

An alternative way to produce a collimated atomic beam is using an orthotropic oven [215]. The orthotropic oven relies on surface ionization to produce a neutral atomic beam that has nearly all of the atoms emitted within a small angle. Some of our initial tests of an orthotropic oven is summarized in [61], and we plan to revisit the design starting from a strontium orthotropic oven.

Finally, we plan to test photoionization efficiencies at different wavelengths. Currently, we use a 450 nm laser to excite the atom above continuum from the $^1P_1$ state. We also have 468 nm and 461 nm lasers available that could drive the radium atom to a Rydberg state [43] from the $^1P_1$ state. High ionization rates from these Rydberg states have been reported for calcium [222]. These lasers may increase the ion loading rate with the same neutral radium atom flux.

# Appendix A

# New ion trap for quantum logic spectroscopy

The ion trap used in this thesis is not suitable for quantum logic spectroscopy of molecular ions due to its large dimensions. Therefore, we built an new ion trapping apparatus following the NIST "wheel trap" design [5, 223], which is designed for a quantum logic $Al^+$ ion clock.

A picture of the assembled ion trap is shown in Fig. A.1. The radial rf electrodes are formed by gold plating on a laser-cut diamond wafer with $r_0 = 250$ $\mu$m and a wafer thickness of 500 $\mu$m, connected to vacuum feedthroughs via gold-plated beryllium copper spring clips. The wafer also provides two dc electrodes for micromotion compensation. The axial electrodes are made of titanium and are 4.5 mm from the trap center. All electrodes are mounted on a silver plated oxygen free high thermal conductivity copper post.

The ion trap is housed in a 4.5" CF titanium octagon [1], with 1.33" CF side ports for electrical feedthroughs and laser access. Titanium vacuum parts are used when possible

[1]Kimball Physics MCF450-SphOct-E2A8

Figure A.1: The new "wheel trap" and electrical connections.

to reduce outgassing and improving the magnetic field stability. The vacuum chamber is pumped down with a 50 L/s ion pump [2] and a titanium sublimation pump [3]. The chamber also includes an ion gauge [4] and a computer-controlled precision leak valve [5]. The leak valve allows us to controllably introduce trace amounts of chemicals to produce molecular ions in the trap. After a vacuum bake, the base pressure measured on the ion gauge is $5 \times 10^{-11}$ torr.

We first test trapping $Sr^+$ ion this trap. We use a 3D printed titanium oven [61] mounted on a 1.33" CF side port facing an axial end cap electrode, and the oven design is shown in Fig. A.2. The end cap electrodes have holes at the center to pass the strontium atomic beam to the trap center. The oven tube is loaded with strontium metal, and we pass a current between the oven tube and one of the oven ground pins to

---

[2] Agilent VatIon Plus 55 Starcell, 9191340
[3] Gamma Vacuum 25S-TR-4D-SC-N-TSPA
[4] Agilent UHV-24p
[5] VAT 59024-GEGG-AAP2

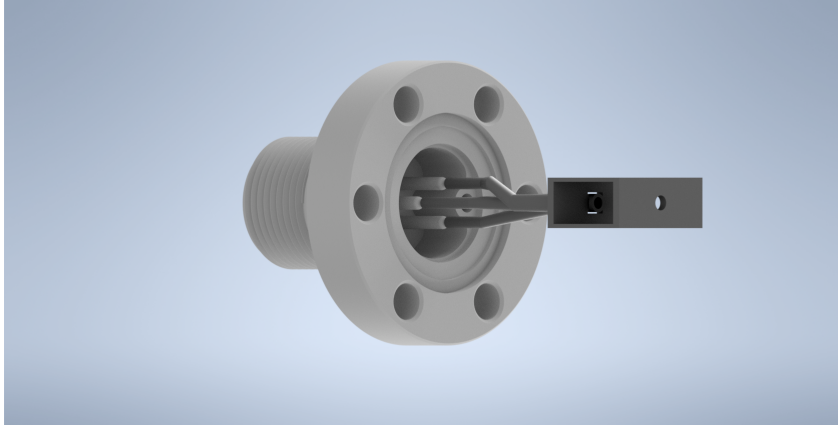heat up the oven to thermally release strontium atoms.



Figure A.2: A 3D printed titanium oven mounted on a vacuum feedthrough (Accuglass 110600). An oven tube is connected to one feedthrough pin (connector is not shown) and it has a loading region that is 1.4 mm diameter and 7 mm deep. The other two feedthrough pins are connected to an oven ground which is in contact with the top of the oven tube to make an electrical connection. The oven ground also has a box-like structure with an aperture to constrain the spread of the strontium atomic beam from the oven tube. This aperture is critical to prevent strontium coating on non-gold-plated parts of the diamond trap wafer to short the electrodes.

The trapped ion fluorescence is collected via a custom objective [6] that compensates for the 4.50" CF viewport glass. The objective has a 50 mm effectively focal length, a numerical aperture of 0.4, and is color-compensated for 422 nm ($Sr^+$ cooling), 468 nm ($Ra^+$ cooling), and 728 nm ($Ra^+$ optical clock for single ion addressing). An aspheric lens at 100 mm [7] focuses the light to an image that is $\sim 2$ times of the size of trapped ions. Another objective [8] and a tube lens [9] provides another 20 times magnification and images the ions on a PMT [10] (70% of the light) and a camera [11] (30% of the light). The distances between the optical elements in the imaging system are optimized with Zemax, and the resolution is simulated to be $\sim 0.6$ $\mu$m at 468 nm with perfect alignments, and

---

[6]Special optics 57-40-50
[7]Thorlabs AL50100G-A
[8]Thorlabs TL10X-2P
[9]Thorlabs TL400-A
[10]Hamamatsu H10682-210
[11]Hamamatsu QUEST Camera

$< 2 \mu$m with tolerances considered. This resolution should be able to resolve a $Ra^+$ and a molecular ion separated by $\sim 4 \mu$m with an axial out-of-phase secular frequency around $2\pi \times 1$ MHz.

The rf electrodes are driven by a homemade LC resonator based on [224]. We wrap 24 gauge bare copper wire on a custom-machined 6.35 mm thick teflon substrate to form a 0.9 uH toroidal inductor. The inductor is connected in series to the capacitor formed by ion trap electrodes (15 pF), and this series RLC circuit is driven from a rf source through an antenna tuner (MFJ-945E) for impedance matching. A Q factor of $\sim 100$ is measured at the resonance frequency of 42.9 MHz.

We have successfully trapped and cooled $Sr^+$ ions in the setup, and we are currently setting up lasers for controlling the $Sr^+$ optical qubit to test quantum logic spectroscopy on $SrH^+$ or $SrD^+$.

# Bibliography

[1] L. Canetti, M. Drewes, and M. Shaposhnikov, *Matter and antimatter in the universe*, *New Journal of Physics* **14** (2012), no. 9 095012.

[2] A. D. Sakharov, *Violation of CP in variance, C asymmetry, and baryon asymmetry of the universe*, *JETP Letters* **5** (1967), no. 1 24–26.

[3] C. Abel, S. Afach, N. J. Ayres, C. A. Baker, G. Ban, G. Bison, K. Bodek, V. Bondar, M. Burghoff, E. Chanel, Z. Chowdhuri, P.-J. Chiu, B. Clement, C. B. Crawford, M. Daum, S. Emmenegger, L. Ferraris-Bouchez, M. Fertl, P. Flaux, B. Franke, A. Fratangelo, P. Geltenbort, K. Green, W. C. Griffith, M. van der Grinten, Z. D. Grujić, P. G. Harris, L. Hayen, W. Heil, R. Henneck, V. Hélaine, N. Hild, Z. Hodge, M. Horras, P. Iaydjiev, S. N. Ivanov, M. Kasprzak, Y. Kermaidic, K. Kirch, A. Knecht, P. Knowles, H.-C. Koch, P. A. Koss, S. Komposch, A. Kozela, A. Kraft, J. Krempel, M. Kuźniak, B. Lauss, T. Lefort, Y. Lemière, A. Leredde, P. Mohanmurthy, A. Mtchedlishvili, M. Musgrave, O. Naviliat-Cuncic, D. Pais, F. M. Piegsa, E. Pierre, G. Pignol, C. Plonka-Spehr, P. N. Prashanth, G. Quéméner, M. Rawlik, D. Rebreyend, I. Rienäcker, D. Ries, S. Roccia, G. Rogel, D. Rozpedzik, A. Schnabel, P. Schmidt-Wellenburg, N. Severijns, D. Shiers, R. Tavakoli Dinani, J. A. Thorne, R. Virot, J. Voigt, A. Weis, E. Wursten, G. Wyszynski, J. Zejma, J. Zenner, and G. Zsigmond, *Measurement of the permanent electric dipole moment of the neutron*, *Phys. Rev. Lett.* **124** (Feb, 2020) 081803.

[4] B. Graner, Y. Chen, E. G. Lindahl, and B. R. Heckel, *Reduced limit on the permanent electric dipole moment of* $^{199}$Hg, *Phys. Rev. Lett.* **116** (Apr., 2016) 161601.

[5] S. M. Brewer, J.-S. Chen, A. M. Hankin, E. R. Clements, C. W. Chou, D. J. Wineland, D. B. Hume, and D. R. Leibrandt, $^{27}$al$^+$ *quantum-logic clock with a systematic uncertainty below* $10^{-18}$, *Phys. Rev. Lett.* **123** (July, 2019) 033201.

[6] M. S. Safronova, D. Budker, D. DeMille, D. F. J. Kimball, A. Derevianko, and C. W. Clark, *Search for new physics with atoms and molecules*, *Rev. Mod. Phys.* **90** (June, 2018) 025008.

134

[7] M. Fan, C. A. Holliman, A. L. Wang, and A. M. Jayich, *Laser cooling of radium ions*, PRL **122** (June, 2019) 223001.

[8] C. A. Holliman, M. Fan, A. Contractor, S. M. Brewer, and A. M. Jayich, *Radium ion optical clock*, PRL **128** (Jan., 2022) 033202.

[9] M. Fan, C. A. Holliman, X. Shi, H. Zhang, M. W. Straus, X. Li, S. W. Buechele, and A. M. Jayich, *Optical mass spectrometry of cold* $RaOH^+$ *and* $RaOCH_3^+$, *Phys. Rev. Lett.* **126** (Jan, 2021) 023002.

[10] H. Park, J. Tallant, X. Zhang, J. Noble, D. Guan, N. Dao, and K. R. Overstreet, *171yb+ microwave clock for military and commercial applications*, in *2020 Joint Conference of the IEEE International Frequency Control Symposium and International Symposium on Applications of Ferroelectrics (IFCS-ISAF)*, pp. 1–4, 2020.

[11] D. J. Berkeland, J. D. Miller, J. C. Bergquist, W. M. Itano, and D. J. Wineland, *Minimization of ion micromotion in a paul trap*, *J. Appl. Phys.* **83** (1998), no. 10 5025–5033.

[12] M. Drewsen and A. Brøner, *Harmonic linear paul trap: Stability diagram and effective potentials*, PRA **62** (Sept., 2000) 045401.

[13] A. Drakoudis, M. Söllner, and G. Werth, *Instabilities of ion motion in a linear paul trap*, *International Journal of Mass Spectrometry* **252** (2006), no. 1 61–68.

[14] K. Deng, H. Che, Y. Lan, Y. P. Ge, Z. T. Xu, W. H. Yuan, J. Zhang, and Z. H. Lu, *Design of blade-shaped-electrode linear ion traps with reduced anharmonic contributions*, *Journal of Applied Physics* **118** (2015), no. 11 113106, [https://doi.org/10.1063/1.4931420].

[15] P. O. Schmidt, T. Rosenband, C. Langer, W. M. Itano, J. C. Bergquist, and D. J. Wineland, *Spectroscopy using quantum logic*, *Science* **309** (July, 2005) 749.

[16] C.-w. Chou, C. Kurz, D. B. Hume, P. N. Plessow, D. R. Leibrandt, and D. Leibfried, *Preparation and coherent manipulation of pure quantum states of a single molecular ion*, *Nature (London)* **545** (May, 2017) 203–207.

[17] J. P. Home, *Chapter 4 - quantum science and metrology with mixed-species ion chains*, in *Advances in Atomic, Molecular, and Optical Physics* (E. Arimondo, P. R. Berman, and C. C. Lin, eds.), vol. 62 of *Advances In Atomic, Molecular, and Optical Physics*, pp. 231–277. Academic Press, 2013.

[18] M. D'Onofrio, Y. Xie, A. J. Rasmusson, E. Wolanski, J. Cui, and P. Richerme, *Radial two-dimensional ion crystals in a linear paul trap*, *Phys. Rev. Lett.* **127** (Jul, 2021) 020503.

[19] S. Fishman, G. De Chiara, T. Calarco, and G. Morigi, *Structural phase transitions in low-dimensional ion crystals*, Phys. Rev. B **77** (Feb, 2008) 064111.

[20] M. Drewsen, C. Brodersen, L. Hornekær, J. S. Hangst, and J. P. Schifffer, *Large ion crystals in a linear paul trap*, Phys. Rev. Lett. **81** (Oct., 1998) 2878–2881.

[21] G. Morigi and H. Walther, *Two-species coulomb chains for quantum information*, The European Physical Journal D - Atomic, Molecular, Optical and Plasma Physics **13** (Jan., 2001) 261–269.

[22] A. K. Ratcliffe, L. M. Oberg, and J. J. Hope, *Micromotion-enhanced fast entangling gates for trapped-ion quantum computing*, Phys. Rev. A **101** (May, 2020) 052332.

[23] A. Bermudez, P. Schindler, T. Monz, R. Blatt, and M. Müller, *Micromotion-enabled improvement of quantum logic gates with trapped ions*, New Journal of Physics **19** (nov, 2017) 113038.

[24] R. Blümel, C. Kappler, W. Quint, and H. Walther, *Chaos and order of laser-cooled ions in a paul trap*, Phys. Rev. A **40** (Jul, 1989) 808–823.

[25] T. Pruttivarasin, M. Ramm, and H. Häffner, *Direct spectroscopy of the $^2S_{1/2} \to\ ^2P_{1/2}$ and $^2D_{3/2} \to\ ^2P_{1/2}$ transitions and observation of micromotion modulated spectra in trapped $^{40}$Ca$^+$*, J. Phys. B **47** (2014), no. 13 135002.

[26] D. J. Wineland, R. E. Drullinger, and F. L. Walls, *Radiation-pressure cooling of bound resonant absorbers*, PRL **40** (June, 1978) 1639–1642.

[27] J. Cao, P. Zhang, J. Shang, K. Cui, J. Yuan, S. Chao, S. Wang, H. Shu, and X. Huang, *A compact, transportable single-ion optical clock with 7.8×1017 systematic uncertainty*, Applied Physics B **123** (Mar., 2017) 112.

[28] P. Dubé, A. A. Madej, A. Shiner, and B. Jian, *$^{88}$Sr$^+$ single-ion optical clock with a stability approaching the quantum projection noise limit*, PRA **92** (Oct., 2015) 042119.

[29] K. J. Arnold, R. Kaewuam, S. R. Chanu, T. R. Tan, Z. Zhang, and M. D. Barrett, *Precision measurements of the $^{138}$Ba$^+$ $6s^2S_{1/2} - 5d^2D_{5/2}$ clock transition*, Phys. Rev. Lett. **124** (May, 2020) 193001.

[30] D. T. C. Allcock, W. C. Campbell, J. Chiaverini, I. L. Chuang, E. R. Hudson, I. D. Moore, A. Ransford, C. Roman, J. M. Sage, and D. J. Wineland, *omg blueprint for trapped ion quantum computing with metastable states*, Applied Physics Letters **119** (2021), no. 21 214002, [https://doi.org/10.1063/5.0069544].

[31] K. Matsubara, U. Tanaka, H. Imajo, S. Urabe, and M. Watanabe, *Laser cooling and isotope-shift measurement of zn+ with 202-nm ultraviolet coherent light*, Applied Physics B **76** (2003), no. 3 209–213.

[32] U. Tanaka, H. Imajo, K. Hayasaka, R. Ohmukai, M. Watanabe, and S. Urabe, *Laser cooling and isotope separation of cd+ ions confined in a linear paul trap*, Opt. Lett. **22** (Sep, 1997) 1353–1355.

[33] D. J. Berkeland, J. D. Miller, J. C. Bergquist, W. M. Itano, and D. J. Wineland, *Laser-cooled mercury ion frequency standard*, Phys. Rev. Lett. **80** (Mar, 1998) 2089–2092.

[34] A. S. Bell, P. Gill, H. A. Klein, A. P. Levick, C. Tamm, and D. Schnier, *Laser cooling of trapped ytterbium ions using a four-level optical-excitation scheme*, Phys. Rev. A **44** (Jul, 1991) R20–R23.

[35] V. Letchumanan, M. A. Wilson, P. Gill, and A. G. Sinclair, *Lifetime measurement of the metastable $4d^2d_{52}$ state in $^{88}Sr^+$ using a single trapped ion*, PRA **72** (July, 2005) 012509.

[36] C. D. Bruzewicz, R. McConnell, J. Stuart, J. M. Sage, and J. Chiaverini, *Dual-species, multi-qubit logic primitives for $Ca^+/Sr^+$ trapped-ion crystals*, npj Quantum Information **5** (Nov., 2019) 102.

[37] R. J. Niffenegger, J. Stuart, C. Sorace-Agaskar, D. Kharas, S. Bramhavar, C. D. Bruzewicz, W. Loh, R. T. Maxson, R. McConnell, D. Reens, G. N. West, J. M. Sage, and J. Chiaverini, *Integrated multi-wavelength control of an ion qubit*, Nature **586** (2020), no. 7830 538–542.

[38] P. Dubé, A. A. Madej, J. E. Bernard, and A. D. Shiner, *High-resolution spectroscopy of the 88Sr+ single ion optical frequency standard*, in *Time and Frequency Metrology* (R. J. Jones, ed.), vol. 6673, p. 667305, International Society for Optics and Photonics, SPIE, 2007.

[39] C. Zhang, S. Buechele, and A. Jayich, *Towards a cryogenic vacuum system for rapid testing of ion traps*, in *APS Division of Atomic, Molecular and Optical Physics Meeting Abstracts*, vol. 2022 of *APS Meeting Abstracts*, p. F01.046, Jan., 2022.

[40] E. Rasmussen, *Serien im funkenspektrum des radiums. ra ii*, Zeitschrift für Physik **86** (Jan, 1933) 24–32.

[41] E. Rasmussen, *Das bogenspektrum des radiums*, Zeitschrift für Physik **87** (1934), no. 9 607–615.

[42] H. N. Russell, *The spectrum and ionization potential of radium, PR* **46** (Dec., 1934) 989–990.

[43] J. A. Armstrong, J. J. Wynne, and F. S. Tomkins, *Bound, 7snp 1p10 series in ra i: measurements and predictions, Journal of Physics B: Atomic and Molecular Physics* **13** (mar, 1980) L133.

[44] K. Wendt, S. A. Ahmad, W. Klempt, R. Neugart, E. W. Otten, and H. H. Stroke, *On the hyperfine structure and isotope shift of radium, Zeitschrift für Physik D Atoms, Molecules and Clusters* **4** (Sept., 1987) 227–241.

[45] W. Neu, R. Neugart, E. W. Otten, G. Passler, K. Wendt, B. Fricke, E. Arnold, H. J. Kluge, and G. Ulm, *Quadrupole moments of radium isotopes from the $7p^2\mathrm{P}_{3/2}$ hyperfine structure in ra ii, Zeitschrift für Physik D Atoms, Molecules and Clusters* **11** (June, 1989) 105–111.

[46] O. O. Versolato, G. S. Giri, L. W. Wansbeek, J. E. van den Berg, D. J. van der Hoek, K. Jungmann, W. L. Kruithof, C. J. G. Onderwater, B. K. Sahoo, B. Santra, P. D. Shidling, R. G. E. Timmermans, L. Willmann, and H. W. Wilschut, *Laser spectroscopy of trapped short-lived* $\mathrm{Ra}^+$ *ions, Phys. Rev. A* **82** (July, 2010) 010501.

[47] O. O. Versolato, L. W. Wansbeek, G. S. Giri, J. E. v. d. Berg, D. J. v. d. Hoek, K. Jungmann, W. L. Kruithof, C. J. G. Onderwater, B. K. Sahoo, B. Santra, P. D. Shidling, R. G. E. Timmermans, L. Willmann, and H. W. Wilschut, *Atomic parity violation in a single trapped radium ion, Hyperfine Interactions* **199** (Apr., 2011) 9.

[48] G. S. Giri, O. O. Versolato, J. E. van den Berg, O. Böll, U. Dammalapati, D. J. van der Hoek, K. Jungmann, W. L. Kruithof, S. Müller, M. Nuñez Portela, C. J. G. Onderwater, B. Santra, R. G. E. Timmermans, L. W. Wansbeek, L. Willmann, and H. W. Wilschut, *Isotope shifts of the $6d^2D_{3/2} \to 7p^2P_{1/2}$ transition in trapped short-lived $^{209-214}\mathrm{Ra}^+$, PRA* **84** (Aug., 2011) 020503(R).

[49] O. Versolato, G. Giri, J. van den Berg, O. Böll, U. Dammalapati, D. van der Hoek, S. Hoekstra, K. Jungmann, W. Kruithof, S. Müller, M. Nuñez Portela, C. Onderwater, B. Santra, R. Timmermans, L. Wansbeek, L. Willmann, and H. Wilschut, *Hyperfine structure of the 6dd3/22 level in trapped short-lived 211,209ra+ ions, Physics Letters A* **375** (2011), no. 35 3130–3133.

[50] M. Nuñez Portela, E. A. Dijck, A. Mohanty, H. Bekker, J. E. van den Berg, G. S. Giri, S. Hoekstra, C. J. G. Onderwater, S. Schlesser, R. G. E. Timmermans, O. O. Versolato, L. Willmann, H. W. Wilschut, and K. Jungmann, $\mathrm{Ra}^+$ *ion trapping: toward an atomic parity violation measurement and an optical clock, Applied Physics B* **114** (Jan., 2014) 173–182.

[51] J. R. Guest, N. D. Scielzo, I. Ahmad, K. Bailey, J. P. Greene, R. J. Holt, Z.-T. Lu, T. P. O'Connor, and D. H. Potterveld, *Laser trapping of* $^{225}$Ra *and* $^{226}$Ra *with repumping by room-temperature blackbody radiation*, PRL **98** (Feb., 2007) 093001.

[52] R. H. Parker, M. R. Dietrich, M. R. Kalita, N. D. Lemke, K. G. Bailey, M. Bishof, J. P. Greene, R. J. Holt, W. Korsch, Z.-T. Lu, P. Mueller, T. P. O'Connor, and J. T. Singh, *First measurement of the atomic electric dipole moment of* $^{225}$Ra, *Phys. Rev. Lett.* **114** (June, 2015) 233002.

[53] M. Bishof, R. H. Parker, K. G. Bailey, J. P. Greene, R. J. Holt, M. R. Kalita, W. Korsch, N. D. Lemke, Z.-T. Lu, P. Mueller, T. P. O'Connor, J. T. Singh, and M. R. Dietrich, *Improved limit on the* $^{225}$Ra *electric dipole moment*, *Phys. Rev. C* **94** (Aug., 2016) 025501.

[54] R. F. Garcia Ruiz, R. Berger, J. Billowes, C. L. Binnersley, M. L. Bissell, A. A. Breier, A. J. Brinson, K. Chrysalidis, T. E. Cocolios, B. S. Cooper, K. T. Flanagan, T. F. Giesen, R. P. de Groote, S. Franchoo, F. P. Gustafsson, T. A. Isaev, Á. Koszorús, G. Neyens, H. A. Perrett, C. M. Ricketts, S. Rothe, L. Schweikhard, A. R. Vernon, K. D. A. Wendt, F. Wienholtz, S. G. Wilkins, and X. F. Yang, *Spectroscopy of short-lived radioactive molecules*, *Nature* **581** (May, 2020) 396–400.

[55] A. A. Sherman, *Translation of an historic paper. on a new, strongly radioactive substance, contained in pitchblende: by m.p. curie, mme p. curie and m.g. bémont; presented by m. becquerel.*, *Journal of nuclear medicine : official publication, Society of Nuclear Medicine* **11** (Jun, 1970) 269–70.

[56] R. Pal, D. Jiang, M. S. Safronova, and U. I. Safronova, *Calculation of parity-nonconserving amplitude and other properties of* ra$^+$, *Phys. Rev. A* **79** (June, 2009) 062505.

[57] N. Auerbach, V. V. Flambaum, and V. Spevak, *Collective t- and p-odd electromagnetic moments in nuclei with octupole deformations*, PRL **76** (June, 1996) 4316–4319.

[58] S. Olmschenk, K. C. Younge, D. L. Moehring, D. N. Matsukevich, P. Maunz, and C. Monroe, *Manipulation and detection of a trapped* Yb$^+$ *hyperfine qubit*, PRA **76** (Nov., 2007) 052314.

[59] R. Islam, E. E. Edwards, K. Kim, S. Korenblit, C. Noh, H. Carmichael, G.-D. Lin, L.-M. Duan, C.-C. Joseph Wang, J. K. Freericks, and C. Monroe, *Onset of a quantum phase transition with a trapped ion quantum simulator*, *Nature Communications* **2** (2011), no. 1 377.

[60] Y. Nam, J.-S. Chen, N. C. Pisenti, K. Wright, C. Delaney, D. Maslov, K. R. Brown, S. Allen, J. M. Amini, J. Apisdorf, K. M. Beck, A. Blinov, V. Chaplin, M. Chmielewski, C. Collins, S. Debnath, K. M. Hudek, A. M. Ducore, M. Keesan, S. M. Kreikemeier, J. Mizrahi, P. Solomon, M. Williams, J. D. Wong-Campos, D. Moehring, C. Monroe, and J. Kim, *Ground-state energy estimation of the water molecule on a trapped-ion quantum computer*, npj Quantum Information **6** (2020), no. 1 33.

[61] C. A. Holliman, *Clocks, Qubits, and Searches for New Physics.* PhD thesis, University of California, Santa Barbara, 2022.

[62] A. Canepa, *Searches for supersymmetry at the large hadron collider*, Reviews in Physics **4** (2019) 100033.

[63] L. I. Schiff, *Measurability of nuclear electric dipole moments*, PR **132** (Dec., 1963) 2194–2200.

[64] E. D. Commins, J. D. Jackson, and D. P. DeMille, *The electric dipole moment of the electron: An intuitive explanation for the evasion of schiff's theorem*, Am. J. Phys. **75** (June, 2007) 532–536.

[65] P. G. H. Sandars, *The electric dipole moment of an atom*, Physics Letters **14** (1965), no. 3 194–196.

[66] B. C. Regan, E. D. Commins, C. J. Schmidt, and D. DeMille, *New limit on the electron electric dipole moment*, Phys. Rev. Lett. **88** (Feb., 2002) 071805.

[67] S. Eckel, P. Hamilton, E. Kirilov, H. W. Smith, and D. DeMille, *Search for the electron electric dipole moment using Ω-doublet levels in pbo*, PRA **87** (May, 2013) 052130.

[68] J. J. Hudson, D. M. Kara, I. J. Smallman, B. E. Sauer, M. R. Tarbutt, and E. A. Hinds, *Improved measurement of the shape of the electron*, Nature **473** (May, 2011) 493.

[69] T. A. C. M. E. Collaboration, J. Baron, W. C. Campbell, D. DeMille, J. M. Doyle, G. Gabrielse, Y. V. Gurevich, P. W. Hess, N. R. Hutzler, E. Kirilov, I. Kozyryev, B. R. O'Leary, C. D. Panda, M. F. Parsons, E. S. Petrik, B. Spaun, A. C. Vutha, and A. D. West, *Order of magnitude smaller limit on the electric dipole moment of the electron*, Science **343** (Jan., 2014) 269–272.

[70] V. Andreev, D. G. Ang, D. DeMille, J. M. Doyle, G. Gabrielse, J. Haefner, N. R. Hutzler, Z. Lasner, C. Meisenhelder, B. R. O'Leary, C. D. Panda, A. D. West, E. P. West, X. Wu, and A. C. M. E. Collaboration, *Improved limit on the electric dipole moment of the electron*, Nature **562** (Oct., 2018) 355–360.

[71] W. B. Cairncross, D. N. Gresh, M. Grau, K. C. Cossel, T. S. Roussy, Y. Ni, Y. Zhou, J. Ye, and E. A. Cornell, *Precision measurement of the electron's electric dipole moment using trapped molecular ions*, Phys. Rev. Lett. **119** (Oct., 2017) 153001.

[72] T. S. Roussy, L. Caldwell, T. Wright, W. B. Cairncross, Y. Shagam, K. B. Ng, N. Schlossberger, S. Y. Park, A. Wang, J. Ye, and E. A. Cornell, *A new bound on the electron's electric dipole moment*, 2022.

[73] M. Pospelov and A. Ritz, *Neutron electric dipole moment from electric and chromoelectric dipole moments of quarks*, Phys. Rev. D **63** (Mar, 2001) 073015.

[74] J. Engel, M. J. Ramsey-Musolf, and U. van Kolck, *Electric dipole moments of nucleons, nuclei, and atoms: The standard model and beyond*, Progress in Particle and Nuclear Physics **71** (July, 2013) 21–74.

[75] V. V. Flambaum and V. A. Dzuba, *Electric dipole moments of atoms and molecules produced by enhanced nuclear schiff moments*, Phys. Rev. A **101** (Apr, 2020) 042504.

[76] V. Spevak, N. Auerbach, and V. V. Flambaum, *Enhanced t-odd, p-odd electromagnetic moments in reflection asymmetric nuclei*, Phys. Rev. C **56** (Sept., 1997) 1357–1369.

[77] R. G. Helmer, M. A. Lee, C. W. Reich, and I. Ahmad, *Intrinsic reflection asymmetry in 225ra: Additional information from a study of the -decay scheme of 229th*, Nuclear Physics A **474** (1987), no. 1 77–113.

[78] J. T. Singh, *A new concept for searching for time-reversal symmetry violation using pa-229 ions trapped in optical crystals*, Hyperfine Interactions **240** (Mar., 2019) 29.

[79] F. Dalton, V. V. Flambaum, and A. J. Mansour, *Enhanced schiff and magnetic quadrupole moments in deformed nuclei and their connection to the search for axion dark matter*, Phys. Rev. C **107** (Mar, 2023) 035502.

[80] J. de Vries, E. Mereghetti, R. G. E. Timmermans, and U. van Kolck, *The effective chiral lagrangian from dimension-six parity and time-reversal violation*, Annals of Physics **338** (2013) 50–96.

[81] M. Pospelov, *Best values for the cp-odd meson-nucleon couplings from supersymmetry*, Physics Letters B **530** (2002), no. 1 123–128.

[82] J. S. M. Ginges and V. V. Flambaum, *Violations of fundamental symmetries in atoms and tests of unification theories of elementary particles*, Physics Reports **397** (July, 2004) 63–154.

[83] T. Chupp and M. Ramsey-Musolf, *Electric dipole moments: A global analysis*, *PRC* **91** (Mar., 2015) 035502.

[84] T. Fleig and M. Jung, *Model-independent determinations of the electron edm and the role of diamagnetic atoms*, *Journal of High Energy Physics* **2018** (2018), no. 7 12.

[85] F.-K. Guo, R. Horsley, U.-G. Meißner, Y. Nakamura, H. Perlt, P. E. L. Rakow, G. Schierholz, A. Schiller, and J. M. Zanotti, *Electric dipole moment of the neutron from 2 + 1 flavor lattice qcd*, *Phys. Rev. Lett.* **115** (Aug, 2015) 062001.

[86] I. Kozyryev and N. R. Hutzler, *Precision measurement of time-reversal symmetry violation with laser-cooled polyatomic molecules*, *Phys. Rev. Lett.* **119** (Sept., 2017) 133002.

[87] P. Yu and N. R. Hutzler, *Probing fundamental symmetries of deformed nuclei in symmetric top molecules*, *Phys. Rev. Lett.* **126** (Jan, 2021) 023003.

[88] R. Mitra, V. S. Prasannaa, B. K. Sahoo, N. R. Hutzler, M. Abe, and B. P. Das, *Study of hgoh to assess its suitability for electron electric dipole moment searches*, *Atoms* **9** (2021), no. 1.

[89] Y. Lin, D. R. Leibrandt, D. Leibfried, and C.-w. Chou, *Quantum entanglement between an atom and a molecule*, *Nature* **581** (May, 2020) 273–277.

[90] P. Wang, C.-Y. Luan, M. Qiao, M. Um, J. Zhang, Y. Wang, X. Yuan, M. Gu, J. Zhang, and K. Kim, *Single ion qubit with estimated coherence time exceeding one hour*, *Nature Communications* **12** (2021), no. 1 233.

[91] V. V. Flambaum, *Enhanced nuclear schiff moment and time-reversal violation in* $^{229}$Th-*containing molecules*, *Phys. Rev. C* **99** (Mar., 2019) 035501.

[92] J.-P. Likforman, V. Tugayé, S. Guibal, and L. Guidoni, *Precision measurement of the branching fractions of the* $5p\,^2p_{1/2}$ *state in* $^{88}$Sr$^+$ *with a single ion in a microfabricated surface trap*, *Phys. Rev. A* **93** (May, 2016) 052507.

[93] D. J. Berkeland and M. G. Boshier, *Destabilization of dark states and optical spectroscopy in zeeman-degenerate atomic systems*, *Phys. Rev. A* **65** (Feb., 2002) 033413.

[94] C. Roos, *Controlling the quantum state of trapped ions*. PhD thesis, University of Innsbruck, 2000.

[95] C. Roos, T. Zeiger, H. Rohde, H. C. Nägerl, J. Eschner, D. Leibfried, F. Schmidt-Kaler, and R. Blatt, *Quantum state engineering on an optical transition and decoherence in a paul trap*, *PRL* **83** (Dec., 1999) 4713–4716.

[96] Y. Yu, N. R. Hutzler, J. T. Zhang, L. R. Liu, J. D. Hood, T. Rosenband, and K.-K. Ni, *Motional-ground-state cooling outside the lamb-dicke regime*, *Phys. Rev. A* **97** (Jun, 2018) 063423.

[97] C. Foot, *Atomic Physics*. Oxford University Press, 2005.

[98] S. A. King, L. J. Spieß, P. Micke, A. Wilzewski, T. Leopold, E. Benkler, R. Lange, N. Huntemann, A. Surzhykov, V. A. Yerokhin, J. R. Crespo López-Urrutia, and P. O. Schmidt, *An optical atomic clock based on a highly charged ion*, *Nature* **611** (2022), no. 7934 43–47.

[99] J. E. Christensen, *High-fidelity operation of a radioactive trapped ion qubit,* $^{133}Ba^+$. PhD thesis, UCLA, 2020.

[100] C. Schneider, S. J. Schowalter, P. Yu, and E. R. Hudson, *Electronics of an ion trap with integrated time-of-flight mass spectrometer*, *Int. J. of Mass Spectrom.* **394** (Jan., 2016) 1–8.

[101] P. Herskind, *Cavity Quantum Electrodynamics with Ion Coulomb Crystals*. PhD thesis, The University of Aarhus, 2008.

[102] M. Brownnutt, V. Letchumanan, G. Wilpers, R. C. Thompson, P. Gill, and A. G. Sinclair, *Controlled photoionization loading of 88sr+ for precision ion-trap experiments*, *Applied Physics B* **87** (2007), no. 3 411–415.

[103] D. Hucul, J. E. Christensen, E. R. Hudson, and W. C. Campbell, *Spectroscopy of a synthetic trapped ion qubit*, *Phys. Rev. Lett.* **119** (Sep, 2017) 100501.

[104] W. Alt, *An objective lens for efficient fluorescence detection of single atoms*, *Optik* **113** (2002), no. 3 142–144.

[105] G. Shu, M. R. Dietrich, N. Kurz, and B. B. Blinov, *Trapped ion imaging with a high numerical aperture spherical mirror*, *Journal of Physics B: Atomic, Molecular and Optical Physics* **42** (jul, 2009) 154005.

[106] D. Hucul, *A Modular Quantum System of Trapped Atomic Ions*. PhD thesis, University of Maryland, 2015.

[107] J. D. Pritchard, J. A. Isaacs, and M. Saffman, *Long working distance objective lenses for single atom trapping and imaging*, *Review of Scientific Instruments* **87** (2016), no. 7 073107, [https://aip.scitation.org/doi/pdf/10.1063/1.4959775].

[108] F. SORRENTINO, G. FERRARI, N. POLI, R. DRULLINGER, and G. M. TINO, *Laser cooling and trapping of atomic strontium for ultracold atoms physics, high-precision spectroscopy and quantum sensors*, *Modern Physics Letters B* **20** (2006), no. 21 1287–1320, [https://doi.org/10.1142/S0217984906011682].

[109] M. Kumph, *2D arrays of ion traps for large scale integration of quantum information processors.* PhD thesis, University of Innsbruck, 2015.

[110] E. D. Black, *An introduction to pound-drever-hall laser frequency stabilization,* *American Journal of Physics* **69** (Jan., 2001) 79–87.

[111] S. T. Sullivan, *The MOTion trap: a hybrid atom-ion trap system for experiments in cold-chemistry and the production of cold polar molecular ions.* PhD thesis, University of California, Los Angeles, 2013.

[112] S. Gerstenkorn, J. Verges, and J. Chevillard, *Atlas du spectre d'absorption de la molecule d'iode: 11000-14000 cm to the minus 1.* Laboratoire Aime-Cotton CNRS II, Paris, 1982.

[113] S. Gerstenkorn and P. Luc, *Atlas du spectre d'absorption de la molecule d'iode: 14000-15600 cm to the minus 1.* Laboratoire Aime-Cotton CNRS II, 1982.

[114] J. Cariou and P. Luc, *Atlas du spectre d'absorption de la molecule de tellure: 18500-21200 cm to the minus 1, temperature: 650 degrees centigrade.* No. pt. 2. Laboratoire Aime-Cotton CNRS II, 1980.

[115] J. Cariou and P. Luc, *Atlas du spectre d'absorption de la molecule de tellure: 21100-23800 cm to the minus 1, temperature: 510 degrees C.* No. pt. 5. Laboratoire Aime-Cotton CNRS II, 1980.

[116] H. Knöckel and E. Tiemann, IodineSpec5 (2011) (Universität Hannover, Hannover, 2011).

[117] H. Knöckel, B. Bodermann, and E. Tiemann, *High precision description of the rovibronic structure of the i2 b-x spectrum*,* *Eur. Phys. J. D* **28** (Feb., 2004) 199–209.

[118] T. Pruttivarasin and H. Katori, *Compact field programmable gate array-based pulse-sequencer and radio-frequency generator for experiments with trapped atoms,* *Rev. Sci. Instrum.* **86** (Nov., 2015) 115106.

[119] "Labrad." `https://github.com/labrad`.

[120] S. Bourdeauducq, R. Jördens, P. Zotov, J. Britton, D. Slichter, D. Leibrandt, D. Allcock, A. Hankin, F. Kermarrec, Y. Sionneau, R. Srinivas, T. R. Tan, and J. Bohnet, *Artiq 1.0*, May, 2016.

[121] M.-A. Bouchiat and C. Bouchiat, *Parity violation in atoms,* *Rep. Prog. Phys.* **60** (1997), no. 11 1351.

[122] M. Dine and A. Kusenko, *Origin of the matter-antimatter asymmetry,* *Rev. Mod. Phys.* **76** (Dec., 2003) 1–30.

[123] J. Dobaczewski and J. Engel, *Nuclear time-reversal violation and the schiff moment of* $^{225}$Ra, *Phys. Rev. Lett.* **94** (June, 2005) 232502.

[124] K. Okada, M. Wada, L. Boesten, T. Nakamura, I. Katayama, and S. Ohtani, *Acceleration of the chemical reaction of trapped* $Ca^+$ *ions with* $H_2O$ *molecules by laser excitation*, *J. Phys. B* **36** (2003), no. 1 33.

[125] T. Yang, A. Li, G. K. Chen, C. Xie, A. G. Suits, W. C. Campbell, H. Guo, and E. R. Hudson, *Optical control of reactions between water and laser-cooled* $Be^+$ *ions*, *J. Phys. Chem. Lett.* **9** (July, 2018) 3555–3560.

[126] R. Noek, G. Vrijsen, D. Gaultney, E. Mount, T. Kim, P. Maunz, and J. Kim, *High speed, high fidelity detection of an atomic hyperfine qubit*, *Opt. Lett.* **38** (Nov., 2013) 4735–4738.

[127] C. Senko, P. Richerme, J. Smith, A. Lee, I. Cohen, A. Retzker, and C. Monroe, *Realization of a quantum integer-spin chain with controllable interactions*, *Phys. Rev. X* **5** (June, 2015) 021026.

[128] N. Fortson, *Possibility of measuring parity nonconservation with a single trapped atomic ion*, *Phys. Rev. Lett.* **70** (Apr., 1993) 2383–2386.

[129] C. Wieman and A. Derevianko, "Atomic parity violation and the standard model."

[130] E. Traykov, U. Dammalapati, S. De, O. C. Dermois, L. Huisman, K. Jungmann, W. Kruithof, A. J. Mol, C. J. G. Onderwater, A. Rogachevskiy, M. da Silva e Silva, M. Sohani, O. Versolato, L. Willmann, and H. W. Wilschut, *Production and trapping of radioactive atoms at the triup facility*, *Nucl. Instrum. Methods Phys. Res., Sec. B* **266** (Oct., 2008) 4532–4536.

[131] M. Ramm, T. Pruttivarasin, M. Kokish, I. Talukdar, and H. Häffner, *Precision measurement method for branching fractions of excited* $P_{1/2}$ *states applied to* $^{40}$Ca$^+$, *Phys. Rev. Lett.* **111** (July, 2013) 023004.

[132] A. Gallagher and A. Lurio, *Optical detection of level crossing in a* $j = \frac{1}{2}$ *state*, *Phys. Rev. Lett.* **10** (Jan, 1963) 25–26.

[133] D. Zimmermann, *Determination of the lifetime of the* $4P_{1/2}$ *state of potassium by hanle-effect*, *Z. Phys. A* **275** (Mar, 1975) 5–10.

[134] See Supplemental Material, available at `https://doi.org/10.1103/PhysRevLett.122.223001`, for further discussion of branching fraction systematic effects and micromotion broadening of the $S_{1/2} \to P_{1/2}$ linescan.

[135] B. K. Sahoo, L. W. Wansbeek, K. Jungmann, and R. G. E. Timmermans, *Light shifts and electric dipole matrix elements in* $Ba^+$ *and* $Ra^+$, *Phys. Rev. A* **79** (May, 2009) 052512.

[136] V. A. Dzuba and V. V. Flambaum, *Calculation of nuclear-spin-dependent parity nonconservation in* $S \rightarrow D$ *transitions of* $Ba^+$, $Yb^+$, *and* $Ra^+$ *ions*, *Phys. Rev. A* **83** (May, 2011) 052513.

[137] L. W. Wansbeek, B. K. Sahoo, R. G. E. Timmermans, K. Jungmann, B. P. Das, and D. Mukherjee, *Atomic parity nonconservation in* $Ra^+$, *Phys. Rev. A* **78** (Nov., 2008) 050501.

[138] B. K. Sahoo, B. P. Das, R. K. Chaudhuri, D. Mukherjee, R. G. E. Timmermans, and K. Jungmann, *Investigations of* $ra^+$ *properties to test possibilities for new optical-frequency standards*, *Phys. Rev. A* **76** (Oct., 2007) 040504.

[139] C. A. Holliman, M. Fan, A. Contractor, M. W. Straus, and A. M. Jayich, *Direct measurement of the* $7s\,^2S_{1/2} \rightarrow 7p\,^2P_{3/2}$ *transition frequency in* $^{226}Ra^+$, *PRA* **102** (Oct., 2020) 042822.

[140] C. A. Holliman, M. Fan, and A. M. Jayich, *Measurements of electric quadrupole transition frequencies in* $^{226}Ra^+$, *PRA* **100** (Dec., 2019) 062512.

[141] M. Fan, C. A. Holliman, A. Contractor, C. Zhang, S. F. Gebretsadken, and A. M. Jayich, *Measurement of the* $Ra^+$ $7p\,^2P_{3/2}$ *state lifetime*, *PRA* **105** (Apr., 2022) 042801.

[142] M. Fan, C. A. Holliman, S. G. Porsev, M. S. Safronova, and A. M. Jayich, *Measurement of the* $7p\,^2P_{3/2}$ *state branching fractions in* $Ra^+$, *PRA* **100** (Dec., 2019) 062504.

[143] S. R. Chanu, V. P. W. Koh, K. J. Arnold, R. Kaewuam, T. R. Tan, Z. Zhang, M. S. Safronova, and M. D. Barrett, *Magic wavelength of the* $^{138}Ba^+$ $6s$ $^2S_{1/2} \rightarrow 5d\,^2D_{5/2}$ *clock transition*, *PRA* **101** (Apr., 2020) 042507.

[144] M. Hettrich, T. Ruster, H. Kaufmann, C. F. Roos, C. T. Schmiegelow, F. Schmidt-Kaler, and U. G. Poschinger, *Measurement of dipole matrix elements with a single trapped ion*, *PRL* **115** (Oct., 2015) 143003.

[145] X.-M. Wu, C.-B. Li, Y.-B. Tang, and T.-Y. Shi, *Magic wavelengths for the* $7S_{1/2} \rightarrow 6D_{3/2,5/2}$ *transitions in* $Ra^+$, *Chinese Physics B* **25** (aug, 2016) 093101.

[146] X. Liu, A. W. Bruch, Z. Gong, J. Lu, J. B. Surya, L. Zhang, J. Wang, J. Yan, and H. X. Tang, *Ultra-high-q uv microring resonators based on a single-crystalline aln platform*, *Optica* **5** (Oct., 2018) 1279–1282.

[147] P. Barakhshan, A. Marrs, A. Bhosale, B. Arora, R. Eigenmann, and M. S. Safronova. *Portal for High-Precision Atomic Data and Computation* (version 2.0). University of Delaware, Newark, DE, USA. URL: https://www.udel.edu/atom, Feb, 2022.

[148] P. Dubé, A. A. Madej, Z. Zhou, and J. E. Bernard, *Evaluation of systematic shifts of the $^{88}Sr^{+}$ single-ion optical frequency standard at the $10^{-17}$ level*, Phys. Rev. A **87** (Feb., 2013) 023806.

[149] P.-L. Liu, Y. Huang, W. Bian, H. Shao, H. Guan, Y.-B. Tang, C.-B. Li, J. Mitroy, and K.-L. Gao, *Measurement of magic wavelengths for the $^{40}Ca^{+}$ clock transition*, Phys. Rev. Lett. **114** (Jun, 2015) 223001.

[150] N. Yu, W. Nagourney, and H. Dehmelt, *Radiative lifetime measurement of the $Ba^{+}$ metastable $D_{3/2}$ state*, Phys. Rev. Lett. **78** (Jun, 1997) 4898–4901.

[151] M. Knoop, M. Vedel, and F. Vedel, *Lifetime, collisional-quenching, and j-mixing measurements of the metastable 3d levels of $ca^{+}$*, Phys. Rev. A **52** (Nov, 1995) 3763–3769.

[152] P. A. Barton, C. J. S. Donald, D. M. Lucas, D. A. Stevens, A. M. Steane, and D. N. Stacey, *Measurement of the lifetime of the $3d^2 D_{5/2}$ state in $^{40}ca^{+}$*, PRA **62** (Aug., 2000) 032503.

[153] A. Kreuter, C. Becher, G. P. T. Lancaster, A. B. Mundt, C. Russo, H. Häffner, C. Roos, W. Hänsel, F. Schmidt-Kaler, R. Blatt, and M. S. Safronova, *Experimental and theoretical study of the $3d^2d$-level lifetimes of $^{40}Ca^{+}$*, PRA **71** (Mar., 2005) 032504.

[154] C. Wunderlich, T. Hannemann, T. Körber, H. Häffner, C. Roos, W. Hänsel, R. Blatt, and F. Schmidt-Kaler, *Robust state preparation of a single trapped ion by adiabatic passage*, null **54** (July, 2007) 1541–1549.

[155] W. Nagourney, J. Sandberg, and H. Dehmelt, *Shelved optical electron amplifier: Observation of quantum jumps*, PRL **56** (June, 1986) 2797–2799.

[156] B. Merkel, K. Thirumalai, J. E. Tarlton, V. M. Schäfer, C. J. Ballance, T. P. Harty, and D. M. Lucas, *Magnetic field stabilization system for atomic physics experiments*, Review of Scientific Instruments **90** (2019), no. 4 044702, [https://doi.org/10.1063/1.5080093].

[157] P. Puri, M. Mills, I. Simbotin, J. A. Montgomery, R. Côté, C. Schneider, A. G. Suits, and E. R. Hudson, *Reaction blockading in a reaction between an excited atom and a charged molecule at low collision energy*, Nat. Chem. **11** (2019), no. 7 615–621.

[158] T. Sikorsky, Z. Meir, R. Ben-shlomi, N. Akerman, and R. Ozeri, *Spin-controlled atom-ion chemistry*, *Nature Communications* **9** (2018), no. 1 920.

[159] M. S. Safronova, V. A. Dzuba, V. V. Flambaum, U. I. Safronova, S. G. Porsev, and M. G. Kozlov, *Highly charged ions for atomic clocks, quantum information, and search for $\alpha$ variation*, *Phys. Rev. Lett.* **113** (July, 2014) 030801.

[160] M. G. Kozlov, M. S. Safronova, J. R. Crespo López-Urrutia, and P. O. Schmidt, *Highly charged ions: Optical clocks and applications in fundamental physics*, *RMP* **90** (Dec., 2018) 045005.

[161] P. Micke, T. Leopold, S. A. King, E. Benkler, L. J. Spieß, L. Schmöger, M. Schwarz, J. R. Crespo López-Urrutia, and P. O. Schmidt, *Coherent laser spectroscopy of highly charged ions using quantum logic*, *Nature* **578** (2020), no. 7793 60–65.

[162] L. P. Gaffney, P. A. Butler, M. Scheck, A. B. Hayes, F. Wenander, M. Albers, B. Bastin, C. Bauer, A. Blazhev, S. Bonig, N. Bree, J. Cederkall, T. Chupp, D. Cline, T. E. Cocolios, T. Davinson, H. De Witte, J. Diriken, T. Grahn, A. Herzan, M. Huyse, D. G. Jenkins, D. T. Joss, N. Kesteloot, J. Konki, M. Kowalczyk, T. Kroll, E. Kwan, R. Lutter, K. Moschner, P. Napiorkowski, J. Pakarinen, M. Pfeiffer, D. Radeck, P. Reiter, K. Reynders, S. V. Rigby, L. M. Robledo, M. Rudigier, S. Sambi, M. Seidlitz, B. Siebeck, T. Stora, P. Thoele, P. Van Duppen, M. J. Vermeulen, M. von Schmid, D. Voulot, N. Warr, K. Wimmer, K. Wrzosek-Lipska, C. Y. Wu, and M. Zielinska, *Studies of pear-shaped nuclei using accelerated radioactive beams*, *Nature* **497** (May, 2013) 199–204.

[163] A. D. Kudashov, A. N. Petrov, L. V. Skripnikov, N. S. Mosyagin, T. A. Isaev, R. Berger, and A. V. Titov, *Ab initio study of radium monofluoride (raf) as a candidate to search for parity- and time-and-parity–violation effects*, *Phys. Rev. A* **90** (Nov., 2014) 052513.

[164] Y. Zhou, Y. Shagam, W. B. Cairncross, K. B. Ng, T. S. Roussy, T. Grogan, K. Boyce, A. Vigil, M. Pettine, T. Zelevinsky, J. Ye, and E. A. Cornell, *Second-scale coherence measured at the quantum projection noise limit with hundreds of molecular ions*, *Phys. Rev. Lett.* **124** (Feb, 2020) 053201.

[165] X. Chen, Y.-W. Lin, and B. C. Odom, *Doppler amplification of motion of a trapped three-level ion*, *New J. Phys.* **17** (apr, 2015) 043037.

[166] K. Vahala, M. Herrmann, S. Knünz, V. Batteiger, G. Saathoff, T. W. Hänsch, and T. Udem, *A phonon laser*, *Nat. Phys.* **5** (Sept., 2009) 682–686.

[167] C. Schneider, S. J. Schowalter, K. Chen, S. T. Sullivan, and E. R. Hudson, *Laser-cooling-assisted mass spectrometry*, *Phys. Rev. Applied* **2** (Sept., 2014) 034013.

[168] N. Deb, L. L. Pollum, A. D. Smith, M. Keller, C. J. Rennick, B. R. Heazlewood, and T. P. Softley, *Coulomb crystal mass spectrometry in a digital ion trap*, *Phys. Rev. A* **91** (Mar, 2015) 033408.

[169] P. C. Schmid, J. Greenberg, M. I. Miller, K. Loeffler, and H. J. Lewandowski, *An ion trap time-of-flight mass spectrometer with high mass resolution for cold trapped ion experiments*, *Rev. Sci. Instrum.* **88** (Dec., 2017) 123107.

[170] P. F. Staanum, K. Højbjerre, R. Wester, and M. Drewsen, *Probing isotope effects in chemical reactions using single ions*, *Phys. Rev. Lett.* **100** (Jun, 2008) 243003.

[171] S. Willitsch, M. T. Bell, A. D. Gingell, S. R. Procter, and T. P. Softley, *Cold reactive collisions between laser-cooled ions and velocity-selected neutral molecules*, *Phys. Rev. Lett.* **100** (Jan, 2008) 043203.

[172] A. D. Gingell, M. T. Bell, J. M. Oldham, T. P. Softley, and J. N. Harvey, *Cold chemistry with electronically excited ca+ coulomb crystals*, *J. Chem. Phys.* **133** (2010), no. 19 194302, [https://doi.org/10.1063/1.3505142].

[173] J. E. Goeders, C. R. Clark, G. Vittorini, K. Wright, C. R. Viteri, and K. R. Brown, *Identifying single molecular ions by resolved sideband measurements*, *J. Phys. Chem. A* **117** (Oct., 2013) 9725–9731.

[174] K. Groot-Berning, F. Stopp, G. Jacob, D. Budker, R. Haas, D. Renisch, J. Runke, P. Thörle-Pospiech, C. E. Düllmann, and F. Schmidt-Kaler, *Trapping and sympathetic cooling of single thorium ions for spectroscopy*, *Phys. Rev. A* **99** (Feb., 2019) 023420.

[175] M. Drewsen, A. Mortensen, R. Martinussen, P. Staanum, and J. L. Sørensen, *Nondestructive identification of cold and extremely localized single molecular ions*, *Phys. Rev. Lett.* **93** (Dec, 2004) 243201.

[176] G. Janik, W. Nagourney, and H. Dehmelt, *Doppler-free optical spectroscopy on the ba+ mono-ion oscillator*, *J. Opt. Soc. Am. B* **2** (Aug, 1985) 1251–1257.

[177] See Supplemental Material, which includes Refs. [225, 226, 11, 21, 227, 228], for further discussion of ion motional amplification, secular frequency calculations, and OMS systematic effects.

[178] H. Oberst, *Resonance fluorescence of single barium ions*, Master's thesis, University of Innsbruck, 1999.

[179] J. Roßnagel, K. N. Tolazzi, F. Schmidt-Kaler, and K. Singer, *Fast thermometry for trapped ions using dark resonances*, *New J. Phys.* **17** (Apr., 2015) 045004.

[180] W. Lu and S. Yang, *Reactions of alkaline earth metal ions with methanol clusters*, *J. Phys. Chem. A* **102** (Jan., 1998) 825–840.

[181] J. I. Lee and J. M. Farrar, *Hot and cold clusters: photodissociation of sr+(ch3od)n through vibrationally excited intermediates*, *J. Phys. Chem. A* **106** (Dec., 2002) 11882–11890.

[182] P. Puri, M. Mills, C. Schneider, I. Simbotin, J. A. Montgomery, R. Côté, A. G. Suits, and E. R. Hudson, *Synthesis of mixed hypermetallic oxide baoca&lt;sup&gt;+&lt;/sup&gt; from laser-cooled reagents in an atom-ion hybrid trap*, *Science* (Sept., 2017).

[183] B. L. Augenbraun, Z. D. Lasner, A. Frenett, H. Sawaoka, C. Miller, T. C. Steimle, and J. M. Doyle, *Laser-cooled polyatomic molecules for improved electron electric dipole moment searches*, *New J. Phys.* **22** (feb, 2020) 022003.

[184] Coursey, J.S., Schwab, D.J., Tsai, J.J., and Dragoset, R.A. (2015), Atomic Weights and Isotopic Compositions (version 4.1). [Online] Available: http://physics.nist.gov/Comp [2020 Sep 24]. National Institute of Standards and Technology, Gaithersburg, MD.

[185] N. B. Khanyile, G. Shu, and K. R. Brown, *Observation of vibrational overtones by single-molecule resonant photodissociation*, *Nat. Commun.* **6** (July, 2015) 7825.

[186] F. Wolf, Y. Wan, J. C. Heip, F. Gebert, C. Shi, and P. O. Schmidt, *Non-destructive state detection for quantum logic spectroscopy of molecular ions*, *Nature* **530** (Feb., 2016) 457.

[187] L. Ratschbacher, C. Zipkes, C. Sias, and M. Köhl, *Controlling chemical reactions of a single particle*, *Nat. Phys.* **8** (2012), no. 9 649–652.

[188] K. G. Johnson, J. D. Wong-Campos, A. Restelli, K. A. Landsman, B. Neyenhuis, J. Mizrahi, and C. Monroe, *Active stabilization of ion trap radiofrequency potentials*, *Rev. Sci. Instrum.* (2016).

[189] L. Skripnikov. Private communication.

[190] B. C. Sawyer, J. G. Bohnet, J. W. Britton, and J. J. Bollinger, *Reversing hydride-ion formation in quantum-information experiments with* $be^+$, *Phys. Rev. A* **91** (Jan., 2015) 011401.

[191] K. Mølhave and M. Drewsen, *Formation of translationally cold* $mgh^+$ *and* $mgd^+$ *molecules in an ion trap*, *Phys. Rev. A* **62** (Jun, 2000) 011401.

[192] J. Condoluci, S. Janardan, A. T. Calvin, R. Rugango, G. Shu, C. D. Sherrill, and K. R. Brown, *Reassigning the cah+ 11 → 21 vibronic transition with cad+*, *The Journal of Chemical Physics* **147** (2017), no. 21 214309, [https://doi.org/10.1063/1.5016556].

[193] H. Wu, M. Mills, E. West, M. C. Heaven, and E. R. Hudson, *Increase of the barium ion-trap lifetime via photodissociation*, *PRA* **104** (Dec., 2021) 063103.

[194] J. A. Coxon and R. Colin, *Born–oppenheimer breakdown effects from rotational analysis of thea1+–x1+band system of beh+, bed+, and bet+*, *Journal of Molecular Spectroscopy* **181** (1997), no. 1 215–223.

[195] A. Shayesteh, R. D. E. Henderson, R. J. Le Roy, and P. F. Bernath, *Ground state potential energy curve and dissociation energy of mgh*, *The Journal of Physical Chemistry A* **111** (2007), no. 49 12495–12505, [https://doi.org/10.1021/jp075704a]. PMID: 18020428.

[196] Z. Yang, H. Chen, Y. Mao, and M. Chen, *A neural network potential energy surface and quantum dynamics studies for the ca+(2s) + h2 → cah+ + h reaction*, *Phys. Chem. Chem. Phys.* **24** (2022) 19209–19217.

[197] A. K. Hansen, M. A. Sørensen, P. F. Staanum, and M. Drewsen, *Single-ion recycling reactions*, *Angewandte Chemie International Edition* **51** (2012), no. 32 7960–7962.

[198] A. T. Calvin, S. Janardan, J. Condoluci, R. Rugango, E. Pretzsch, G. Shu, and K. R. Brown, *Rovibronic spectroscopy of sympathetically cooled 40cah+*, *The Journal of Physical Chemistry A* **122** (2018), no. 12 3177–3181, [https://doi.org/10.1021/acs.jpca.7b12823]. PMID: 29521505.

[199] C. S. Wood, S. C. Bennett, D. Cho, B. P. Masterson, J. L. Roberts, C. E. Tanner, and C. E. Wieman, *Measurement of parity nonconservation and an anapole moment in cesium*, *Science* **275** (Mar., 1997) 1759.

[200] P. Yu. Private communication. The data is generated with python code ported from the original Mathematica code by P. Yu.

[201] J. L. Bohn. Private communication. The data is generated with python code ported from the original matlab code by J. L. Bohn.

[202] C. H. Townes and A. L. Schawlow, *Microwave spectroscopy / C.H. Townes and A.L. Schawlow.* International series in pure and applied physics. McGraw-Hill, New York, 1955.

[203] E. R. Meyer, A. E. Leanhardt, E. A. Cornell, and J. L. Bohn, *Berry-like phases in structured atoms and molecules*, *PRA* **80** (Dec., 2009) 062110.

[204] A. E. Leanhardt, J. L. Bohn, H. Loh, P. Maletinsky, E. R. Meyer, L. C. Sinclair, R. P. Stutz, and E. A. Cornell, *High-resolution spectroscopy on trapped molecular ions in rotating electric fields: A new approach for measuring the electron electric dipole moment*, Journal of Molecular Spectroscopy **270** (Nov., 2011) 1–25.

[205] H. Loh, K. C. Cossel, M. C. Grau, K.-K. Ni, E. R. Meyer, J. L. Bohn, J. Ye, and E. A. Cornell, *Precision spectroscopy of polarized molecules in an ion trap*, Science **342** (Dec., 2013) 1220.

[206] U. Schramm, T. Schätz, and D. Habs, *Bunched crystalline ion beams*, Phys. Rev. Lett. **87** (Oct, 2001) 184801.

[207] B. Tabakov, F. Benito, M. Blain, C. R. Clark, S. Clark, R. A. Haltli, P. Maunz, J. D. Sterk, C. Tigges, and D. Stick, *Assembling a ring-shaped crystal in a microfabricated surface ion trap*, Phys. Rev. Appl. **4** (Sep, 2015) 031001.

[208] H.-K. Li, E. Urban, C. Noel, A. Chuang, Y. Xia, A. Ransford, B. Hemmerling, Y. Wang, T. Li, H. Häffner, and X. Zhang, *Realization of translational symmetry in trapped cold ion rings*, Phys. Rev. Lett. **118** (Jan, 2017) 053001.

[209] T. N. Taylor, J. O. Island, and Y. Zhou, *Quantum logic control and precision measurements of molecular ions in a ring trap – a new approach for testing fundamental symmetries*, 2022.

[210] C. Hallas, N. B. Vilas, L. Anderegg, P. Robichaud, A. Winnicki, C. Zhang, L. Cheng, and J. M. Doyle, *Optical trapping of a polyatomic molecule in an $\ell$-type parity doublet state*, 2022.

[211] C. Schneider, M. Enderlein, T. Huber, and T. Schaetz, *Optical trapping of an ion*, Nature Photonics **4** (2010), no. 11 772–775.

[212] T. Huber, A. Lambrecht, J. Schmidt, L. Karpa, and T. Schaetz, *A far-off-resonance optical trap for a ba+ ion*, Nature Communications **5** (2014), no. 1 5587.

[213] G. Arrowsmith-Kron, K. Bailey, M. Bishof, M. Gott, J. Greene, P. Mueller, T. O'Connor, J. Singh, and M. Dietrich, *Progress on a More Sensitive Measurement of the Atomic Electric Dipole Moment of Radium-225 and Radium-223*, in *APS Division of Atomic, Molecular and Optical Physics Meeting Abstracts*, vol. 2022 of *APS Meeting Abstracts*, p. C03.004, Jan., 2022.

[214] Z. Varga, A. Nicholl, and K. Mayer, *Determination of the $^{229}$Th half-life*, Phys. Rev. C **89** (Jun, 2014) 064310.

[215] T. Dinneen, A. Ghiorso, and H. Gould, *An orthotropic source of thermal atoms*, Review of Scientific Instruments **67** (Mar., 1996) 752–755.

[216] B. Santra, *Precision spectroscopy of neutral radium: towards searches for permanent electric dipole Electric.* PhD thesis, University of Groningen,, 2013.

[217] B. Santra, U. Dammalapati, A. Groot, K. Jungmann, and L. Willmann, *Absolute frequency measurement of the $7s^2\ ^1S_0 \rightarrow 7s7p\ ^1P_1$ transition in $^{225}$Ra*, Phys. Rev. A **90** (Oct., 2014) 040501.

[218] L. von der Wense, B. Seiferle, M. Laatiaoui, J. B. Neumayr, H.-J. Maier, H.-F. Wirth, C. Mokry, J. Runke, K. Eberhardt, C. E. Düllmann, N. G. Trautmann, and P. G. Thirolf, *Direct detection of the 229th nuclear clock transition*, Nature **533** (2016), no. 7601 47–51.

[219] W. L. Trimble, I. A. Sulai, I. Ahmad, K. Bailey, B. Graner, J. P. Greene, R. J. Holt, W. Korsch, Z.-T. Lu, P. Mueller, and T. P. O'Connor, *Lifetime of the $7s6d$ $^1D_2$ atomic state of radium*, Phys. Rev. A **80** (Nov, 2009) 054501.

[220] D. R. Olander and V. Kruger, *Molecular beam sources fabricated from multichannel arrays. iii. the exit density problem*, Journal of Applied Physics **41** (June, 1970) 2769–2776.

[221] D. J. Santeler, *New concepts in molecular gas flow*, Journal of Vacuum Science & Technology A **4** (1986), no. 3 338–343, [https://doi.org/10.1116/1.573923].

[222] S. Gulde, D. Rotter, P. Barton, F. Schmidt-Kaler, R. Blatt, and W. Hogervorst, *Simple and efficient photo-ionization loading of ions for precision ion-trapping experiments*, Applied Physics B **73** (2001), no. 8 861–863.

[223] J.-S. Chen, *Ticking near the zero-point energy: towards $1x10^{-18}$ accuracy in $Al^+$ optical clocks.* PhD thesis, University of Colorado, 2017.

[224] M. F. Brandl, P. Schindler, T. Monz, and R. Blatt, *Cryogenic resonator design for trapped ion experiments in paul traps*, Applied Physics B **122** (May, 2016) 157.

[225] P. D. Lett, W. D. Phillips, S. L. Rolston, C. E. Tanner, R. N. Watts, and C. I. Westbrook, *Optical molasses*, J. Opt. Soc. Am. B **6** (Nov., 1989) 2084–2107.

[226] U. Kemiktarak, M. Durand, M. Metcalfe, and J. Lawall, *Mode competition and anomalous cooling in a multimode phonon laser*, Phys. Rev. Lett. **113** (Jul, 2014) 030802.

[227] D. Kielpinski, B. E. King, C. J. Myatt, C. A. Sackett, Q. A. Turchette, W. M. Itano, C. Monroe, D. J. Wineland, and W. H. Zurek, *Sympathetic cooling of trapped ions for quantum logic*, Phys. Rev. A **61** (Feb, 2000) 032310.

[228] N. Akerman, S. Kotler, Y. Glickman, Y. Dallal, A. Keselman, and R. Ozeri, *Single-ion nonlinear mechanical oscillator*, Phys. Rev. A **82** (Dec, 2010) 061402(R).